Mécanismes d'interaction entre décharges nanosecondes répétitives pulsées et écoulements laminaires réactifs

Sylvain Heitz

université PARIS-SACLAY

NNT : 2017ACLC069

Thèse de doctorat

CentraleSupélec

Interaction mechanisms between nanosecond repetitively pulsed discharges and laminar reactive flows

préparée à CentraleSupélec et Technische Universität Berlin

École doctorale n°579 Sciences mécaniques et énergétiques, matériaux et géosciences (SMEMAG)
Spécialité de doctorat : Énergétique

Thèse présentée et soutenue à Gif-Sur-Yvette, le 27/11/2017, par

Sylvain Heitz

Composition du Jury :

Julien Sotton Professeur, ENSMA – ISAE	Président
Anne Bourdon Directrice de recherche, École Polytechnique – LPP CNRS	Rapporteur
Christian Oliver Paschereit Professeur, TU Berlin – ISTA	Rapporteur
Thierry Schuller Professeur, Université III – IMFT	Directeur de thèse
Deanna Lacoste Professeur Assistant, KAUST– CCRC	Co-Directrice de thèse
Jonas Moeck Professeur Assistant, TU Berlin – ISTA	Co-Directeur de thèse

Acknowledgments

This doctoral work has brought me a long way, starting from Paris, on to Berlin, to finish as far as Saudi Arabia. I have met a number of people I would like to thank, but some of them are not quite at ease with foreign languages, preventing me to properly give credit where credit is due (which is the point of this section, really). I finally gave up on overthinking about what language to use and settled on my slightly-less-than-Shakespearean English. Any translation request, you know where to find me.

First of all, a thousand thanks to my advisors, Deanna, Jonas and Thierry. It may be a *cliché* to say that nothing would have been possible without your help and counsel, but it is just plain truth. As important as your stolid guidance and constant enthusiasm and interest towards my work, I thank you for having been able to put up with me for more than three years (Lord knows I was surprised you showed no impatience after a mere three months).

There are a lot of people I would like to mention here. First in EM2C, where it all started, many thanks to my colleagues and friends Kevin (who may now soon start a post-doc, or build missiles, I'm still not sure) and Erwan (who always works at these ungodly hours of his), with whom I discovered the ups and downs of research work. I would also like to thank Marien and Laurent for being such great office pals and Nathalie, Noï and Brigitte for their help. My gratitude also goes to all my colleagues from the ISTA, in particular Richard, Lisa, Tom, Eric and Olaf from the HFI-102, but also Sandy and Maria, Professor Paschereit, for welcoming me in Berlin and giving me this unique opportunity to work in their institute. Then, there are the people I got acquainted with in Saudi Arabia, especially those in the CCRC. Francesco, Valentina, Sumit, Monika, Eshan, Josh, Tony and Louise, you have all contributed to make my stay there a real pleasure.

Work matters, yet fun and games also does, so my gratitude also goes to my friends. Apart from the ones I cited above, there is also Anne, Björn and the gang from Berlin; then Clara, Marie, Sylvain (never forget the Trésor)

and Johanna. My travel companions also deserve a mention in here: Loïc, Leah, Bryan, Monica and so many more. A special appreciation for my crew, namely, Lucas, Kevin, François, Vivien and Hélène which have been particularly supportive (though they tried their best not to be); they are the ones who made these three years tremendous fun for me and I cannot expect anything else than for them to keep on doing so.

Last but not least, I thank my family. My parents of course, for their constant support and cheerfulness despite having a son seemingly unable to stay put in one place for more than two weeks, but also my bros Stéphane, Dorian and Kevin (yes, him again, but if almost twenty years of friendship does not reward one with twice the credit, then nothing does), for keeping my spirits up with their wry, sometimes edging on sarcastic, sense of humour. Life is a bumpy road, but a loving family and great friends help one to overcome any challenge one can face.

Abstract

The interactions between Nanosecond Repetitively Pulsed (NRP) plasma discharges and laminar reactive flows are investigated. The NRP discharges used in this study have durations of 10 ns, voltage amplitudes up to 15 kV and are pulsed at a repetition frequency up to 30 kHz, thus yielding pulse energies of less than one millijoule.

In a first chapter, the influence of steady and unsteady air flows on the regimes of NRP discharges is investigated. The results are interpreted with the use of characteristic dimensionless numbers; this analysis allows to highlight a synergetic effect between the high-voltage pulses as well as the power of the pulses on the NRP discharge regime observed.

The second chapter presents an investigation of the effect of laminar premixed methane-air flames on NRP discharges. An effect of the flame on the NRP corona discharges is displayed; this effect is a function of the proximity of the flame to the discharges. Additionally, the influence of the inter-electrode gas mixture on the shape of the plasma discharges is also visually assessed.

Finally, the last chapter focuses on the effect of NRP corona discharges on laminar premixed flat flames. The NRP discharges induce a displacement of the flame in the upstream direction. Enhancement of the laminar flame speed caused by NRP discharges application is assumed to be the reason for this flame motion and the validity of this hypothesis is verified by one-dimensional numerical simulations of axisymmetric flames.

This study displays the effect of NRP discharges on a flame and gives insights as to the phenomenon underlying this effect, namely the flame speed enhancement by generation of ozone and heat by the plasma discharges. Moreover, the study highlights the opposite effect of reactive mixtures on the NRP discharges. The visual modification of the NRP discharges is a function of the transport of the inter-electrode flow and of the nature of the gas itself. This influence of the mixture is attributed to several effects such as modification of the spectroscopic

properties of the mixture, and electromagnetic and thermal effect when a flame is stabilised close to the electrodes.

Résumé

Les interactions entre décharges Nanosecondes Répétitives Pulsées (NRP) et des écoulements de gaz laminaires sont étudiées. Dans cette étude, les décharges NRP ont des durées de 10 ns, des amplitudes en tension de 15 kV et sont pulsées à des fréquences maximales de répétition de 30 kHz, résultant en des énergies inférieures à un millijoule.

Dans un premier chapitre, l'influence d'écoulements d'air stationnaires et instationnaires sur les régimes de décharges NRP est étudiée. Les résultats sont interprétés au moyen de nombres adimensionnels; cette analyse met en évidence l'effet synergétique du nombre d'impulsions appliquées, ainsi que de la puissance des pulses, sur le régime de décharge NRP observé.

Le second chapitre présente une étude de l'effet de flammes méthane-air laminaires prémélangées sur des décharges NRP. Dans les deux configurations expérimentales utilisées, un effet de la flamme sur les décharges NRP en régime couronne est démontré; cet effet dépend de la distance entre la flamme et les décharges. De plus, l'influence du mélange de gaz entre les électrodes sur la forme des décharges plasma est démontrée.

Enfin, le dernier chapitre se concentre sur l'effet de décharges NRP en régime couronne sur des flammes plates laminaires prémélangées. Dans les deux mêmes configurations qu'au chapitre précédent, les décharges NRP entraînent un déplacement de la flamme vers l'amont. Ce mouvement de flamme est supposé dû à l'augmentation de la vitesse de flamme laminaire causée par l'application de décharges NRP. Des simulations numériques 1D de flammes axisymétriques sont réalisées afin de vérifier la validité de cette hypothèse.

Cette étude met en évidence l'effet des décharges NRP sur une flamme et donne des indications sur le phénomène à l'origine de cet effet, à savoir l'augmentation de la vitesse de flamme laminaire par le biais de la génération de chaleur et d'ozone par les décharges plasma. De plus, l'étude démontre l'effet opposé de mélanges réactifs sur les décharges NRP. Les décharges NRP sont modifiées

par le phénomène de convection du gaz entre les électrodes ainsi que par la constitution de ce gaz. La modification des décharges NRP par la composition du mélange réactif est le résultat de différents effets : un effet chimique lié à la composition du mélange gazeux, ainsi que deux effets additionnels, thermique et électromagnétique, lorsqu'une flamme se trouve proche des électrodes.

Zusammenfassung

Untersucht werden die Interaktionsprozesse zwischen gepulsten Nanosekunden- (NRP-) Plasmaentladungen mit laminaren, reaktiven Strömungen. Die erzeugten Hochspannungsentladungen haben eine Dauer von 10 ns, eine Spannungsamplitude von 10 kV und werden mit einer Pulswiederholrate von bis zu 30 kHz erzeugt. Die Energie pro Puls entspricht hierbei weniger als ein Millijoule.

Im ersten Kapitel wird der Einfluss von konstanter und schwankender Luftströmung auf die Entladungsform der NRP-Plasmaentladungen untersucht. Angegeben werden die Ergebnisse mittels dimensionslosen Kennzahlen, wodurch unter anderem die Abhängigkeit zwischen der Anzahl an Pulsen, welche auf ein einzelnes Luftteilchen einwirken, und der Pulsenergie auf die Entladungsform charakterisiert werden konnte.

Das zweite Kapitel behandelt den Effekt von laminaren Methan/Luft Vormischflammen auf die NRP-Entladungen. Ein Effekt der Flamme auf die Corona-Plasmaentladungen is beobachtet. Zudem konnte gezeigt werden, dass der beobachtete Effekt sich mit kleiner werdendem Abstand zwischen Elektroden und Flamme verstärkt. Des Weiteren wurde auch der Einfluss der Gasmischung untersucht.

Im letzten Kapitels ist der Effekt von Coronaentladungen auf den Verbrennungsprozess von laminaren Vormischflammen untersucht. Es konnte gezeigt werden, dass die Plasmaentladungen eine Bewegung der Flamme stromauf verursachen. Mittels 1D-Simulationen konnte gezeigt werden, dass diese Bewegung durch eine Erhöhung der laminaren Flammengeschwindigkeit erklärt werden kann.

Contents

List of Tables

List of Figures

Nomenclature

Values:

T	temperature	K
p	pressure	Pa
k_{B}	Boltzmann's constant	$\mathrm{m}^2.\mathrm{kg}.\mathrm{s}^{-2}.\mathrm{K}^{-1}$
E/n	reduced electric field	Td
U	inter-electrode voltage amplitude	kV
I	inter-electrode current	A
I_{disp}	displacement current	A
I_{cond}	conduction current	A
E_{p}	deposited energy per pulse	$\mu\mathrm{J}.\mathrm{pulse}^{-1}$
P_{p}	mean power of the NRP discharges	W
n	number of applied pulses on air particles	.
d	gap distance between electrodes	mm
D_{h}	hydraulic diameter of inter-electrode area	mm
u_z, u_θ, u_r	instantaneous axial, azimuthal, radial velocity	$\mathrm{m}.\mathrm{s}^{-1}$
$\bar{u}_z$, $\bar{u}_\theta$, $\bar{u}_r$	mean axial, azimuthal, radial velocity	$\mathrm{m}.\mathrm{s}^{-1}$
t_{R}	air residence time in inter-electrode area	ms
f_{ac}	acoustic frequency	Hz
C_{air}	speed of sound	$\mathrm{m}.\mathrm{s}^{-1}$
$\bar{u}_z$	mean axial velocity	$\mathrm{m}.\mathrm{s}^{-1}$
u'_z	RMS axial velocity	$\mathrm{m}.\mathrm{s}^{-1}$

$u'_z/\bar{u}_z$	relative RMS axial velocity	.
Φ	equivalence ratio of the flame	.
P_{th}	heat release rate of the flame	W
S_{L}	laminar flame speed	cm.s^{-1}
z_0	axial position of the flame's centre	mm
z_{R}	axial position of the flame's sides	mm
A_{fl}	surface of the flame's leading edge	mm^2
T_{e^-}	electron temperature	eV
k	reaction rate constant	order dependent
ω	reaction rate	$\text{mol.cm}^{-3}\text{.s}^{-1}$
[X]	concentration of species X	mol.cm^{-3}

Abbreviations:

NRP	Nanosecond Repetitively Pulsed
PRF	Pulse Repetition Frequency
RMS	Root Mean Square
C-S	NRP corona to spark transition
S-C	NRP spark to corona transition
e^-	electron

Introduction

Recent years have seen an increase in research on Nanosecond Repetitively Pulsed (NRP) plasma discharges for applications such as medical treatment (see review by Heinlin et al. 2010), biological decontamination (see reviews by Moreau et al. 2008; Lu et al. 2016), fuel reforming (see reviews by Lebouvier et al. 2013; Snoeckx and Bogaerts 2016), aerodynamic flow control (see review by Adamovich et al. 2009) and combustion (see reviews by Starikovskiy and Aleksandrov 2013; Starikovskaia 2014; Ju and Sun 2015a). All of these requiring highly reactive plasma at ambient conditions with a low electrical energy input. This thesis focuses on the field of plasma-assisted combustion. The effect of NRP plasma discharges on a reactive mixture is threefold: first, the discharges induce a heating of the inter-electrode gas, thus locally decreasing its density; second, they produce ions, radicals, and excited species (such as excited nitrogen, atomic oxygen, ozone and nitric oxides); third, the electromagnetic field generated by the high-voltage pulses influences the electrons and charged species that are naturally present in the flame. A reactive mixture also exercises a similar, reciprocal effect on NRP discharges. Three different regimes of NRP discharges are usually distinguished (see Pai et al. 2009; Pai et al. 2010a; Pai et al. 2010b): corona, glow and spark. Although all three of them are encountered in the coming study, the focus is mostly on the NRP corona discharges.

The purpose of this work is to study the interactions taking place between NRP discharges and laminar reactive mixtures. Indeed, for combustion enhancement applications, usually NRP spark discharges are used because they have a spectacular effect on combustion due to a strong gas heating (up to 4,000 K, see Pai et al. 2010a). However, less energetic regimes, such as NRP glow and corona discharges are of practical interest to understand how the plasma-induced chemistry can affect the combustion process. Only a few studies have been conducted on NRP glow and corona discharges for applications in combustion (see Lacoste et al. 2017a; Lacoste et al. 2017b; Lacoste et al. 2017c and the review by Ju and Sun 2015a; Ju and Sun 2015b). Currently, there is a lack of quantitative information on these effects.

In addition, while plasma discharges have already proven their efficiency in altering a flame, little is known about the opposite effect of the flame on the NRP discharges. This reverse effect is also investigated in this work. Chapter 1 of this thesis presents a bibliographic review on plasma-assisted combustion by NRP discharges.

In Chapter 2, the effect of laminar air flows on the regimes of NRP discharges is investigated. First, the effect of steady air flows on the NRP discharges is assessed. It is shown that the modification of inter-electrode voltage amplitude, Pulse Repetition Frequency (PRF) and axial air velocity allow to cause NRP corona-to-spark or spark-to-corona regime transitions, while the azimuthal air velocity between the electrodes does not influence the regime of NRP discharges. Then, an acoustic oscillation is applied to the air flow and it is shown that, under certain conditions of relative velocity amplitude and of frequency of the forcing, similar corona-to-spark and spark-to-corona transitions could be observed. The results from these two experiments are interpreted in terms of dimensionless numbers and display the significance of two parameters in the observed NRP regime: the number of high-voltage pulses applied to a particle of air during its transit in the inter-electrode area and the power of each of these high-voltage discharges. A model is established and allows to reproduce qualitatively the trends obtained in the experiments.

Chapter 3 of the present study focuses on displaying the influence of laminar premixed flames on NRP corona discharges. Two experimental setups implementing complementary configurations are used. In the first one, the NRP corona discharges are generated in a parallel direction to a laminar premixed lean methane-air flame, stabilised in a conical quartz tube with an acoustic forcing. In this configuration, the shape of the NRP discharges is significantly modified when the distance between the flame and the electrodes is less than 7 mm. This effect is also visible in the second configuration, where the NRP corona discharges are pulsed across the reaction front of an aerodynamically stabilised laminar premixed methane-air flame. The length of the discharges increases when the flame is stabilised between the electrodes, compared to the case without flame. This effect of the flame's presence is attributed to a local increase in the reduced electric field in the hot combustion products, as well as an interaction between the electromagnetic field of the plasma discharges and the charged species constituting the flame. Additionally, the effect of the mixture itself is assessed by comparison of the NRP discharges in air and in an air-methane mixture. An explanation for the significant increase in length of the discharges following methane addition in air is proposed. This explanation is linked to a modification in the spectroscopic properties of the inter-electrode gas by modification of the gas composition.

Finally, Chapter 4 investigates the effect of NRP corona discharges on laminar premixed methane-air flames in the same two experimental configurations from the previous chapter. In the first configuration, application of NRP corona discharges in a direction parallel to the laminar premixed methane-air flame induces the flame to move upstream, closer to the electrodes. The upstream displacement of the flame increases with the voltage amplitude of the NRP discharges. The laminar flame speed is determined and compared without and with application of NRP discharges and an enhancement of up to 2.2 % in this configuration is displayed. In the second configuration, where NRP discharges are applied in a perpendicular direction to the flame front, the transient response of the flame to application of NRP discharges is first investigated with another setup, and a model for deduction of flame speed increase based on this transient response is presented; the enhancement of laminar flame speed reaches up to 9 %. On the second setup with perpendicular electrode configuration, the flame also moves upstream under plasma discharge application, all the more when the PRF of the discharges is increased. Additionally, a deformation of the flame's surface is observed.

In this same chapter, the thermal and chemical effects of NRP plasma discharges are also estimated by the establishment of a numerical model. The thermal production of the discharges results in an increase of fresh gas temperature while the chemical effect focuses on ozone generation by the discharges. Once determined, the influence of these thermal and chemical effects on the laminar flame speed and the adiabatic temperature of a one-dimensional axisymmetric premixed methane-air flame is estimated and yields a maximum enhancement of 35 % in the laminar flame speed and of 4 % in the adiabatic flame temperature.

To conclude, this study highlights the effect of NRP discharges on laminar reactive mixtures. This effect is due to an increase in the laminar speed of the flame caused by a reactivity increase of the gas treated by the plasma discharges, as well as from the small thermal addition and the electromagnetic field generated by the nanosecond high-voltage pulses. It was also demonstrated that, while NRP discharges have an effect on a flame, the flame itself—and, more widely, the reactive mixture—has a reciprocal effect on the NRP discharges, thus bringing several insights as to the phenomena underlying applications in the field of plasma-assisted combustion.

Chapter 1

Background

1.1 Introduction: plasma discharges

Plasma is often presented as the fourth state of matter and can be described as an electrically neutral ionised gas. Irving Langmuir, who first introduced the term in the 1930s, indeed described plasma as the region in an ionised gas containing balanced charges of ions and electrons.

A common technique for the generation of plasmas in laboratory is the use of electric discharges. Raizer (1987) presents them as discharges of a capacitor into a capacitive circuit consisting of a gap between two electrodes, both of these electrodes being connected to a power supply. The process of plasma generation by gas discharges is described in detail in the book of Fridman (2008). The electric field generated by the discharges accelerates the electrons in the gas. On their path, these accelerated electrons collide with the heavy particles from the gas and transfer energy to them in the process (this mechanism is commonly known as Joule heating), thus losing a fraction of their own energy. After a given number of collisions and provided the discharge energy is sufficient, the potential applied sufficiently long, and that no mechanism prevents the heating of the gas, the energies of electrons and heavy particles reach an equilibrium. If this equilibrium is established, electrons and heavy particles in the gas end up at a similar temperature. In this case, Local Thermodynamic Equilibrium (LTE) is reached and the ionisation and chemical processes in the plasma are determined by the gas temperature. The plasma in a LTE or quasi-LTE state is called thermal plasma.

Many plasmas exist at conditions where electrons and heavy particles are far

from LTE (if the discharge time scale is short enough, its energy low enough, or if a quenching mechanism of the gas exists). It is often the electron temperature that is significantly higher than the heavy particle temperature. In this case, the electron temperature is the one parameter determining the chemical and ionisation processes in the non-equilibrium plasma; such a plasma is also called non-thermal plasma.

Although having many features in common, thermal and non-thermal plasmas present different characteristics as well; for instance, thermal plasmas yield more power while non-thermal plasmas allow for a better selectivity of excited and ionised particles. Thus their application areas are also quite different.

Typical values for electron temperatures and electron densities are given in Figure 1.1 for different types of plasmas. The plasmas classified as equilibrium, such as the flame or arc, usually feature a low electron temperature (maximum $1\,\mathrm{eV} = 11{,}600\,\mathrm{K}$) while the electron temperature of the non-thermal plasmas is often much higher (up to 10 eV). The number density of electrons for all these plasmas can take values across a wide range (from 10^{10} to $10^{20}\,\mathrm{cm}^{-3}$) according to the type of discharge used.

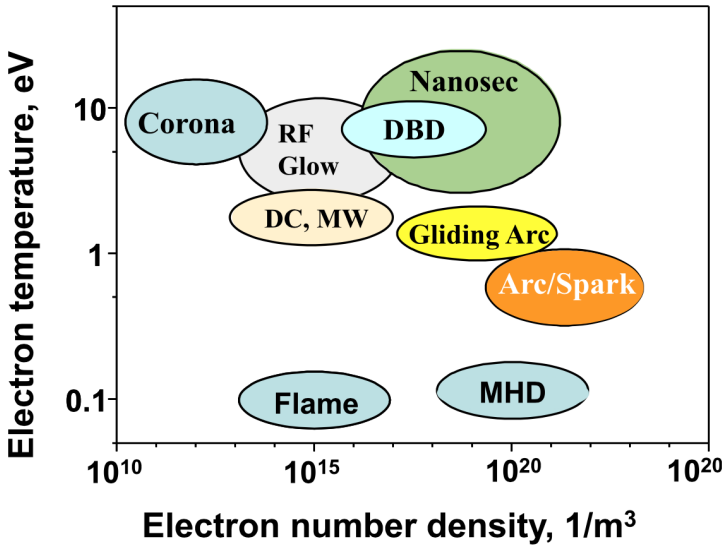

Figure 1.1: *Typical values for electron temperatures and electron densities of several types of plasmas: flame, magneto hydrodynamic discharge (MHD), arc, spark, glow, corona, radio-frequency (RF), direct current (DC), dielectric barrier discharge (DBD), nanosecond and gliding arc. Image from Ju and Sun (2015a).*

Non-equilibrium plasmas have a large range of potential applications. In the biomedical field, non-thermal plasmas are used for dermatology applications (see the review by Heinlin et al. 2010), for surface decontamination (as pre-

sented in the works of Moreau et al. 2008; Rupf et al. 2010; Cahill et al. 2014), for cancer treatment (see Hirst et al. 2014) and blood coagulation (see Kong et al. 2009). In the field of fuel reforming, Dielectric Barrier Discharges (DBD) are implemented in order to degrade benzene into CO molecules for syngas production by Jiang et al. (2013) and also to reform methane-carbon dioxide mixtures into syngas (see Scapinello et al. 2015). Similar DBD discharges, as well as nanosecond repetitively pulsed discharges show a potential for the partial oxidation of methane, as demonstrated by Nozaki et al. (2004); Zhang and Cha (2015). Finally, non-equilibrium discharges can be applied to surface treatment (see Stauss et al. 2010; Massines et al. 2012) for thin film deposition and are put to use by Stuckert and Fisher (2015) for the modification of surface properties of nanomaterials. The present study focuses on the non-equilibrium Nanosecond Repetitively Pulsed (NRP) plasma discharges and their application for the enhancement of combustion.

1.2 NRP plasma discharges

1.2.1 Principle and characterisation

Nanosecond Repetitively Pulsed discharges consist in ultra-short (from ten to a few hundreds of nanoseconds) high-voltage pulses (voltage amplitude in the order of the tens of kilovolts). The repetition rate of the pulses, also called Pulse Repetition Frequency (PRF), ranges between ten and few hundreds kilohertz.

Since the excitation of electrons occurs for a very short time, the condition for local thermodynamic equilibrium of the fluid in the inter-electrode area is not fulfilled; indeed, the electrons feature a temperature in the range from one to ten electronvolt, while the neutral particles, ions and radicals remain, depending on the plasma regime, from near-ambient temperature to a few thousands of Kelvins. Also due to the extremely short duration of the pulses, almost no ionic wind is induced and, for most applications, only a small portion of the deposited electrical energy of the discharges is converted into heating of the gas.

The existence of three different regimes of plasmas generated by NRP discharges has been established in the works of Pai et al. (2009); Pai et al. (2010a); Pai et al. (2010b). These NRP regimes are displayed in Figure 1.2 (from the thesis of Pai 2008) and are named corona, glow and spark. Their existence depends on a number of parameters such as the PRF of the high-voltage pulses, the radius of curvature of the electrodes and the reduced electric field, E/n, which

is defined as:

$$E/n = \frac{U\, k_{\mathrm{B}}\, T}{p\, d}, \tag{1.1}$$

where U is the applied voltage amplitude, d the inter-electrode gap distance, p the pressure, T the gas temperature and k_{B} the Boltzmann constant.

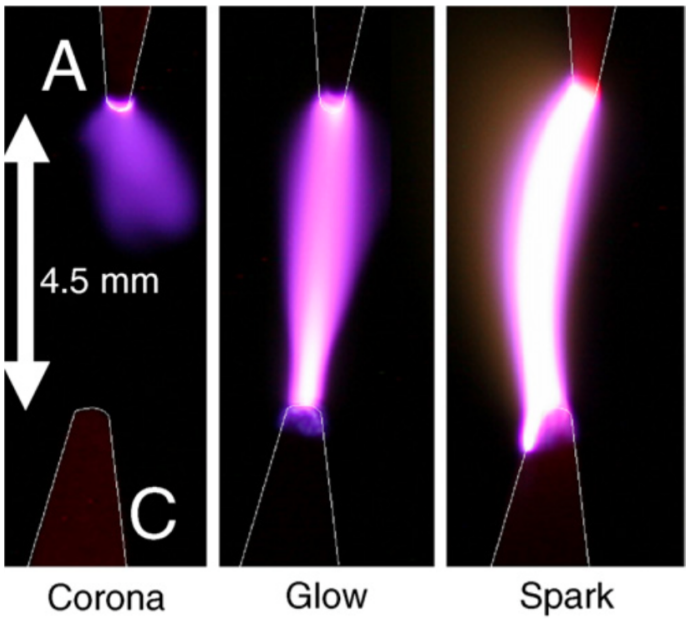

Figure 1.2: *Photographs from Pai (2008) of plasmas generated from NRP discharges: corona, glow and spark (from left to right) in air at $p = 1$ atm and $T = 1{,}000$ K. The PRF is set at 10 kHz and the inter-electrode gap distance between anode (A) and cathode (C) is set at $d = 4.5$ mm. The transversal flow of air (flowing from right to left) has a velocity of 1.2 m.s^{-1}.*

Typical current and voltage waveforms are presented in Figure 1.3, also from the thesis of Pai (2008). In this example, NRP discharges are pulsed at a PRF of 30 kHz, in air at atmospheric pressure and a temperature of 1,000 K, flowing with a velocity of 1.2 m.s^{-1}. The inter-electrode gap distance is 5 mm. Discharges in (a) are in the NRP glow regime as defined by Pai et al. (2009) while discharges in (b) are in the NRP spark regime, as defined by Pai et al. (2010a). Both are displayed in Figure 1.2. Plasmas in the NRP corona regime present current and voltage waveforms similar to the ones in NRP glow regime.

The voltage peak is larger for case (a) with NRP glow discharges compared to case (b) with NRP spark discharges. This is due to the phenomenon of streamer breakdown where a conductive channel is formed between the electrodes of the circuit, thus reducing the resistance of the inter-electrode gas (see Figure 1.2). As the maximal current that can be supplied by the generator is reached, the

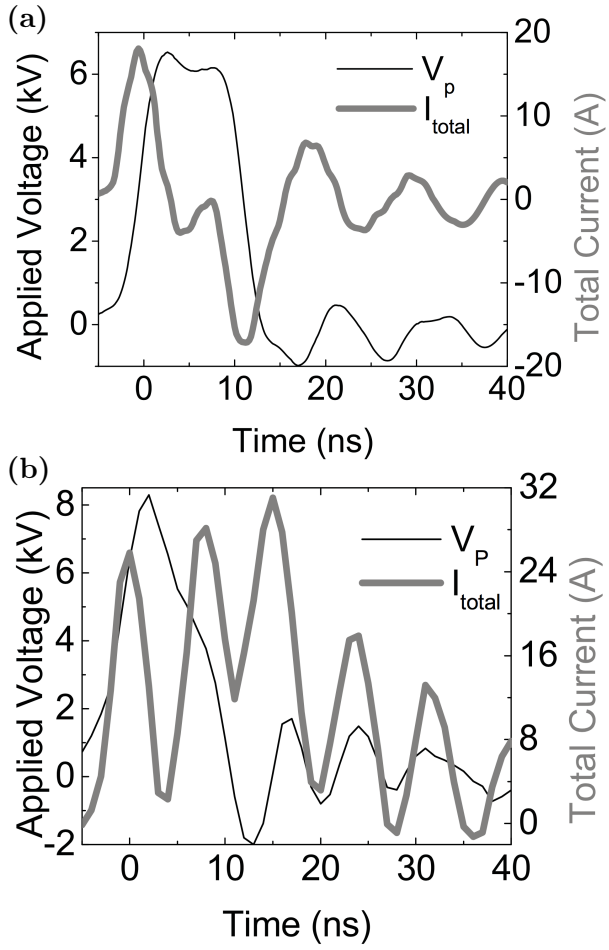

Figure 1.3: *Comparison from Pai (2008) of voltage, V_{p} (thin line), and total current, I_{total} (thick line), waveforms, for NRP discharges pulsed at a PRF of 30 kHz in an air flow of 1.2 $m.s^{-1}$ velocity. The discharges in (a) are in the NRP glow regime and the discharges in (b) are in the NRP spark regime. Air velocity between the electrodes is 1.6 $m.s^{-1}$ and its temperature is 1,000 K. The inter-electrode gap distance is 5 mm and the PRF of the discharges is 30 kHz.*

high voltage cannot be sustained anymore, resulting in the reduction of the full width at half maximum of the voltage peak from 12 to 8 ns. The waveform of the total current evolves also with the NRP regime considered: the current for NRP glow discharges is close to the form of a purely capacitive current while the one of NRP spark discharges displays several positive peaks.

Plasmas generated from NRP discharges (commonly called NRP plasma discharges) lead to two different effects. Both of them are interesting for many applications. The first effect is the heating induced by the plasma, also called thermal effect; the second effect is the generation of ions, radicals, and ac-

tive species, also called chemical effect of the discharges. These thermal and chemical effects are discussed in Sections 1.2.1.1 and 1.2.1.2.

1.2.1.1 Thermal effect

As mentioned above, because of the transient nature of NRP discharges, only a small amount of the input energy goes to heating of the heavy particles constituting the gas, while the largest amount of energy goes to chemistry, *i.e.* generation of ions, radicals and excited species. Rusterholtz et al. (2013) conducted an experimental investigation focusing on the process of ultrafast heating of the gas by NRP spark discharges. This ultrafast heating process takes place at the nanosecond time scale through excitation of the ground-state nitrogen molecules in air:

$$N_2(X) + e^- \rightarrow N_2(A, B, C) + e^-. \tag{1.2}$$

The generated excited nitrogen molecules in turn dissociates oxygen molecules into atomic oxygen, a process that releases a significant amount of heat through the following quenching reaction:

$$N_2(A, B, C) + O_2 \rightarrow N_2(X) + 2\,O + \text{heat}. \tag{1.3}$$

This ultrafast heating is studied for NRP spark discharges in air at atmospheric pressure and temperature of 1,000 K and brings to light an increase in gas temperature of about 900 K within 20 ns. The mechanism of ultrafast heating provides, on the one hand, a source of atomic oxygen promoting oxidation of hydrocarbon molecules in the case of reactive mixtures; on the other hand, the significant heat release accompanying reaction (1.3) leads to a rise in the pressure, resulting in the propagation of an expansion wave followed by a shock wave. The temporal evolution of this hydrodynamic expansion has been quantitatively measured and analysed by Xu et al. (2011); Xu et al. (2014) with the Schlieren technique and has, by comparison to numerical simulations, shown that the fraction of energy transferred to ultrafast heating (ranging from 25 to 75 % in the experimental configuration of the study) is a function of the reduced electric field, as defined in Equation (1.1), and of the initial gas temperature. The fraction of transferred energy increases with these two parameters.

The thermal effect of NRP glow discharges in a combustion environment is investigated by Lacoste et al. (2017a); Lacoste et al. (2017c) where the influence of NRP glow discharges on the temperature of a M-shape laminar premixed methane-air flame ($\Phi = 0.95$) at ambient conditions of temperature and pressure is determined by CARS (Coherent Anti-Stokes Raman Spectroscopy) measurements. Application of NRP glow discharges modifies the shape of the

flame front (detected by CH^* chemiluminescence, see Figure 1.4(a) and (b)), yet the increase in temperature of the flame remains within the range of uncertainty for the diagnostic technique ($\pm 40\,K$). Since the NRP glow discharges have a low thermal effect, their actuation of the flame is thus attributed mostly to chemical activation of the gas.

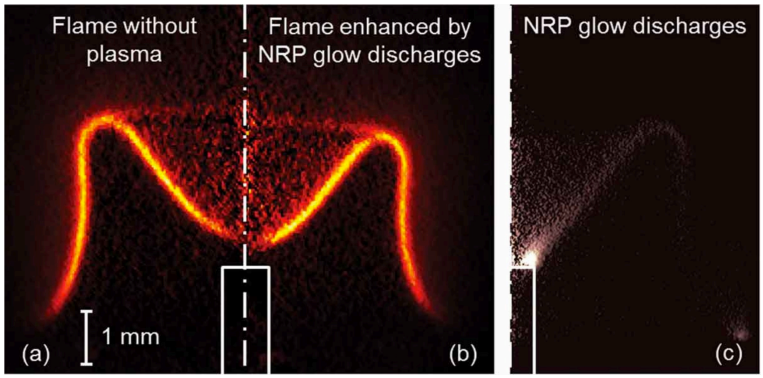

Figure 1.4: *Abel-inverted images of the (a) CH^* chemiluminescence emission of a flame, (b) CH^* emission of a flame enhanced by NRP glow discharges and (c) N_2^* emission of the NRP glow discharges. Images from Lacoste et al. (2017c).*

The thermal effect of NRP corona discharges has not yet been investigated but, since this type of plasma discharge features lower energies, an even lower thermal effect is expected, compared to the glow discharges. There is a need for more precise diagnostic methods in order to measure it precisely, or numerical simulations with flame-plasma coupling.

1.2.1.2 Chemical effect

The chemical effect of NRP discharges is a subject often addressed in the literature. Most of the species produced by non-thermal plasmas in air present interesting properties, especially when considering combustion applications, on which the present work focuses. As mentioned in Section 1.2.1.1, application of NRP discharges in air results in the production of atomic oxygen from excited nitrogen quenching (see Equation (1.3)). Atomic oxygen can also result from direct electron-impact dissociation (see Cosby 1993; Laporta et al. 2014; Laporta et al. 2015):

$$O_2 + e^- \rightarrow 2\,O + e^-. \tag{1.4}$$

Atomic oxygen occupies a most significant position in the mechanism of hydrocarbon oxidation (described for instance in Law 2006), hence the interest of using NRP plasma discharges for combustion applications.

The generation of excited oxygen molecules, in particular the Singlet Delta Oxygen (SDO) molecule, $O_2\left(a^1\Delta_g\right)$, from non-thermal plasma discharges has been investigated several times over the last decade (see Hicks et al. 2005; Ionin et al. 2007; Bowman et al. 2014) because of its potential in decreasing ignition delay times, as demonstrated by Popov (2011) in hydrogen-oxygen stoichiometric mixtures at atmospheric pressure and a range of temperatures from 300 to 1,000 K. In this numerical study, addition of 1 % of SDO molecules to ground-state molecular oxygen leads to a reduction in ignition delay time of the mixture of up to one order of magnitude. This effect is attributed to the role of SDO molecules in chain-initiation and chain-branching reactions:

$$H_2 + O_2\left(a^1\Delta_g\right) \rightarrow OH + OH, \tag{1.5}$$

$$H + O_2\left(a^1\Delta_g\right) \rightarrow OH + O. \tag{1.6}$$

In addition to this effect on ignition delay time, SDO molecules also proved their potential in increasing the laminar propagation velocity of flames. Indeed, Kozlov et al. (2008) have calculated an increase of up to 50 % in the laminar flame speed of a lean hydrogen-air flame for 10 % of SDO in the oxygen. In terms of hydrocarbon mixtures, an experimental study by Ombrello et al. (2010a) reports an increase of 5 % in the laminar burning velocity of stoichiometric ethylene-air flames for an SDO content of 3,000 ppm in oxygen.

Ozone molecules are of interest to combustion applications because of their potential in enhancing the flame speed, as reported by Ombrello et al. (2010b), where an enhancement in the flame speed of lifted stoichiometric propane-air flames of up to 20 % was observed for an addition of 5,000 ppm of ozone in the unburnt gas. Ozone production from non-thermal plasma has been validated with different types of discharges (see Kogelschatz et al. 1988; Chen and Davidson 2002; Mericam-Bourdet et al. 2012). The action of ozone in a combustion area is linked to the following three-body decomposition reaction:

$$O_3 + M \rightarrow O + O_2 + M, \tag{1.7}$$

taking place in the pre-heat zone of a flame and leading to the production of atomic oxygen which, as mentioned above, contribute to the process of fuel oxidation. Ozone also reacts with atomic hydrogen during the fuel oxidation process to form hydroxyl radicals (OH). These radicals take part in the fuel oxidation process of hydrocarbon molecules as well. An experimental-numerical study by Singleton et al. (2016) investigates the effect of air humidity on the production of ozone by nanosecond plasma discharges in a lean ($\Phi = 0.8$) ethylene-air mixture at a pressure of 2 atm and a temperature of 473 K. The experiments are in good agreement with simulations combining a one-dimensional

detailed temporal evolution of the reduced electric field of the discharge and a zero-dimensional Boltzmann equation solver for each species of interest. Ozone density is measured by UV absorption with a UV LED and a photodiode detector equipped with a bandpass filter centred around 250 nm. The nanosecond spark discharges have a duration of 12 ns, a voltage amplitude of 40 kV and result in a deposition of energy per pulse of 50 mJ.pulse^{-1}. Figure 1.5 displays the experimental results of the temporal evolution of ozone density after a 12-ns discharge in a lean ($\Phi = 0.8$) ethylene-air mixture with various water contents.

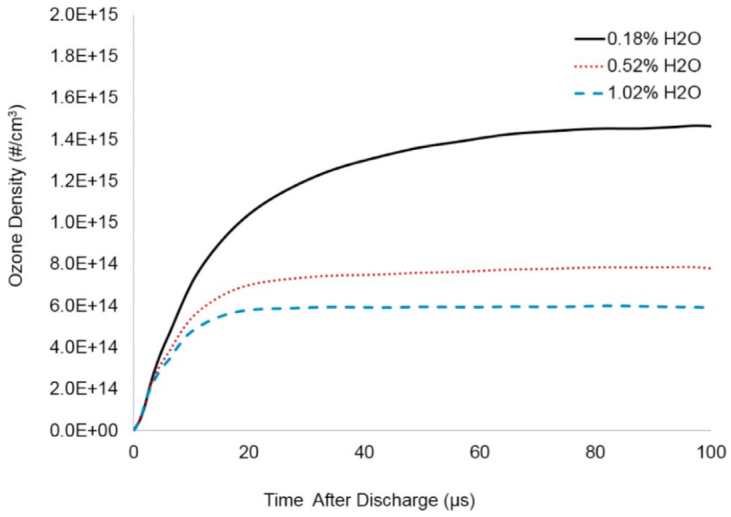

Figure 1.5: *Measured temporal evolution of ozone particle density in a lean ($\Phi = 0.8$) ethylene-air mixture at 2 atm and 473 K. The streamer discharges have a duration of 12 ns, a voltage amplitude of 40 kV, and feature deposited energies of 50 mJ.pulse^{-1}. Taken from Singleton et al. (2016).*

This experiment shows the potential of nanosecond plasma discharges in producing a high amount of ozone (in the order of 10^{15} cm^{-3}). Figure 1.5 also highlights the role of humidity in the fresh gas mixture, which plays a significant role on the measured ozone density. This is due to the fact that, as atomic oxygen is produced by the NRP discharges, it recombines with water molecules into hydroxyl radicals:

$$\mathrm{O} + \mathrm{H_2O} \rightarrow 2\,\mathrm{OH}, \tag{1.8}$$

rather than reacting with molecular oxygen, which would have resulted in ozone production by the following three-body reaction taking place at ambient temperature:

$$\mathrm{O} + \mathrm{O_2} + \mathrm{M} \rightarrow \mathrm{O_3} + \mathrm{M}. \tag{1.9}$$

Additionally to these oxygen-related species, plasma discharges excite the nitrogen molecules in air (this is the origin of the violet light emission from plasma

discharges in air, as seen in Figure 1.2). Because of their high concentration in air and their role in the production of atomic oxygen by the quenching reaction (1.3), excited nitrogen molecules are significant for the precise modelling of plasma discharges in air so that numerous studies focus on establishing the reaction rates for electron-impact excitation of nitrogen (see for instance Gillan et al. 1996; Vojnovic et al. 2015). The dissociation of nitrogen from plasma discharges can also lead to formation of nitric oxides, omnipresent molecules in today's challenge regarding pollutants emission; thus the production of dissociated nitrogen is also a significant topic (see Kumar and Ghosh 1993).

Nitric oxides are a major concern because of their health hazards [1] and their role in the ozone layer depletion, in which nitric oxide reacts with the ozone in the stratosphere as follows:

$$O_3 + NO \rightarrow O_2 + NO_2. \tag{1.10}$$

Emission of this chemical compound is one of the main issues in any combustion application involving air molecules. NO production from NRP discharges in the spark regime is investigated by Kim et al. (2006). The discharges have durations of 10 ns, voltage amplitudes of 5 kV and PRFs between 15 and 50 kHz. Radial single point measurements are performed with a gas analyser placed 10 mm above the nozzle of the burner for three different equivalence ratios of the methane-air mixture: $\Phi = 0$, 0.33 and 0.49. The results are displayed in Figure 1.6 and highlight the fact that the nanosecond plasma discharges in pure air can lead to concentrations in nitric oxides up to 120 ppm (see blue curve), *i.e.* higher concentrations than the lethal dose of 100 ppm.

Another work from Bak and Cappelli (2015) investigates the kinetics of NO formation in reactive mixtures at ambient conditions ($p = 1$ atm and $T = 300$ K). This numerical study is divided in two parts: in the first, the products of NRP discharges with a duration of 10 ns, an amplitude of 5.3 kV and a PRF of 30 kHz are determined on the basis of a zero-dimensional model of a methane-air mixture ($\Phi = 0.55$). In the second part, the results of the first calculation are used as initial conditions for a one-dimensional combustion simulation of a premixed methane-air flame. Figure 1.7 displays the temporal evolution of several products of the NRP discharges for the zero-dimensional discharge computation at (i) constant volume and (ii) constant pressure conditions. The concentrations obtained at constant volume are higher than the ones at constant pressure but the former are only valid for times lower than the gas expansion time following the NRP spark discharge (of a few hundreds of nanoseconds, see Xu et al. 2014). Atomic oxygen and hydroxyl radicals reach concentrations of about 10^{17} cm^{-3} at constant pressure, while the concentrations in carbon monoxide

[1] the Center for Disease Control—CDC—sets the dose for the category Immediately Dangerous to Life or Health—IDLH—at a concentration of 100 ppm

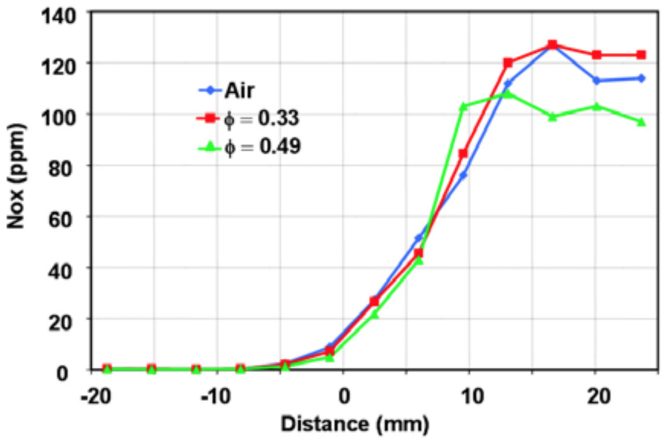

Figure 1.6: *NO concentration along the radial direction at a height of 10 mm above the nozzle of the burner for three different equivalence ratios of the methane-air mixture. Study performed by Kim et al. (2006).*

and nitric oxide at the same condition of constant pressure are a bit lower (1 and $4 \times 10^{16}\,\mathrm{cm}^{-3}$).

Since pollutant emissions represent a major issue in the field of combustion, nitric oxide generation by NRP discharges is further addressed in Section 1.2.2.3 where the main applications of NRP plasma discharges to combustion are discussed.

1.2.2 NRP discharges for plasma-assisted combustion

In the past two decades, NRP discharges have been increasingly applied to combustion processes. Through numerical and experimental studies, the discharges have shown a potential for lowering the lean ignition limit for combustion, extending the stability domains of a flame, modifying the flame's pollutants emission, controlling thermoacoustic pressure fluctuations. These effects are obtained with an input electrical energy of only a few percents of the thermal power of the flame. Some of these studies are presented in this section.

1.2.2.1 Plasma-assisted ignition

One common—and probably the most famous—instance of ignition per electrical discharge is the spark ignition in internal combustion (IC) engines where a spark plug produces a discharge in order to ignite a fuel-air mixture. The mech-

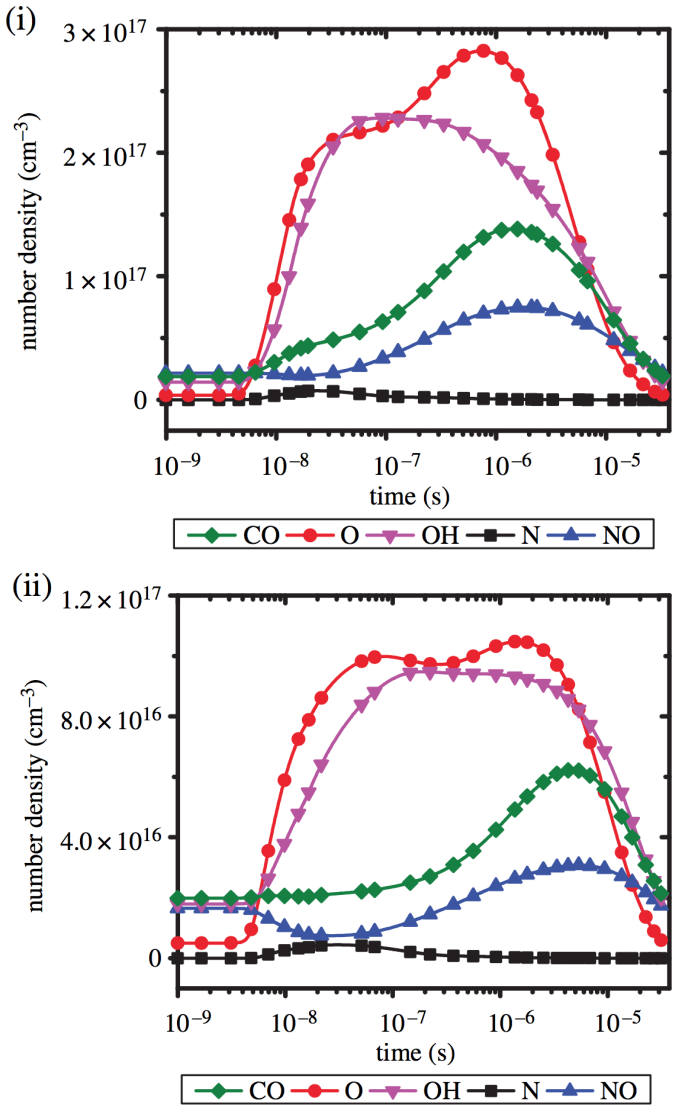

Figure 1.7: *Temporal evolution of the products of NRP discharges in a methane-air ($\Phi = 0.55$) mixture for (i) constant volume and (ii) constant pressure conditions. Taken from Bak and Cappelli (2015).*

anism leading to the ignition in the IC engine is mostly linked to the release of heat, though the fluid particles in the mixture are also chemically activated (generation of ions, radicals and excited fluid elements).

Recently, non-equilibrium plasma discharges have shown their potential for ignition of a wide range of sub- and supersonic combustible flows. A study from Pancheshnyi et al. (2006) demonstrates the efficiency of NRP plasma discharges as an igniter for propane-air mixtures from 0.35 to 2 bars. Figure 1.8

shows an example of ignition assisted by NRP plasma discharges: the propane-air mixture at an equivalence ratio of 0.7 is confined in a closed volume, where the initial pressure is 2 bars, and ignited by a train of ten NRP discharges of 1 mJ energy each, pulsed at a PRF of 30 kHz between two electrodes separated by a distance of 1.5 mm. The afterglow of the discharge is visible at 1.5 ms; it is followed by the flame front propagation which is intensified by the shock wave produced by the plasma discharge, leading to hot spot formation 6 ms after the discharge.

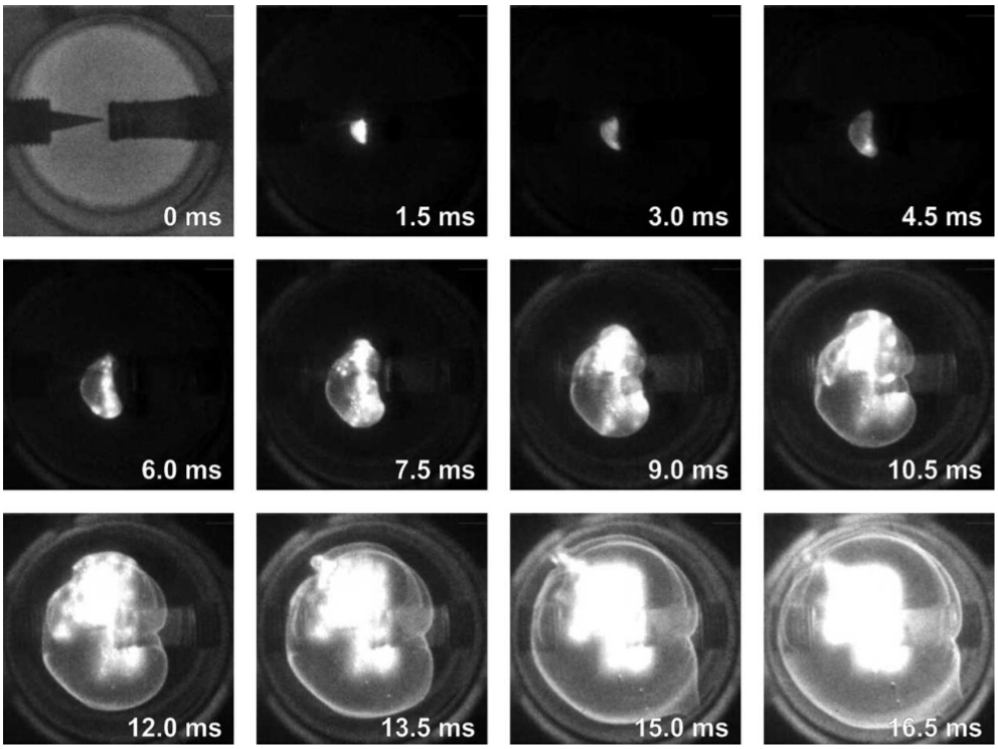

Figure 1.8: *Plasma afterglow and flame propagation in a 2-bars, 0.7-equivalence ratio propane-air mixture. The gap distance between the electrodes is 1.5 mm and the total ignition energy is 10 mJ. Frame rate is 667 Hz and exposure time is 33 µs. Image taken from Pancheshnyi et al. (2006).*

More recently, an experimental work by Sun et al. (2013) investigates the ignition and extinction characteristics of methane-oxygen diffusion counterflow flames diluted in helium under the influence of nanosecond plasma discharges. The pulses are applied between the two burner nozzles so that the plasma discharges find themselves in the fresh gases, in the flame itself, and in the burnt gases. The experiments prove that application of NRP discharges, under certain conditions, induces the classic ignition-extinction S-curve of the flame to give way to a new, fully-stretched ignition curve (see Figure 1.9) in which no hysteresis effect exists between ignition and extinction. This result suggests

that application of nanosecond plasma discharges provides new chemical pathways of fuel oxidation, even at low temperature. Experimental results indeed show that ignition could occur with local maximum temperatures as low as 900 K, compared to the conventional ignition temperature in counterflow burners, usually around 1,200 K.

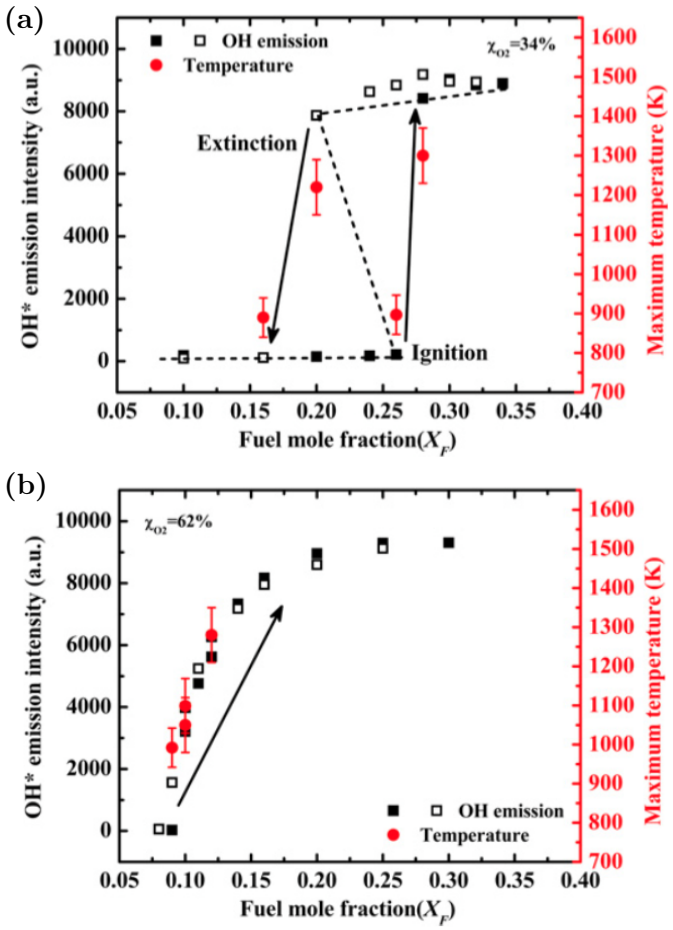

Figure 1.9: *Relation between normalised OH* emission intensity, maximum temperature in the reaction zone, and fuel mole fraction. The pressure is 9,600 Pa, the strain rate is 400 s^{-1} and the repetition frequency of the pulsed nanosecond discharges is 24 kHz. In (a), the oxygen fraction in the helium/oxygen mixture is 0.34 and the traditional ignition-extinction S-curve with its hysteresis is observed. In (b), the oxygen fraction is 0.64 and the ignition-extinction curve is fully stretched. Study by Sun et al. (2013).*

The past decade has been marked by a steady effort to improve the understanding of the mechanisms governing the interactions between plasma chemistry, heat generation and flame ignition. Literature reviews from Adamovich et al. (2009); Starikovskiy and Aleksandrov (2013); Ju and Sun (2015a) already exist

and report the potential applications of non-equilibrium plasma discharges for ignition of combustible mixtures and high-speed flow control. Among the cited non-equilibrium discharges, nanosecond discharges stand as one of the most promising techniques.

1.2.2.2 Extension of flame stability domain

NRP discharges have a potential in extending the stability domain of a flame. The lean extinction limit of a premixed propane-air swirl flame is compared without and with NRP discharges in a combustor with the geometry and nominal conditions representative of an aeronautical combustion chamber by Barbosa et al. (2015) and displays the extension of flame stability domains in both primary and secondary combustion chambers. The NRP discharges have durations of 10 ns, voltage amplitudes of 14 kV and are pulsed at a PRF of 30 kHz. Figure 1.10(a) displays the evolution of the extinction equivalence ratio in the primary stage of the burner, Φ_p, and of the global extinction equivalence ratio, Φ_g, as a function of the primary propane flow rate, with and without application of NRP discharges. It is observed that the nanosecond discharges allow the flame to exist at a much lower fuel flow rate—thus at a much lower thermal power of the flame—compared to the extinction flow rate without discharge. Indeed, the equivalence ratios at which flame extinction occur are $\Phi_p = 2.05$ and $\Phi_g = 0.4$ without NRP plasma discharges; they become $\Phi_p = 0.57$ and $\Phi_g = 0.11$ when NRP discharges are applied. Figure 1.10(b) displays CH^* chemiluminescence images of the flame without (left) and with (right) application of NRP discharges (the red filament in the flame is the glowing from the electrode). This visual comparison shows that the plasma discharges induce no significant change in the shape of the flame between the global equivalence ratios of 0.47 and 0.41. NRP discharges allow a short, compact flame to remain attached to the injection plane, even when its equivalence ratio is below the extinction limit of the flame without NRP discharges ($\Phi = 0.4$). This extension of the flame stability domains has been obtained with NRP discharges featuring only 0.7 % of the thermal power of the flame. However, it is necessary to adapt the pulse repetition frequency to the velocity of the fresh gas mixture, so as to ensure that the whole of the gas flowing through the burner's nozzle is in contact with the plasma discharges.

1.2.2.3 Emission of pollutants

NRP discharges are known to alter the emission of certain products of hydrocarbon combustion. As mentioned in Section 1.2.1.2, the production of nitric

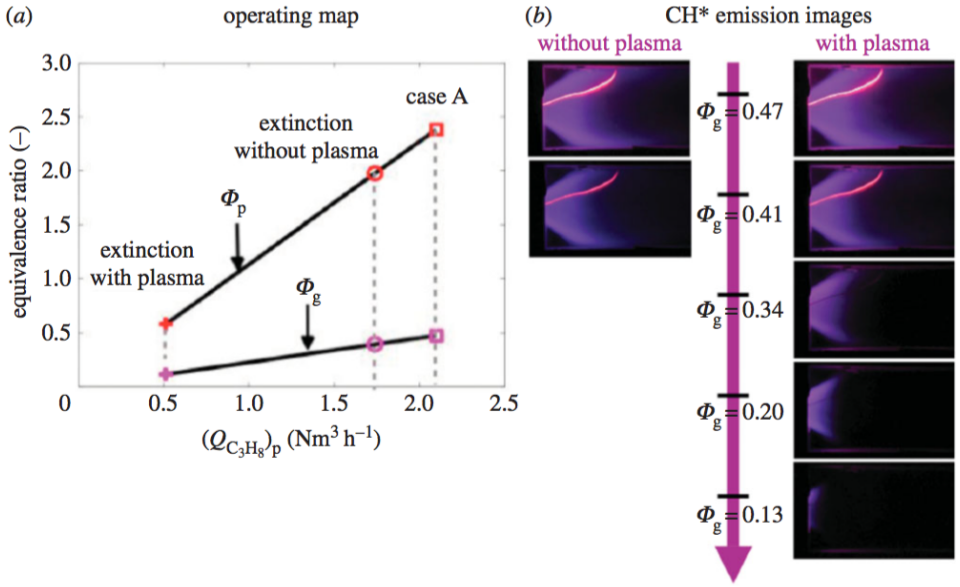

Figure 1.10: *(a) Stability domains of the burner without and with NRP plasma discharges, displayed through the lean-limit equivalence ratios of the primary stage,* Φ_p*, and of the combustion chamber,* Φ_g*. (b) Comparison of CH* emission of the flame and plasma discharges. The PRF is 30 kHz, the air flow rate is maintained constant at* $Q_{air} = 105\,Nm^3.h^{-1}$*. Taken from Barbosa et al. (2015).*

oxide (NO) from nanosecond discharges was measured by Kim et al. (2006) for methane-air mixtures with three different equivalence ratios, see Figure 1.6. The nanosecond discharges lead to a maximum NO concentration of 120 ppm in pure air (blue curve), which remains the same for an air-methane mixture at $\Phi = 0.33$ (red curve). However, when the equivalence ratio of the mixture becomes high enough for ignition, the concentration of NO in the gases decreases to a maximum value of 100 ppm (green curve). This is attributed to the consumption of a part of the plasma-produced nitric oxide by the flame. When the equivalence ratio is further increased towards stoichiometric condition, the NO production is found to increase again with the equivalence ratio. This is attributed to the NO production resulting from the thermal mechanism, which is enhanced by the higher flame temperature when the equivalence ratio is increased. These experimental data are compared with the results yielded from a code for flame computation, supplemented with an initial plasma-generated pool of radicals (see Kim et al. 2007); the results of which show a good agreement with the experimental NO concentrations.

An experimental work of Lacoste et al. (2013a) investigates the influence of NRP spark discharges on the averaged densities of NO, NO_2 and CO of premixed lean natural gas-air ($\Phi = 0.62$) swirl flames. NRP discharges of a duration

of 10 ns, an amplitude of 10 to 20 kV and a PRF between 5 and 40 kHz are applied upstream of the flame, and the burnt gases are analysed by absorption spectroscopy in the infrared to determine CO concentrations and in the ultraviolet to detect NO and NO_2. The evolution of these three species concentrations with the PRF of the NRP discharges is displayed in Figure 1.11. The NO_2 and the CO contents do not vary with the PRF of the discharges while the concentration in NO increases significantly, from 2 ppm without NRP discharges to 27 ppm with NRP discharges pulsed at 30 kHz, a setting which yields a mean electrical power of the discharges of 180 W. For comparison, the thermal power of the flame is 50 kW. The significant increase in the NO concentration is attributed to thermal NO production resulting from ultrafast heating of the gas provided by the spark discharges. Figure 1.12 displays the evolution of NO concentration in the burnt gases as a function of the number of applied pulses per unit mass of air. The NO concentration in the burnt gases depends on the number of discharges per gram of air alone and does not depend on the PRF.

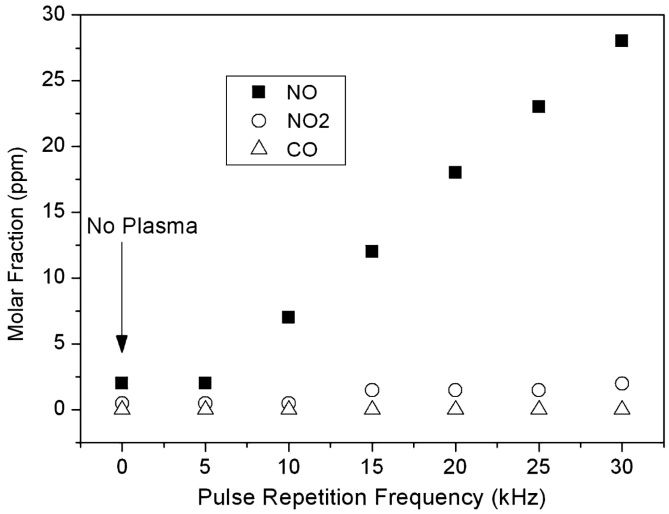

Figure 1.11: *Influence of the PRF of NRP discharges on the concentrations in NO, NO_2 and CO in the burnt gases of a natural gas-air lean swirled flame. Figure taken from Lacoste et al. (2013a).*

1.2.2.4 Control of thermoacoustic pressure fluctuations

Combustion instabilities in propulsion systems and gas turbines have been a subject of research for several decades now. These instabilities result from a trilateral interaction involving velocity fluctuations occurring in the burner. The velocity fluctuations induce oscillations in the flame's heat release rate which themselves couple with the acoustic modes of the combustion chamber, leading to potentially intense pressure fluctuations which can cause severe drawbacks

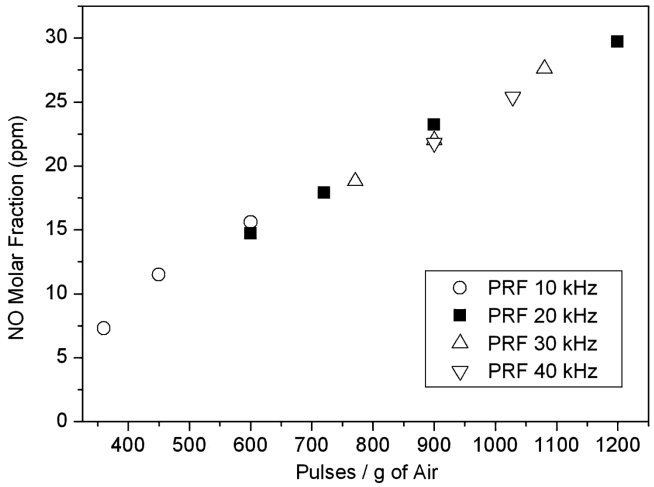

Figure 1.12: *Influence of the number of applied pulses per unit mass of air on the NO concentration for several PRF of the NRP discharges. Figure taken from Lacoste et al. (2013a).*

ranging from decreased combustion efficiency to complete engine failure and structural damage to the combustor. The study of the mechanisms underlying combustion instabilities is inherently complex due to the interactions between fluid dynamics, unsteady heat release rate and pressure fluctuations.

The understanding of this phenomenon has been gradually improved over the years by a decoupling of the interactions taking place in the combustor. The Flame Transfer Function (FTF) has been identified as one of the key characteristic values, indicating the response of the flame to the acoustic fluctuations of the flow in the combustion chamber:

$$\mathrm{FTF}(\omega) = \frac{\dot{Q}'(\omega)/\bar{\dot{Q}}}{u'(\omega)/\bar{u}}, \tag{1.11}$$

where $\dot{Q}'/\bar{\dot{Q}}$ is the heat release rate fluctuation of the flame and $u'/\bar{u}$ is the velocity fluctuation upstream of the flame for a given frequency, ω.

In order to prevent this phenomenon, two types of control can be applied. The first type is passive control; its principle is the implementation of design changes in the combustor such as modifying the fuel injection scheme, reshaping the flame holder, modifying the combustion chamber's geometry, installing acoustic dampers. All these modifications aim at interfering with the resonant coupling between oscillation of the flame's heat release rate and the acoustic modes of the chamber. Passive control of instabilities is, however, limited through the absence of a dynamic component in the system, and through the lack of adaptability to other types of combustion chambers. Design of passive

control schemes can therefore prove a costly and time-consuming method. Active control schemes, on the contrary, implement a dynamic component (also called actuator). Mcmanus et al. (1993) provide a review on active combustion dynamics control. It underlines the importance of several criteria, such as the time-response of the control system; this time has to be adapted to the characteristic time of the dynamic instability. The review also distinguishes systems featuring constant transfer functions (fixed-parameter controllers) and the ones capable of optimizing their action (adaptive controllers).

Recent studies have demonstrated the effect of NRP discharges on combustion instabilities. Moeck et al. (2013) implement an open-loop control scheme on a nominally unstable flame. This open-loop scheme causes a reduction in the instability amplitude by one order of magnitude for an input electrical power of the discharges representing less than 1 % of the thermal power of the flame. This effect of NRP discharges on the flame dynamics is also brought to light by Lacoste et al. (2013b) and linked to a modification of the flame transfer function (FTF, see Equation (1.11)) of the flame. After decomposition of the FTF into gain, G and phase, φ:

$$\mathrm{FTF}(\omega) = G(\omega)\, e^{i\,\varphi(\omega)}, \tag{1.12}$$

the effect of nanosecond discharges on both of these values is demonstrated, as shown in Figure 1.13 where NRP plasma discharges of a duration of 10 ns, PRF of 30 kHz and mean electrical power of 40 W are pulsed in the unburnt mixture of a turbulent lean premixed swirl flame with an equivalence ratio of 0.7 and a thermal power of 4 kW.

NRP discharges increase gain and phase in certain ranges of frequencies while decreasing them in others. Images of CH* chemiluminescence of the flame confirm visually this influence of NRP discharges on flame dynamics. A comparison of the flame diameter at different heights for the case without and with plasma discharges highlights the fact that application of NRP discharges tends to reduce the wrinkling of the flame by 10 to 15 %, a value which varies depending on the phase of the acoustic period.

Response of laminar premixed methane-air flames to different types of forcing is investigated by Lacoste et al. (2017b). The response of three types of flame (conical, M-shape and V-shape) in terms of the FTF is compared for forcing by acoustic waves, by AC electric fields and by NRP glow discharges. The effects provided by these three forcing sources are different: the AC electric field indeed generates an acceleration of the charged species in the reaction front, attributed to a modification in the flow field alone (since no thermo-diffusive wrinkling of the flame surface is observed), while the influence of forcing by NRP glow discharges was attributed to a local increase in the burning velocity caused by the chemical effect of the discharges (as mentioned in Section 1.2.1.2,

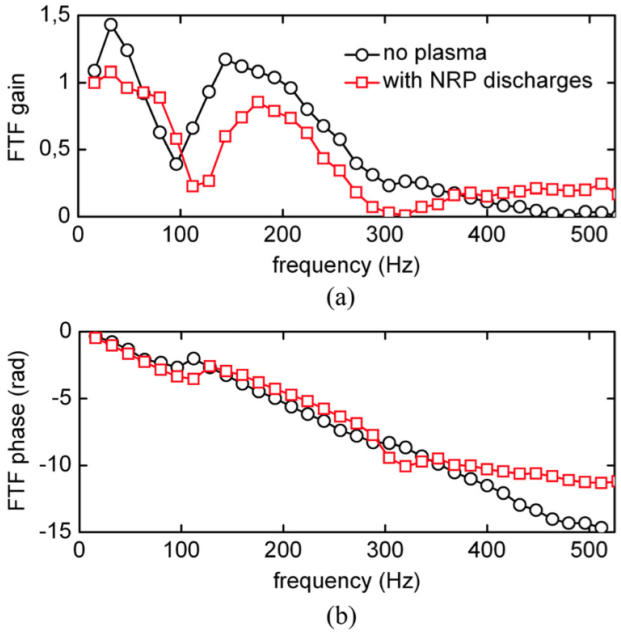

Figure 1.13: *FTF of a swirl-stabilised lean ($\Phi = 0.7$) premixed methane-air flame ($P_{\mathrm{th}} = 4\,kW$; $S = 0.53$) with (red squares) and without (black circles) application of NRP plasma discharges in the NRP spark regime ($PRF = 30\,kHz$; $P_{\mathrm{el}} = 40\,W$). Taken from Lacoste et al. (2013b).*

the thermal effect of NRP glow discharges in this configuration has been proved as being small, see Lacoste et al. 2017c). The geometry of the flame influences its response to acoustic waves and NRP glow discharges, especially in terms of the FTF gain. Figure 1.14 displays the M- and V-shaped flames (a) without and (b) with application of NRP glow discharges. From this figure, it can be seen that the plasma energy distribution changes with the geometry of the flame: the discharges are indeed more homogeneously distributed on the flame front in the case of a M-shaped flame, while the luminous emission is mostly concentrated at the rod in the centre of the flame in the case of a V-shaped flame.

NRP discharges have proved their potential in controlling combustion instabilities; however, knowledge on the interactions between inlet flow, heat release rate of the flame and NRP discharges still has to be improved in order to comprehend and properly optimise the control schemes to their maximum efficiency. While the influence of NRP discharges on the three phenomena (flow field fluctuation, unsteady heat release rate and pressure fluctuations) at the root of thermoacoustic instabilities has been proved, the mechanisms governing these effects, as well as the influence of these phenomena themselves on NRP plasma discharges still need to be understood.

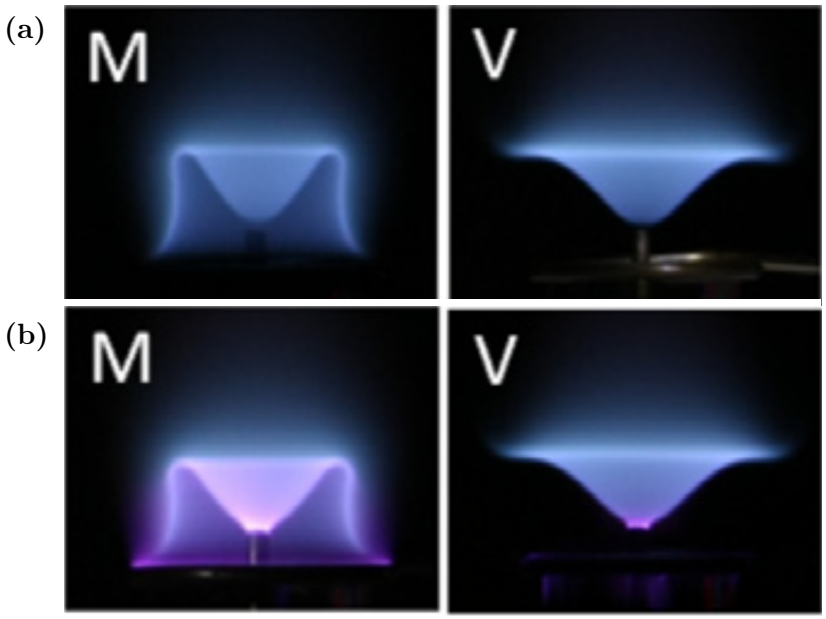

Figure 1.14: *M-shaped (M) and V-shaped (V) flames (a) without and (b) with application of NRP glow discharges. Image taken from Lacoste et al. (2017b).*

1.2.3 Conclusion

A lot of studies have already proved the strong effect of NRP discharges on many different combustion problems. However, there is still a lack of understanding in the fundamental processes taking place, especially in terms of quantification of these effects. Displaying these effects and quantifying them is the main goal of this study.

Chapter 2

Effect of flow on NRP discharges

The effect of various air flow parameters on the plasma regimes of nanosecond repetitively pulsed (NRP) discharges is investigated at atmospheric pressure. The two electrodes are in a pin-annular configuration, transverse to the mean flow. The NRP corona to NRP spark (C-S) regime transition and the NRP spark to NRP corona (S-C) regime transition are investigated for different steady and harmonically oscillating flows. First, the strong effect of a transverse flow on the C-S and S-C transitions, as reported in previous studies, is verified. Second, it is shown that the azimuthal flow imparted by a swirler does not affect the regime transition voltages. Finally, the influence of low frequency harmonic oscillations of the air flow, generated by a loudspeaker, is studied. A strong effect of frequency and amplitude of the flow modulation on the NRP plasma regime is observed. Results are interpreted based on the cumulative effect of the NRP discharges and an analysis of the residence times of fluid particles in the inter-electrode region. This study was done in the laboratoire Énergétique Moléculaire et Macroscopique, Combustion (EM2C) in the École Centrale Paris (ÉCP), France. The results of this experimental study have been published in Heitz et al. (2016).

2.1 Introduction

Numerous applications make use of non-equilibrium plasma discharges in an atmospheric pressure air (or air-containing) flow. Among them, a significant number is related to bio-medical applications (see Kovalova et al. 2014; Collet et

al. 2014; Kong et al. 2009; Hirst et al. 2014), surface processing (see Massines et al. 2012; Stauss et al. 2010), gaseous treatment (see Nozaki et al. 2004; Mericam-Bourdet et al. 2012; Zhang and Cha 2015) or combustion enhancement (see Adamovich et al. 2009; Starikovskiy and Aleksandrov 2013). Although there is a strong mutual coupling between gaseous flow and plasma, most academic and industrial studies mainly focus on the effect of plasma on the flow.

One of the most spectacular effects of non-equilibrium plasmas on gas dynamics is the generation of ionic wind. Colas et al. (2010); Rickard et al. (2005); Debien et al. (2012) have studied different configurations in order to increase the velocity of the ionic wind, also called electric wind. The physical mechanism of this effect has also been modeled by Likhanskii et al. (2008); Lagmich et al. (2008), and the electrohydrodynamic force can be predicted. Ionic wind generated by plasma discharges can be used to modify an oscillating air flow. Kopiev et al. (2014) gives an example by controlling shear layer flow instabilities triggered by acoustic forcing in a turbulent air jet with three types of plasma actuators. This control was achieved through a variation in the phase shift between the signals driving the loudspeaker and the plasma actuator. A change in the velocity profile in the shear layer of the jet was also observed. Spark discharges can also affect the flow by thermal expansion, as displayed by Xu et al. (2011); Haley et al. (1989). The ultrafast heating of the gas (up to several thousand Kelvin) generates shock waves followed by expansion waves that eventually increase local turbulence.

Although effects of plasma on the flow are relatively well-known, effects of the flow on plasma discharges have scarcely been investigated. In argon, studies of Evans (1967); Bogaerts et al. (2002); Li et al. (2009) report on the significant influence of the gas flow on the discharge properties, such as breakdown voltage and gas heating. In low-pressure hydrogen, Chabert et al. (1998) found a strong effect of the flow on the dissociation degree of a microwave discharge, but a relatively weak influence on the gas temperature.

In air, a few studies (see Jaworek and Krupa 1996; Pereira et al. 2014) have shown the significant effect of a transverse air stream on the characteristics of positive corona and dielectric barrier discharges. For example, it was shown that for cold plasmas, the breakdown voltage increases with the bulk velocity and that the momentum transfer can be affected by the direction of the flow. It was also shown that the discharge regime can be affected by the gas velocity. Recently, Bálek et al. (2014) studied the effect of an acoustic field on a negative corona discharge in air at atmospheric pressure. They found that an intense acoustic field (with velocity fluctuations up to $25\,\mathrm{m.s^{-1}}$, in a frequency range from 24 to 100 Hz) can significantly affect both the stability and the spatial

organization of the negative corona or transient spark discharges. An explanation of their experimental results based on transport properties and thermal instabilities of the plasma was proposed. However, all these previous studies on the effect of an air flow on the discharge behavior dealt with relatively low power plasmas. Typically, with a current up to 30 mA and a minimal thermal impact, the corona or dielectric barrier discharges investigated have limited relevance for applications such as plasma-assisted combustion. The impact of transverse flows and acoustic waves on the organization and regime transition of non-equilibrium thermal air plasmas such as Nanosecond Repetitively Pulsed (NRP) spark discharges, laser sparks or radio-frequency discharges has never been investigated.

In this chapter, we focus on the influence of a transverse stream, eventually modulated by harmonic acoustic waves, on the breakdown voltage and the regime transitions of NRP discharges in air, at atmospheric pressure. Previous studies have shed light upon key parameters governing the regime of NRP plasma discharges. The gas temperature, the inter-electrode gap distance, the Pulse Repetition Frequency (PRF), as well as the electrode geometry have been established as relevant parameters by Pai et al. (2010b). In this work, effects of a steady laminar air stream with a Reynolds number lower than 1,300 is first assessed by investigating the NRP corona to spark (C-S) and the NRP spark to corona (S-C) transition voltages dependence to changes of the axial or azimuthal velocity components of the incoming flow. The effect of axial acoustic forcing is then examined. Finally, an explanation for the observed results, based on the cumulative effect of the NRP discharges and the residence time of the flow particles in the inter-electrode area is proposed.

2.2 Experimental setup

2.2.1 The test-rig

The experiments are performed in an atmospheric pressure test-rig shown in Figure 2.1. A flow of air at room temperature, controlled by a flowmeter (EL-Flow, Bronkhorst) enters the experimental setup at its bottom. The air flows through a perforated plate and a honeycomb which are not shown in Figure 2.1. It then enters a converging section. These elements are used to laminarize the flow and reduce the boundary layer thickness leading to a top hat velocity profile at the converging nozzle outlet. An element with or without radial swirling vanes is also placed in between the converging nozzle and the cylindrical tube to set the flow in rotation in the azimuthal direction or not. Three swirlers featuring different blade angles: 0 ° (no rotation of the flow), 34 °, and 48 ° were

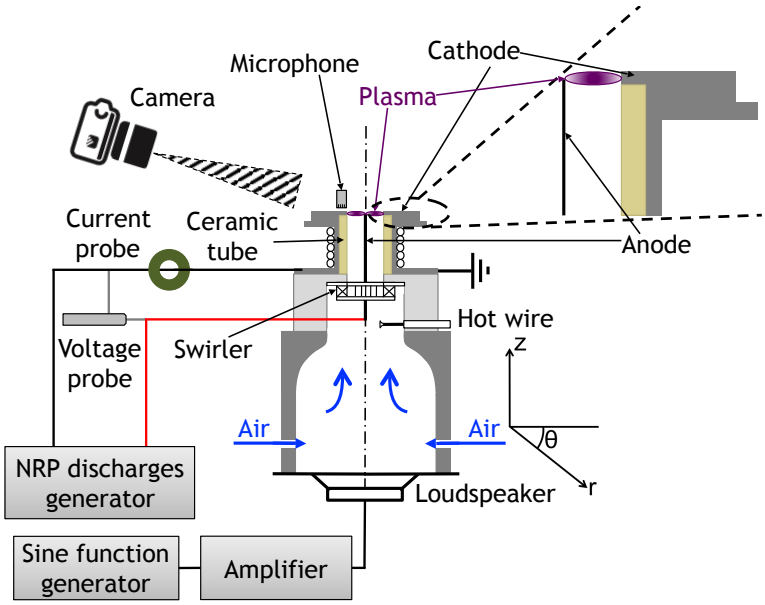

Figure 2.1: *Schematic of the experimental setup and zoom on the inter-electrode area.*

used in these experiments. The element carries also a small central cylindrical bluff body of 2.6 mm diameter made of stainless steel, which is flush-mounted with the injection tube outlet.

The NRP plasma discharges are generated between two stainless steel electrodes, in a pin-annular configuration. Figure 2.1 provides a zoom on the inter-electrode area to allow a better description of the electrode configuration. The anode corresponds to the central bluff body described above. The cathode is an annular ring of $D = 17.9$ mm diameter and $h = 1.2$ mm height. The gap distance between the anode and the cathode is therefore $d = 7.7$ mm. Upstream of the cathode, a cylindrical piece of ceramic with the same external diameter ($D = 17.9$ mm) is flush-mounted with the metallic ring to prevent parasitic discharges inside the injection tube. Both electrodes are connected to a high-voltage pulse generator (FPG Series, FID Technologies). The pulses have an amplitude in the range of 3.5 to 15 kV, last 10 ns with a pulse repetition frequency that has been set to either PRF = 15 or 30 kHz.

A loudspeaker (SPH-115, Monacor, with a power of 80 W) at the bottom of the setup is connected to a signal synthesizer (TGA1200 Series, Aim & TTi) and a Hi-Fi amplifier (RA-04, Rotel). These elements are used to generate harmonic acoustic waves at controlled amplitudes and frequencies. The forcing frequency is varied between $f_{ac} = 16$ and 192 Hz, and the velocity amplitude in the inter-electrode region is evaluated by using a hot wire and ranges from

$u'_z = 0$ to $3\,\mathrm{m.s^{-1}}$.

2.2.2 Instrumentation

Electrical measurements are performed with a voltage probe (PPE 20 kV, LeCroy) and a current probe (Model 6585, Pearson Electronics) attenuated with a low-voltage attenuator (2-20, Barth Electronics). The voltage and current signals are recorded with an oscilloscope (1 GHz WavePro 7000A Series, LeCroy). The methodology to deduce the deposited energy per pulse is provided in Appendix A. Figure 2.2 displays the temporal evolution of current, I, voltage amplitude, U, and energy per pulse, E_p, for a high-voltage pulse of a NRP corona discharge, averaged over 1,000 pulses.

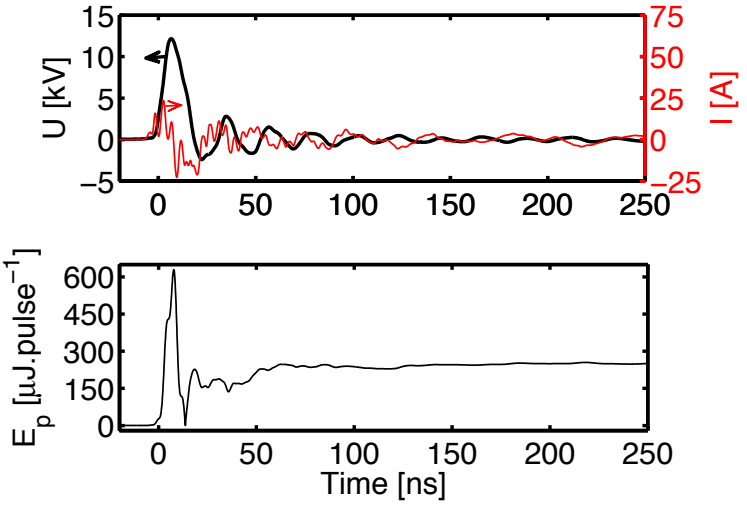

Figure 2.2: *Temporal evolution of the current, I (upper graph, red line), voltage amplitude, U (upper graph, black line), and energy per pulse, E_p (lower graph), of a NRP corona discharge averaged over 1,000 pulses.*

Imaging of the discharges organization in the inter-electrode region is realized by collecting the plasma light emission in the visible range with a camera (D7000, Nikon) equipped with a glass lens. The exposure time is between 0.02 s and 3.20 s, the sensitivity is kept constant and set to ISO 1600 and the aperture is set to f/25.

The velocity of the air flow is measured with a hot wire (55P16, Dantec Dynamics) located upstream of the swirler. Measurements of the velocity in the inter-electrode area is obviously not possible with a hot wire during plasma generation. Section 2.2.3.2 describes how the velocity in the inter-electrode

area is determined from measurements upstream of the swirler. The hot wire had to be calibrated prior to the measurements; this procedure for calibration is detailed in Appendix B.

Finally, acoustic pressure measurements close to the inter-electrode area are made with a microphone (Type 4138, Brüel & Kjær) and a preamplifier (Type 2670, Brüel & Kjær) connected to a conditioning amplifier (Type 2690 Nexus, Brüel & Kjær). Setting the microphone in the manner depicted in Figure 2.1 is intrusive but will not significantly affect the pressure oscillation in the inter-electrode area.

2.2.3 Experimental procedure

2.2.3.1 Steady air flow

For steady flow conditions, experiments are carried out to analyse the impact of the velocity on the plasma regime. The velocity profile in the inter-electrode area is thus determined when the hot wire is set 2 mm above the outlet of the injection tube. This intrusive sensor is mainly sensitive to the norm of the velocity component of the flow perpendicular to the hot wire. Assuming that the radial velocity component of the swirling flow can be neglected, the hot wire is oriented so as to successively measure the mean axial, $\bar{u}_z$, and mean azimuthal, $\bar{u}_\theta$, velocity components of the swirling jet exhausting the injection tube. These measurements are carried out for the two swirlers with 34 ° and 48 ° blade angles, designated by medium swirl and strong swirl in the following. The resulting u_z and u_θ under a steady air flow are calculated according to:

$$\bar{u}_z = \frac{2}{R^2 \Delta t} \int_0^R \int_0^{\Delta t} r\, u_z\,(t;r)\; dt\, dr, \tag{2.1}$$

$$\bar{u}_\theta = \frac{2}{R^2 \Delta t} \int_0^R \int_0^{\Delta t} r\, u_\theta\,(t;r)\; dt\, dr. \tag{2.2}$$

where $R = 9\,\text{mm}$ is the radius of the inter-electrode area and $\Delta t = 16\,\text{s}$ is the signal acquisition time. The velocity $\bar{u}_z$ corresponds to the bulk velocity in the injection channel.

Spatially and temporally averaged velocity components are calculated as follows:

$$\bar{u}_z^r = \frac{2}{R^2} \int_0^R r\, u_z\,(t;r)\; dr, \qquad \bar{u}_z^t = \frac{1}{\Delta t} \int_0^{\Delta t} u_z\,(t;r)\; dt, \tag{2.3}$$

$$\bar{u}_\theta^r = \frac{2}{R^2}\int_0^R r\, u_\theta\,(t;r)\; dr, \qquad \bar{u}_\theta^t = \frac{1}{\Delta t}\int_0^{\Delta t} u_\theta\,(t;r)\; dt. \tag{2.4}$$

Results are presented in Figure 2.3 for two different swirlers and the same bulk velocity of $1.42\,\mathrm{m.s^{-1}}$ in the annular gap of the injection tube. Figure 2.3(a) shows the local axial velocity profiles and Figure 2.3(b) presents the local azimuthal velocity profiles for the two tested swirlers. The sign of the signal was adjusted across the symmetry axis of the system for the azimuthal velocity component. The strongly swirled flow reaches higher axial and azimuthal peak velocities than the moderately swirled flow. The axial velocities both feature a M-shaped profile with about the same minimum velocity of about $0.5\,\mathrm{m.s^{-1}}$ on the burner axis. This velocity defect in the centre flow originates from the wake of the central bluff body and from the negative axial pressure gradient due to the swirling flow. The azimuthal velocity component features a Rankine-like vortex profile except near the burner axis. The hot wire is not suited for velocity measurements in this low azimuthal velocity region and the contribution from the axial flow might be of the same order of magnitude. Away from this region, the radial and azimuthal velocity gradients increase between the medium and strong swirl cases. The main observation is that the two swirlers allow to impart an azimuthal component to the flow with a peak velocity roughly equal to half the axial peak velocity of the jet.

Measurements of NRP corona to spark (C-S) and spark to corona (S-C) regime transition voltages are first made in a configuration with a purely axial flow (swirler with $0\,^\circ$ blade angle) by changing the flow rate of air. The range of explored bulk flow velocities, $\bar{u}_z$, in the inter-electrode gap is indicated in Table 2.1 together with the Reynolds number, Re, calculated as:

$$Re = \frac{\bar{u}_z\, D_h}{\nu_{\mathrm{air}}}, \tag{2.5}$$

where $\bar{u}_z$ is the bulk flow velocity, as defined in Equation (2.1), D_h is the hydraulic diameter of the inter-electrode area and $\nu_{\mathrm{air}} = 1.59\times10^{-5}\,\mathrm{m^2.s^{-1}}$ is the kinematic viscosity of air at atmospheric pressure and ambient temperature. The value of the hydraulic diameter is determined, in the current configuration, as:

$$D_\mathrm{h} = \frac{4\,S}{P} = D - d, \tag{2.6}$$

where S and P are the surface and perimeter of the inter-electrode area, and D and d are the diameter of the nozzle and of the high-voltage electrode, respectively.

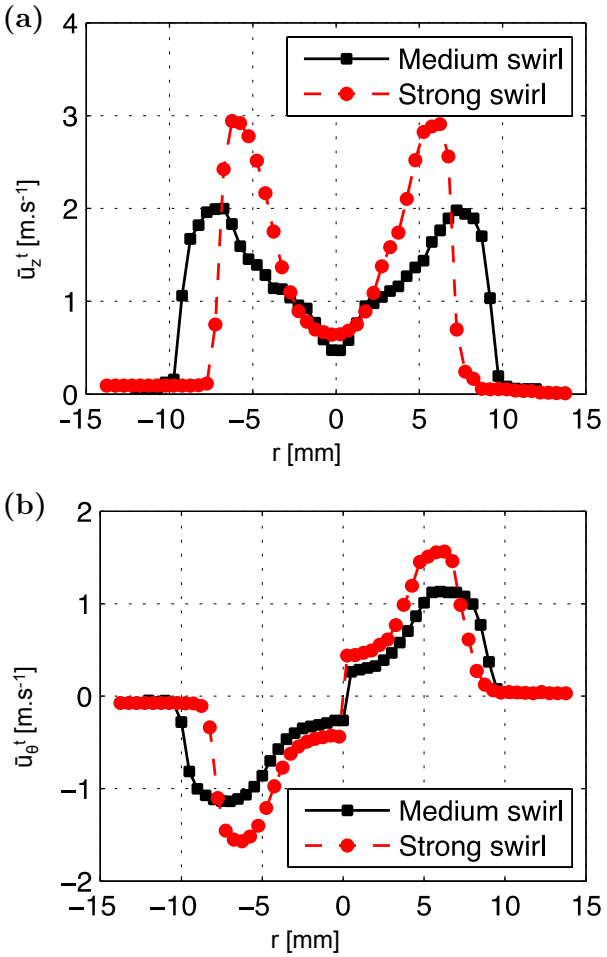

Figure 2.3: *(a) Axial and (b) tangential velocity profiles for two types of swirlers in the test-rig: the medium swirler (solid black lines) and the strong swirler (dashed red lines). The value of the bulk velocity is* $\bar{u}_z = 1.42\,m.s^{-1}$.

Table 2.1: *Velocities in the inter-electrode area,* $\bar{u}_z$*, for the regime transition voltages study in a steady air flow and corresponding Reynolds numbers, Re. The hydraulic diameter is* $D_h = 15.3\,mm$ *and the viscosity of the gas is* $\nu_{air} = 1.59 \times 10^{-5}\ m^2.s^{-1}$.

$\bar{u}_z$ (m.s^{-1})	Re (.)
0.33	318
0.66	636
1.00	963
1.33	1,281

For a fixed bulk flow velocity, the inter-electrode voltage is slowly increased, so as to visually reach transition from NRP corona discharges to NRP spark

discharges (C-S). This transition could not be detected for bulk flow velocities higher than $\bar{u}_z = 1.33\,\mathrm{m.s^{-1}}$ due to the limited maximum amplitude of the high voltage pulses of 15 kV. The voltage is then decreased until the reverse (S-C) transition takes place. The measurements are repeated thrice and averaged results are presented. The error bars in the following figures correspond to the maximum differences observed between these three measurements. Effect of swirl is then examined in a second set of experiments for two fixed flow rates corresponding to $\bar{u}_z = 0.33$ and $1.00\,\mathrm{m.s^{-1}}$.

2.2.3.2 Harmonically oscillating air flow

Effects of acoustic forcing on the NRP discharge regime are examined without swirl ($S = 0$). The investigated conditions are summarized in Table 2.2. The amplitude of the voltage pulses is chosen to obtain NRP corona discharges close to the transition to NRP spark discharges.

Table 2.2: *Sets of experimental conditions used for the determination of the influence of an oscillating flow on NRP plasma discharges.*

Label of the set	$\bar{u}_z$ ($\mathrm{m.s^{-1}}$)	PRF (kHz)	U (kV)
1st set	1.42	30	12.75
2nd set	0.81	30	12.02
3rd set	0.81	15	13.93

For each set of conditions in Table 2.2, the amplitude of the acoustic forcing is slowly increased from zero to a level where a C-S transition is observed. If the amplitude is increased further, the plasma regime returns to NRP corona discharges (S-C transition). The hot wire, placed far enough from the walls, at the converging nozzle outlet, is used to deduce the velocity signal in the inter-electrode gap and the corresponding mean and root mean square (RMS) values of this signal for the C-S and S-C transitions. These calculations are based on mass balance for low-frequency acoustic waves leading to a conservation of the acoustic volume flow rate over an axial distance which is short compared to the acoustic wavelength. The cross-sectional area at the converging nozzle outlet being 3.36 times larger than the cross section in the inter-electrode region, the velocity measured at the convergent exhaust needs to be multiplied by 3.36 to determine the velocity in the inter-electrode annulus.

Predictions are compared in Figure 2.4 with direct measurements in the inter-electrode region in the absence of plasma for two forcing frequencies: (a) $f_{\mathrm{ac}} = 40\,\mathrm{Hz}$ and (b) $f_{\mathrm{ac}} = 80\,\mathrm{Hz}$. The signals are well superimposed.

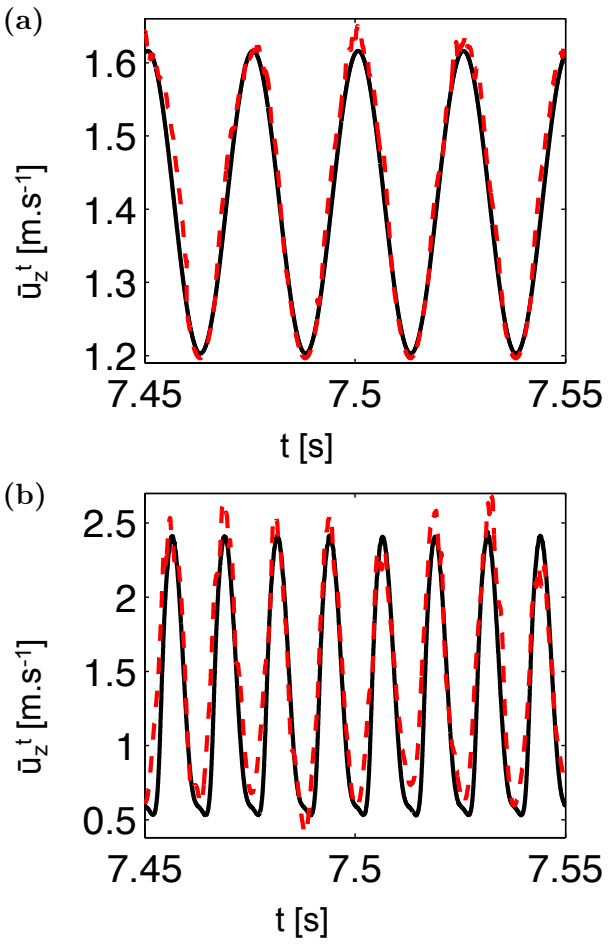

Figure 2.4: *Temporally averaged velocity signals for two acoustic forcing frequencies: (a) 40 Hz and (b) 80 Hz. The velocity upstream of the swirler (solid black lines) was multiplied by the ratio of cross-sectional areas, 3.36, to compare it with the velocity measured in the inter-electrode area (dashed red lines). The mean value of the velocity, $\bar{u}_z$, is 1.42 m.s^{-1}.*

2.3 Results

2.3.1 Steady air flow

Effects of the air velocity on NRP plasma discharges are first assessed by the direct visualizations of the inter-electrode area presented in Figures 2.5(a) to 2.5(d), with the camera positioned so as to visualize the inter-electrode area. The inter-electrode voltage is kept constant in these experiments and set to $U = 12.46$ kV while the PRF is set to 30 kHz. Figure 2.5(a) corresponds to a case

without flow (within quiescent air). Figures 2.5(b), (c) and (d) correspond to resulting axial velocities in the inter-electrode area of, respectively, $0.81\,\mathrm{m.s^{-1}}$, $0.81\,\mathrm{m.s^{-1}}$ and $1.42\,\mathrm{m.s^{-1}}$. There is no azimuthal velocity in cases (b) and (d), and (c) is obtained with medium swirl, which induces an azimuthal velocity component of $0.29\,\mathrm{m.s^{-1}}$.

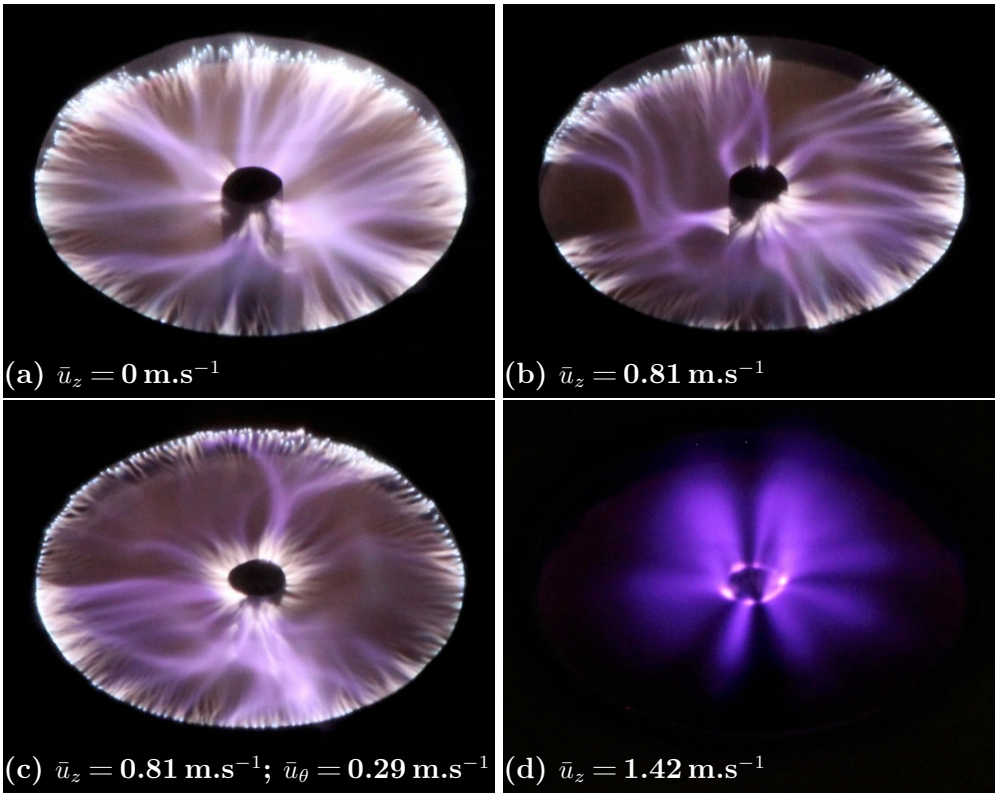

Figure 2.5: *Photographs of the NRP plasma discharges obtained for different flow conditions with pulse voltage amplitude of 12.46 kV and a PRF of 30 kHz. Pictures (a), (b) and (c) were taken with an exposure time of 0.02 s, while picture (d) was taken with an exposure time of 3.20 s.*

In Figure 2.5(a) (without flow), the NRP plasma discharges are in the spark regime as defined by Pai et al. (2010a), and are well distributed around the whole surface of the anode. The luminous intensity is higher and the sparks are more uniformly distributed than in Figure 2.5(b), obtained for a bulk velocity of $\bar{u}_z = 0.81\,\mathrm{m.s^{-1}}$. In this case, the discharges mainly start from the edge of the anode and reach the whole surface of the cathode. In Figure 2.5(c), the NRP spark discharges look similar as in Figure 2.5(b) but they mainly reach the upper part of the cathode. In these three figures, the exposure time of the camera was set to 0.02 s, allowing 600 pulses at a PRF of 30 kHz to be imaged. In Figure 2.5(d), the NRP discharges are in the corona regime, as defined by Pai et al. (2010b), and the exposure time had to be significantly increased

(to 3.20 s) to obtain a good image quality, corresponding to a visualization of 96,000 pulses at the same PRF of 30 kHz. In these experiments, it was observed that the NRP discharges transit directly from spark to corona; the intermediate NRP glow regime, as defined by Pai et al. (2009), does not appear.

These figures clearly indicate that an air stream and swirl significantly affect the organization as well as the regime of the NRP plasma discharges. An inter-electrode area with no air motion, as in Figure 2.5(a) favours the presence of NRP spark discharges. This can be explained by the fact that a constant air flow, as in Figures 2.5(b), (c) and (d), prevents the accumulation of the effects of successive plasma pulses. By only considering this phenomenon, it is clear that the residence time of the fluid particles convected by a transverse air flow within the inter-electrode region will determine the number of air particles treated by the plasma pulses (by addition of heat and active species). If they are transported faster out of the inter-electrode area, this cumulative effect of NRP discharges is reduced, lowering the probability of the creation of NRP spark discharges. This scenario is retained here to interpret the following results.

2.3.1.1 Impact of an axial stream

Effects of a mean bulk flow on the C-S and S-C regime transition voltages are presented in Figure 2.6. The voltage, U, for the two considered regime transitions increases with the bulk air flow velocity, $\bar{u}_z$. A hysteresis effect is observed, placing the C-S transition curve (solid black line) at a higher voltage level than the S-C transition curve (dashed red line). The width of the hysteresis region takes values between 1 and 3 kV, depending on the bulk flow velocity.

This phenomenon has already been observed by Jaworek and Krupa (1996), but for DC corona discharges. The authors suggested that the increase in breakdown voltage induced by an air velocity increase is due to an increase in the effective length of the plasma streamers due to their deflection by the air flow. As in our case the length of the discharge channels does not seem to be affected by the flow, as seen in Figures 2.5(b) and 2.5(c), it appears that this explanation does not apply here. These observations are further analysed in Section 2.4.

To validate the analysis of Section 2.4, the results from Figure 2.6 are compared with another set of measurements for the C-S transition. This experiment has been performed by setting a constant inter-electrode voltage, $U = 14.60$ kV. With an axial air velocity set at a value between 0.33 and 1.33 $\mathrm{m.s^{-1}}$, the PRF is increased until the C-S transition is reached. The results are displayed in Figure 2.7 and show a linear influence of the axial air velocity on the PRF to

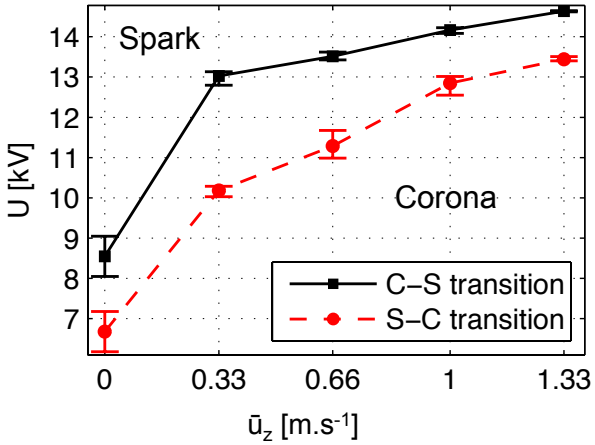

Figure 2.6: *Voltage, U, values for C-S (solid black) and S-C (dashed red) transitions as a function of the bulk flow velocity, $\bar{u}_z$, for a non-swirled air flow ($\bar{u}_\theta = 0$). The PRF is set to 30 kHz.*

reach C-S transition. Note that this experiment has only been performed once, hence the absence of error bars on this figure.

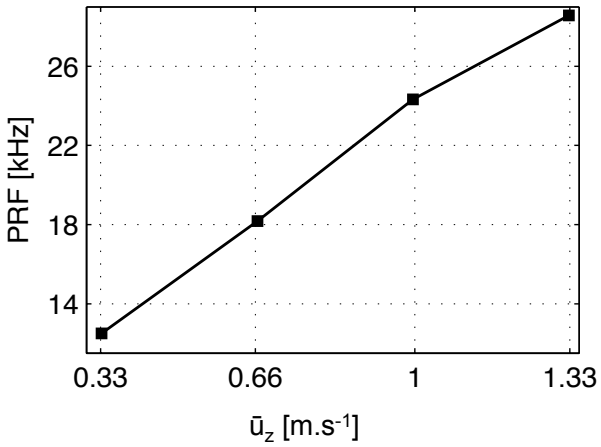

Figure 2.7: *PRF values for C-S transition as a function of the axial velocity, $\bar{u}_z$, for a non-swirled flow ($\bar{u}_\theta = 0$). The inter-electrode voltage, U, is set to 14.60 kV.*

2.3.1.2 Impact of an azimuthal flow

Effects of swirl are now analysed. The C-S and S-C transition voltages are measured in three configurations: without azimuthal velocity, with moderate swirl and with strong swirl. Results are presented for two bulk flow veloc-

ities $\bar{u}_z = 0.33\,\mathrm{m.s^{-1}}$ and $\bar{u}_z = 1.00\,\mathrm{m.s^{-1}}$ in Figure 2.8. The component $\bar{u}_\theta$ indicated in these figures corresponds to the resulting velocity reached by the azimuthal flow in the swirling jet at the injection tube outlet, obtained with Equation (2.2).

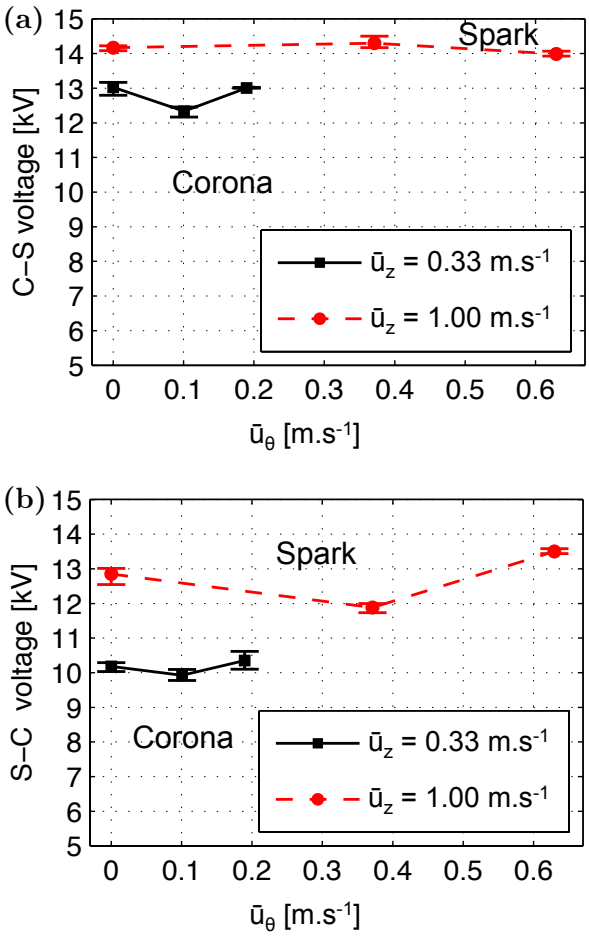

Figure 2.8: *Voltage values (a) for C-S and (b) for S-C transitions. Two axial velocities, $\bar{u}_z$, are considered: $0.33\,\mathrm{m.s^{-1}}$ (solid black lines) and $1.00\,\mathrm{m.s^{-1}}$ (dashed red lines). The PRF of the pulses is constant and set to 30 kHz.*

The voltage amplitudes needed to reach the C-S or the S-C transition are very similar for the three examined configurations. The difference between the transition voltages for the medium and strong swirling flows is indeed small compared to the absolute values of the voltages. The difference is less than 1.6 kV variation for voltages lying between 13 and 15 kV, corresponding to a relative difference of about 12 %. It can be concluded that, in contrast to the NRP spark discharges organization (see Figure 2.5), there is no significant effect of the azimuthal component of the flow on the C-S and S-C transition voltages.

The effect of acoustic oscillations of the flow will thus be investigated only for non-swirling flows.

2.3.2 Harmonically oscillating flow

Experiments with low frequency acoustic forcing are conducted here for a total duration of 16 s. The definition of the mean (or bulk) velocity, $\bar{u}_z$, is given in Equation (2.1). The RMS velocity, u'_z, that is used to estimate the residence time of air particles in the inter-electrode area is expressed as:

$$u'_z = \left(\frac{1}{T} \int_0^T \left(\bar{u}_z^t - \bar{u}_z \right)^2 dt \right)^{1/2}, \tag{2.7}$$

where $\bar{u}_z^t$ is the instantaneous velocity in the inter-electrode region (see Section 2.2.3.2) and $T = 1/f_{\mathrm{ac}}$ is the forcing period of the harmonic signal. The relative RMS velocity is defined as the ratio of the RMS and the mean velocity, $u'_z/\bar{u}_z$. A systematic analysis shows that the relative difference between the reconstructed velocity and its actual measured value lies between 7.53 % and 10.22 % for RMS velocities, between 8.05 % and 13.07 % for mean velocities and between 8.84 % and 12.88 % for relative RMS velocities. The uncertainty in the velocity measurements is therefore considered as smaller than 13 %.

The NRP regime chart is presented in Figure 2.9 as a function of the acoustic forcing frequency f_{ac} and the modulation velocity u'_z when the bulk flow velocity is set to $\bar{u}_z = 1.42\,\mathrm{m.s^{-1}}$. In this figure, the PRF is set to 30 kHz and the voltage is fixed to 12.75 kV. In the first region, designated by (1) and corresponding to relatively low modulation amplitudes, the NRP plasma discharges are in the corona regime. The second region, designated by (2), corresponds to the NRP spark regime, reached for moderate velocity fluctuations. The third region, designated by (3), is reached when the modulation amplitude is further increased; in this region, the NRP discharges return to the corona regime. For forcing frequencies higher than 192 Hz, transition to the NRP spark regime cannot be observed, and the plasma remains in the NRP corona regime, irrespective of the forcing amplitude.

The results presented in the following are given in non-dimensionalised form. The Strouhal number is defined as:

$$St = \frac{f_{\mathrm{ac}}\, h}{\bar{u}_z} \tag{2.8}$$

where $h = 1.2\,\mathrm{mm}$ is the height of the inter-electrode area. The RMS velocity of the acoustic forcing, u'_z, is expressed as the relative RMS velocity by dividing it by the mean velocity of the air flow, $\bar{u}_z$.

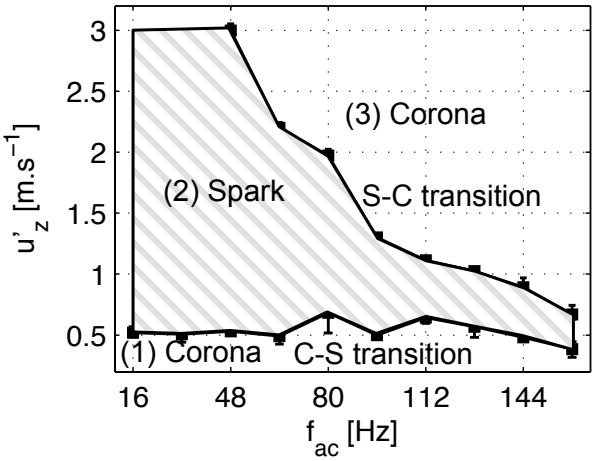

Figure 2.9: *NRP discharges regimes for acoustic forcing frequencies, f_{ac}, varying from 16 to 192 Hz and amplitudes, u'_z, between 0 and 3 $m.s^{-1}$. The bulk flow velocity, $\bar{u}_z$, is set to 1.42 $m.s^{-1}$, the PRF is 30 kHz and the voltage amplitude is 12.75 kV.*

Figure 2.10 compares the relative RMS velocities, $u'_z/\bar{u}_z$, measured (a) for the C-S and (b) for the S-C transitions of NRP discharges for the three experimental conditions defined in table 2.2 as a function of the Strouhal number, St. For a bulk injection velocity of $\bar{u}_z = 1.42\,\mathrm{m.s^{-1}}$ and a PRF of 30 kHz, an air particle is convected, on average, by 47 μm between two pulses. By changing the PRF or the mean resulting axial air velocity, the particle displacement between two NRP discharges is altered, and the displacement of the previously treated air particles is modified, as explained in Section 2.3.1. The C-S transition in Figure 2.10(a) is reached at a similar relative RMS velocity value over the Strouhal number span (corresponding to acoustic frequencies between 16 and 192 Hz). The S-C transition curves (see Figure 2.10(b)) follow another trend: for low Strouhal numbers (typically, for acoustic frequencies lower than 100 Hz) the modulation level required for the S-C transition is much larger than at high Strouhal number. The relative RMS velocities for the transitions are similar for each set of experimental conditions.

2.4 Analysis and discussion

2.4.1 Steady air flow

It was shown in the previous section that the C-S and S-C regime transition voltages increase with the bulk flow velocity (see Figure 2.6), supposedly due to a faster transport of the air particles out of the inter-electrode region. Fig-

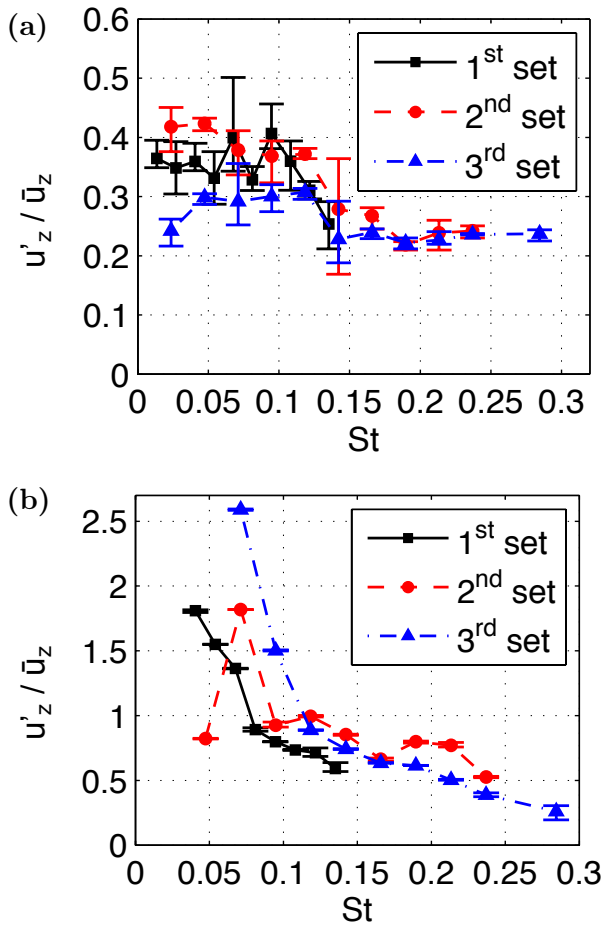

Figure 2.10: *(a) C-S transition and (b) S-C transition curves in terms of the relative RMS velocity and the Strouhal number. Solid black: first set of experimental conditions, dashed red: second set of experimental conditions and dash-dotted blue: third set of experimental conditions, from table 2.2.*

ure 2.11 shows a schematic of this region that spans over a height $h = 1.2\,\mathrm{mm}$, corresponding to the height of the cathode. The mean residence time, t_R, of an air particle in this region is then given by:

$$t_\mathrm{R} = \frac{h}{\bar{u}_z}. \tag{2.9}$$

The residence time multiplied by the PRF yields the number of NRP pulses, n, to which an air particle is submitted when travelling through the inter-electrode region:

$$n = t_\mathrm{R} \times \mathrm{PRF}. \tag{2.10}$$

Table 2.3 makes a synthesis, for a PRF of 30 kHz, of the residence times, t_R, and number of applied pulses on air particles in the inter-electrode area, n, for the range of bulk velocities, $\bar{u}_z$, explored in Figure 2.6.

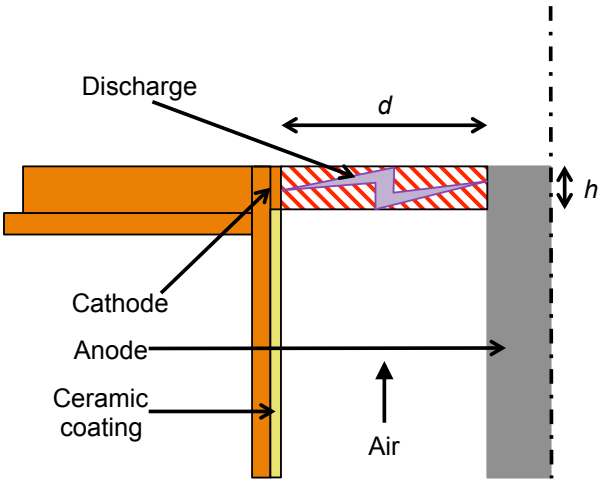

Figure 2.11: *Cross-section of the inter-electrode area at the outlet of the injection tube, where the NRP plasma discharges are generated. The gap distance between the anode and the cathode, d, is 7.7 mm and the height of the inter-electrode area, h, is 1.2 mm.*

Table 2.3: *Mean residence times and number of applied pulses on the particles in the inter-electrode area for the studied bulk velocities. Calculations made with Equation (2.9), with an inter-electrode area height, h, of 1.2 mm and a PRF of 30 kHz.*

$\bar{u}_z$ ($m.s^{-1}$)	t_R (ms)	n (.)
0.33	3.64	109
0.66	1.82	55
1.00	1.20	36
1.33	0.90	27

Increasing the convective transport exposes an air particle to less NRP plasma discharges, thus reduces the cumulative heating and active species production. Increasing the voltage amplitude compensates this effect and increases the heating and active species production induced by individual pulses to reach the transitions presented in Figure 2.6. It is reasonable to assume that the pulse power required to reach a NRP regime transition is inversely proportional to the mean number of applied pulses on air particles during their transit in the inter-electrode area. This hypothesis is checked by turning the parameters in Figure 2.6 non-dimensional and by comparing them with the data from Figure 2.7. The resulting axial air velocity, $\bar{u}_z$, is now expressed as the mean number of high-voltage pulses applied on an air particle in the inter-electrode area, n, defined by Equation (2.10). The inter-electrode voltage for C-S transi-

tion, U, is expressed as the non-dimensional power of the pulses, P^*, expressed as:

$$P^* = \frac{U^2/R_{\text{air}}}{U_0^2/R_{\text{air}}}, \tag{2.11}$$

where $R_{\text{air}} = 1.19 \times 10^{16}\,\Omega$ is the electrical resistance of the considered volume of air (see Figure 2.11) under atmospheric conditions, and U_0 is the inter-electrode voltage required to reach C-S transition in quiescent air. Plotting the product of the non-dimensional pulse power and the number of pulses, $P^* \times n$, as a function of the number of pulses, n, in Figure 2.12 highlights the linear evolution between the two quantities. The data at $\bar{u}_z = 0\,\text{m.s}^{-1}$ have not been included because the number of applied pulses in a quiescent air is hard to quantify (the only air motion results from the thermal expansion of air following a high-voltage pulse). The data from the two experiments presented in Section 2.3.1.1 (the black lines correspond to the data from Figure 2.6 and the red line corresponds to the data from Figure 2.7) superimpose well.

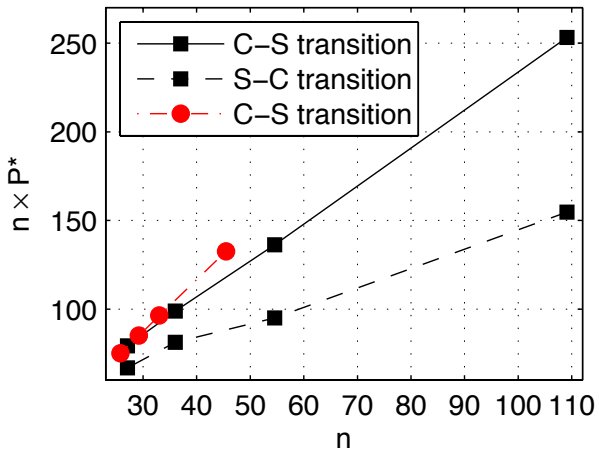

Figure 2.12: *Non-dimensionalised power of the high voltage pulses, P^*, multiplied by the mean number of applied pulses on an air particle in the inter-electrode area, n, as a function of n. The black lines correspond to the experimental data from Figure 2.6 and the red line corresponds to the experimental data from Figure 2.7.*

The following relation between the pulse power, P^*, and the number of applied pulses on an air particle, n, may be deduced:

$$P^* = A + \frac{B}{n}, \tag{2.12}$$

where $A = 2.52$ and $B = 10.95$. The result from Equation (2.12) implies that an increase of the number of applied pulses on the air particles results in a decrease of the required power to reach C-S transition in the inter-electrode area.

However, even with a constant voltage, the properties of the air in the inter-electrode area change after each high-voltage pulse. The energy deposition is then in fact different for each pulse. Thus, the total energy deposition on an air particle that is required to reach a NRP regime transition, $E_{\text{transition}}$, is actually expressed as:

$$E_{\text{transition}} = \sum_{i=1}^{n} E_{p;i} = \sum_{i=1}^{n} \int_{\frac{i-1}{\text{PRF}}}^{\frac{i}{\text{PRF}}} U(t) \times I_i(t) dt, \tag{2.13}$$

where the inter-electrode voltage waverform, $U(t)$, is supposed to remain the same for each high-voltage pulse.

The analysis based on the calculation of the non-dimensional pulse power, P^*, as a function of the square inter-electrode voltage, U^2, is rough and the equivalent electrical circuit of the inter-electrode area is not trivial to model. The modeling of $I(t)$ that is necessary to determine the relative impact of n and U on the C-S and S-C transitions will require further investigations, and is not presented in the current work.

Modifying the azimuthal velocity by imparting swirl to the flow does not alter the residence time inside the inter-electrode region so that air particles are still exposed to the same number of pulses, which is consistent with the results presented in Figure 2.8.

2.4.2 Pressure oscillations induced by acoustic forcing

The effect of acoustic oscillations on the regime transitions is now discussed. Sound waves are accompanied by small fluctuations in pressure and velocity. Their effects on the formation of the discharges are examined separately.

A variation in pressure induced by the acoustic field alters the reduced electric field, E/N, which might, in turn, modify the discharge regime transition (see for instance Rusterholtz et al. 2013):

$$\frac{E}{N} = \frac{U}{d \times N}. \tag{2.14}$$

Here, U is the inter-electrode voltage, d is the gap distance and N is the particle density. Assuming plane wave propagation, sound pressure waves associated with fluctuations of the acoustic velocity with a RMS fluctuation u'_z in the inter-electrode region correspond to pressure fluctuations $p' \simeq Z_0 \times u'_z$, where $Z_0 \simeq 400\,\text{kg.m}^{-2}.\text{s}^{-1}$ is the characteristic impedance of air at atmospheric pressure and room temperature. Due to the relatively large values

taken by $u'_z \leq 3\,\mathrm{m.s^{-1}}$, the corresponding RMS sound pressure levels also reach high values: $p' \leq 1,200\,\mathrm{Pa}$ (*i.e.* 155 dB). This level of fluctuations is however weak compared to the atmospheric pressure $p'/\bar{p} \simeq 10^{-2}$ but could be sufficient to explain a NRP regime transition. We therefore performed pressure measurements with a microphone, to check the pressure variation in our experimental setup during acoustic forcing.

Most favorable conditions for spark formation will take place at the instant of lowest density, thus lowest pressure. The minimum peak of the pressure fluctuation was evaluated for a range of acoustic frequencies from 32 to 160 Hz and for the amplitudes corresponding to C-S and S-C transitions with a bulk velocity of $1.42\,\mathrm{m.s^{-1}}$ and a PRF of 30 kHz. Figure 2.13 presents the results. The error bars take into account the calibration and the sensitivity of the microphone conditioning amplifier; these were estimated at 5 % of the measured pressure value.

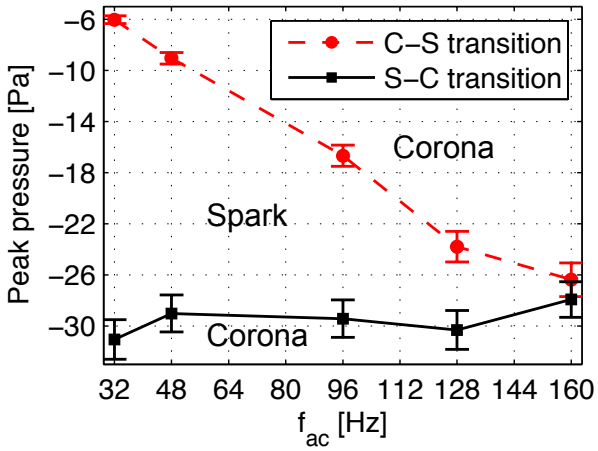

Figure 2.13: *Negative peak pressure measured for C-S transition (dashed red curve) and S-C transition (solid black curve). The harmonic oscillation amplitudes match the ones corresponding to C-S and S-C transitions with a bulk flow velocity of the air of $1.42\,m.s^{-1}$; the NRP discharges are pulsed at a PRF of 30 kHz and a voltage amplitude of 12.75 kV.*

The minimum pressure, which should favour NRP spark discharges, actually corresponds to the S-C transition. The evolution of the measured pressure is therefore not consistent with the expected trend. Furthermore, the minimum pressure resulting from acoustic forcing lies between 6 and 31 Pa below the mean pressure (corresponding to a fluctuation between 55 and 62 dB), far smaller than the expectations. These measured values are very small compared to the atmospheric pressure ($p'/\bar{p} \simeq 10^{-4}$) so that the effect of a temporarily decreased pressure on NRP spark discharge formation can be considered neg-

ligible. Pressure can therefore be ruled out as a significant factor in the NRP regime transitions observed during acoustic forcing of the flow.

2.4.3 Residence times during acoustic forcing

Experiments presented in Section 2.3.2 were carried out for different repetition frequencies and air velocities, at a fixed voltage amplitude. For each set of these experimental conditions, the inter-electrode voltage has been adjusted so as to be close to the C-S transition. Effects of the voltage amplitude are not considered in the following analysis. The breakdown phenomenon depends in a complex and non-linear manner on the inter-electrode voltage, and quantitative modeling of this effect is not attempted. The objective is here to examine whether modifications of the residence time may be used to interpret the transitions observed in Figure 2.9.

The residence time, t_R, is defined as the time that a particle located at a boundary of the inter-electrode domain ($z=0$ or $z=h$) needs to move out of this area, *i.e.* go beyond the upper limit $z>h$. The residence time, t_R, if the air particle was initially located at $z=0$, is thus implicitly defined by:

$$h = \int_{t_1}^{t_1+t_R} \bar{u}_z^t \, dt, \tag{2.15}$$

where t_1 is an arbitrary time in the acoustic forcing period. If the air particle was initially located at $z=h$, the residence time is:

$$0 = \int_{t_1}^{t_1+t_R} \bar{u}_z^t \, dt, \tag{2.16}$$

supposing that the particles are not convected upstream of the inter-electrode area.

The instantaneous axial velocity of the flow, $\bar{u}_z(t)$, can be expressed, in the case of a sine acoustic forcing as:

$$\bar{u}_z^t = \bar{u}_z + u'_z \sqrt{2} \sin\left(\frac{2\pi}{T}\, t\right), \tag{2.17}$$

where $T = 1 \,/\, f_\mathrm{ac}$ is the acoustic period. Because the axial extent of the inter-electrode area is small compared to the acoustic wavelength ($C_\mathrm{air} \,/\, f_\mathrm{ac}$, with C_air the speed of sound in air), which lies between 1.77 and 21.25 m at the low frequencies considered here, the unsteady velocity component can be taken as spatially constant.

Equations (2.15) and (2.16) are then integrated to yield implicit expressions for the residence time:

$$t_{\mathrm{R}} = \frac{h}{\bar{u}_z} + \frac{u'_z}{\bar{u}_z}\frac{T}{\pi\sqrt{2}}\left[\cos\left(\frac{2\pi}{T}\left(t_1 + t_{\mathrm{R}}\right)\right) - \cos\left(\frac{2\pi}{T}\,t_1\right)\right], \tag{2.18}$$

$$t_{\mathrm{R}} = \frac{u'_z}{\bar{u}_z}\frac{T}{\pi\sqrt{2}}\left[\cos\left(\frac{2\pi}{T}\left(t_1 + t_{\mathrm{R}}\right)\right) - \cos\left(\frac{2\pi}{T}\,t_1\right)\right]. \tag{2.19}$$

Equations (2.18) and (2.19) apply for the case that the air particle was initially located respectively at $z = 0$ and $z = h$ and show that, for high frequencies of the acoustic forcing (low T), the effect of the flow modulation will be small so that the residence time is similar to the one without acoustic forcing. The effect of flow modulation on the C-S and S-C transitions therefore decreases with frequency. This is in agreement with the experimental results: it was not possible to obtain NRP spark discharges for frequencies larger than 200 Hz.

The residence time also depends on the relative modulation level, $u'_z/\bar{u}_z$ and t_1.

2.4.3.1 Case without backflow

We first consider the case where the oscillation amplitude is smaller or equal to the mean flow velocity ($u'_z\sqrt{2} \leq \bar{u}_z$). The model detailed here is named Model 0. For this case, an air particle always moves in the direction of the mean flow, and the residence time will be maximum for the following condition (corresponding to a minimum air velocity, see Figure 2.14):

$$t_1 + \frac{t_{\mathrm{R}}}{2} = \frac{3}{4}\,T. \tag{2.20}$$

Then, for the case where the air particle is initially located at $z = 0$, Equation (2.18) gives:

$$t_{\mathrm{R,max}} = \frac{h}{\bar{u}_z} + \frac{u'_z}{\bar{u}_z}\frac{T}{\pi\sqrt{2}}\sin\left(\frac{\pi}{T}\,t_{\mathrm{R,max}}\right). \tag{2.21}$$

Figure 2.15 presents the effect of the acoustic oscillation frequency on the number of applied pulses on air particles for relative RMS velocities $u'_z/\bar{u}_z = 0.21$,

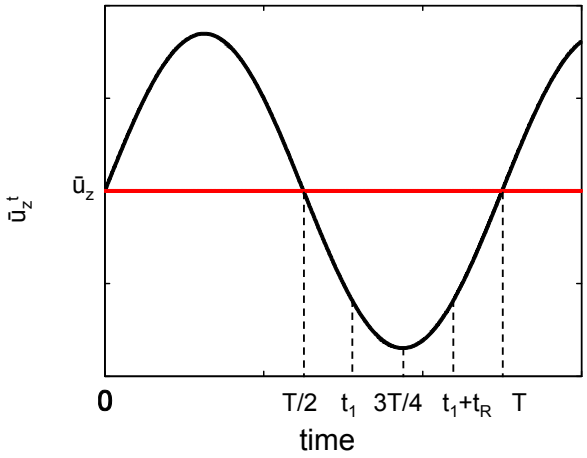

Figure 2.14: *Illustration of the required condition from Equation (2.20) to ensure a maximum residence time of the air particles in the inter-electrode area when* $u'_z\sqrt{2} \leq \bar{u}_z$ *(Model 0).*

0.35 and 0.49 (the mean axial velocity is here set to $\bar{u}_z = 1.42\,\mathrm{m.s^{-1}}$). These values were chosen according to the C-S transition in Figure 2.9. The effect of the oscillation frequency is not significant. The maximum variation is obtained for a relative amplitude of $u'_z/\bar{u}_z = 0.49$, where n only decreases from 80 at $St = 0.01$ to 55 at $St = 0.16$. As a comparison, the number of applied pulses without acoustic forcing is 25. Thus, for any frequency in the range of 16 to 192 Hz, the acoustic forcing significantly increases the residence time of air particles in the inter-electrode area, even at low amplitudes of forcing.

2.4.3.2 Case with backflow

We now consider the case where the acoustic oscillation amplitude is larger than the mean flow velocity ($u'_z\sqrt{2} > \bar{u}_z$). For this case, during a certain part of the acoustic period, the flow velocity is negative and an air particle moves upstream. In order to maximise the residence time, different scenarios are possible, depending on the initial location of the air particle. For an air particle initially located at the lower boundary of the inter-electrode area ($z = 0$), the residence time will be maximum if the particle follows the trajectory depicted in Figure 2.16 (Model 1). Since the considered period, T, of the acoustic forcing is very high compared to the particle residence time in the inter-electrode area, it is not possible for a particle to stay for several acoustic periods in the inter-electrode area. In order to optimize the trajectory (red line), we need to carefully choose t_1 and t_2 for each frequency and amplitude of the oscillation.

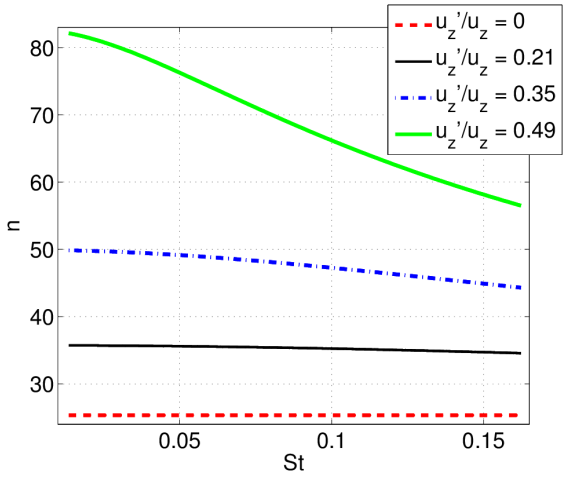

Figure 2.15: *Effect of the Strouhal number, St, on the number of applied pulses on an air particle, n, predicted by Equation (2.21) and calculated from Equation (2.10), for low amplitudes of the forcing, corresponding to Model 0. The mean velocity of the flow, $\bar{u}_z$, is 1.42 m.s^{-1}.*

This ideal trajectory will produce the largest residence time, $t_{\mathrm{R,max}}$, that can be obtained by solving the following system of four equations:

$$\int_{t_1}^{t_1+t_{\mathrm{R,max}}} \bar{u}_z^r \, dt = h \tag{2.22}$$

$$\int_{t_1}^{t_2} \bar{u}_z^r \, dt = 0 \tag{2.23}$$

$$u_z(t_2) = 0 \tag{2.24}$$

$$\frac{du_z}{dt}(t_2) > 0 \tag{2.25}$$

Figure 2.17 presents the effect of acoustic oscillation amplitude and Strouhal number on the number of applied pulses on a particle initially located at $z = 0$. The mean flow velocity is set to 1.42 m.s^{-1}. The hatched area indicates conditions for which Model 1 cannot be applied, meaning that the red trajectory in Figure 2.16 cannot be obtained, the trajectory is then similar to the blue one. In order to explain the S-C transition, *i.e.* for high oscillation amplitudes, this model can only be used for elevated frequencies. From 112 to 192 Hz ($St = 0.1$ to 0.16), the number of applied pulses that can be obtained following Model 1 varies from 150 to 100. The corresponding RMS oscillation amplitudes are 1.6 m.s^{-1} and 1.8 m.s^{-1}, hence a relative RMS fluctuation between 1.1 and 1.3.

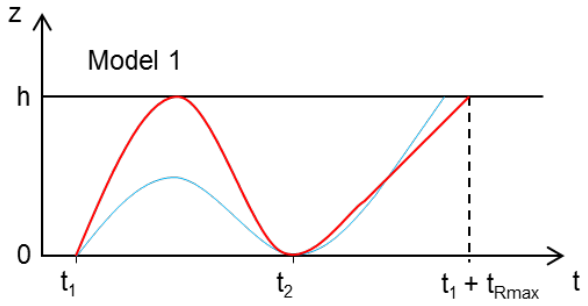

Figure 2.16: *Non-ideal (blue) and ideal (red) air particle trajectories maximising the residence time of an air particle in the inter-electrode area, when it is initially located at $z = 0$, for acoustic oscillation amplitudes larger than the mean velocity.*

These values are slightly larger than the experimental results presented in Figure 2.9; however, the trend is apparent. For high oscillation frequencies, the amplitude has only little effect on the maximum residence time. By increasing or decreasing the mean velocity of the flow, the limit RMS velocity for which Model 1 is valid is displaced respectively to higher or lower RMS velocity values.

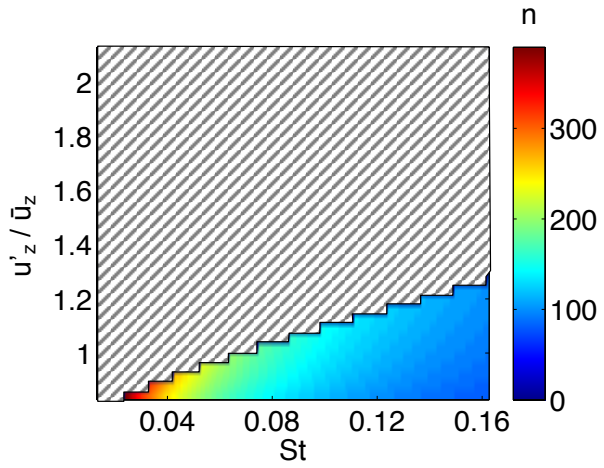

Figure 2.17: *Number of applied pulses on air particles as a function of Strouhal number and relative velocity modulation level following Model 1 from Figure 2.16. The hatched area corresponds to conditions for which Model 1 is not valid. The mean velocity of the flow is $1.42\,m.s^{-1}$.*

By now considering an air particle initially located at the upper boundary of the inter-electrode area ($z = h$), the maximum residence time, $t_{\mathrm{R,max}}$, will be attained if the air particle follows the red trajectory in Figure 2.18 (Model 2). In this case, the maximum residence time is found by solving the system of equations:

$$\int_{t_1}^{t_1+t_{\mathrm{R,max}}} \bar{u}_z^r \, dt = 0 \tag{2.26}$$

$$\int_{t_1}^{t_2} \bar{u}_z^r \, dt = -h \tag{2.27}$$

$$u_z(t_2) = 0 \tag{2.28}$$

$$\frac{du_z}{dt}(t_2) > 0 \tag{2.29}$$

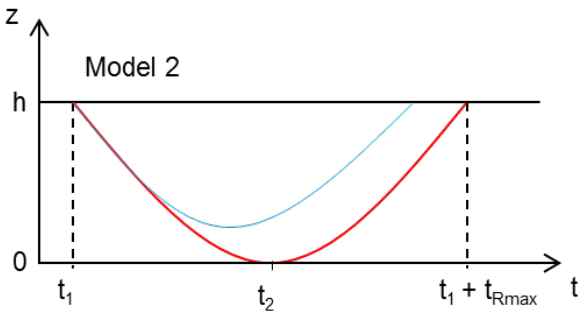

Figure 2.18: *Non-ideal (blue) and ideal (red) air particle trajectories maximising the residence time of an air particle in the inter-electrode area, when it is initially located at $z = h$, for acoustic oscillation amplitudes larger than the mean velocity.*

Figure 2.19 presents the effect of relative oscillation amplitude and Strouhal number on the number of applied pulses on a particle initially located at $z = h$ with a mean air velocity of $1.42\,\mathrm{m.s^{-1}}$. The hatched area indicates conditions for which Model 2 cannot be applied, *i.e.* the red trajectory in Figure 2.18 cannot be obtained (the trajectory then corresponds to the blue curve of this same figure). A given number of pulses at low Strouhal number (for example, 120 pulses in cyan) follows the same trend as the S-C transition in Figure 2.9. Changing the mean velocity of the air flow leads to the same displacement of the limit RMS velocity for which Model 2 is valid as in Figure 2.17.

The whole effect of acoustic forcing on the maximum residence time is finally considered by combining the results for low oscillation amplitudes (Model 0) and for the case with backflow (Model 1 and Model 2). Table 2.4 summarizes the different situations and the maximum residence times that an air particle can be exposed to, depending on the amplitude and the frequency of the forcing. Figure 2.20 shows isolines for a number of 90 pulses (residence time of 3 ms), obtained from a combination of the individual models (solid black lines). This value of 90 pulses provides the best fit with the experimental values (red squares) for the C-S and the S-C transitions. The qualitative structure in

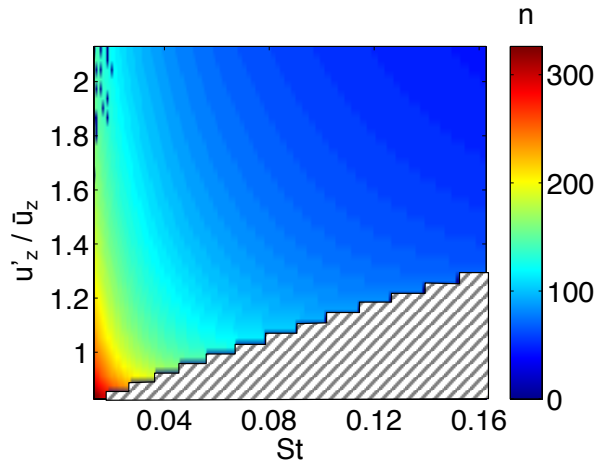

Figure 2.19: *Number of applied pulses on air particles as a function of Strouhal number and relative velocity modulation level following Model 1 from Figure 2.18. The hatched area corresponds to conditions for which Model 2 is not valid. The mean velocity of the flow is 1.42 m.s^{-1}.*

the frequency-amplitude domain looks very similar to the measured transition curves in Figure 2.9. It can therefore be concluded that the dominant effect of acoustic oscillations on the C-S and S-C transitions is merely linked to a change in the residence time of the air in the inter-electrode area.

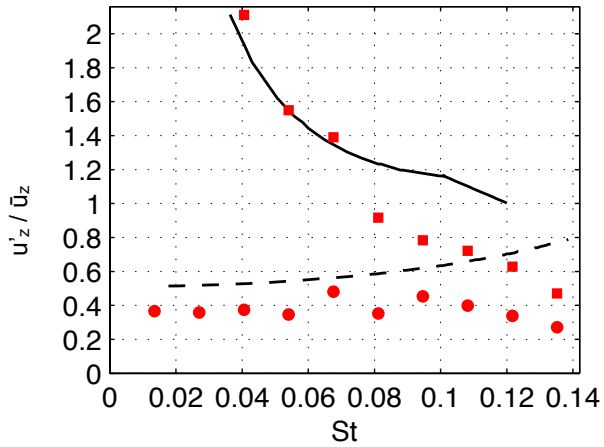

Figure 2.20: *Isolines corresponding to a number of 90 pulses applied to the air particles, obtained by combining modeling results (black lines) for low-amplitude (Model 0, dashed black line) and for high-amplitude forcing (Model 1 and Model 2, solid black line), for a mean velocity of the flow $\bar{u}_z = 1.42\,m.s^{-1}$. Data are compared to measurements (red squares) for a PRF of 30 kHz, voltage pulse amplitude of 12.75 kV and a mean air velocity of 1.42 m.s^{-1}. Number of pulses larger than 90 are found to the left of the lines.*

Table 2.4: *Synthesis of configurations maximizing the residence time.*

Amplitude of the acoustic forcing	f_{ac}	Model number	Maximum residence time, $t_{R,max}$	Trajectory of air particles in the inter-electrode area with maximum residence time
low: $u'_z\sqrt{2} \leq \bar{u}_z$	low	0	$t_{R,max} = \frac{h}{\bar{u}_z} + \frac{u'_z}{\bar{u}_z} \times \frac{T}{\pi\sqrt{2}} \times \sin\left(\frac{\pi}{T} t_{R,max}\right)$	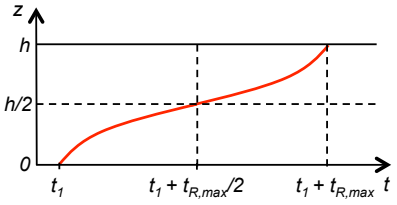
high: $u'_z\sqrt{2} > \bar{u}_z$	high	1	$\int_{t_1}^{t_1+t_{R,max}} u_z(t)dt = h$ $\int_{t_1}^{t_2} u_z(t)dt = 0$ $u_z(t_2) = 0$ $\frac{du_z}{dt}(t_2) > 0$	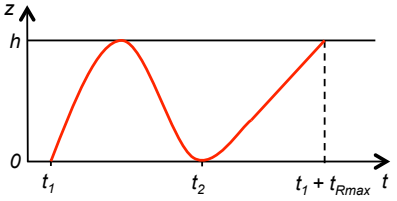
	low	2	$\int_{t_1}^{t_1+t_{R,max}} u_z(t)dt = 0$ $\int_{t_1}^{t_2} u_z(t)dt = -h$ $u_z(t_2) = 0$ $\frac{du_z}{dt}(t_2) > 0$	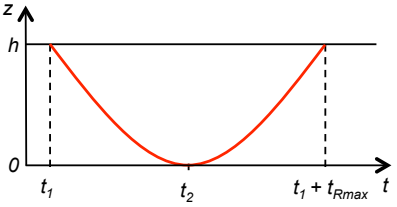

2.5 Conclusion

The effect of steady and harmonically oscillating flow on the regime transitions of NRP discharges has been experimentally investigated in a pin-annular configuration. The importance of the axial air velocity on the C-S and S-C regime transition voltages has been demonstrated. The azimuthal velocity component was found to have a negligible effect on the regime transitions, for the investigated range of velocities. These experimental observations can be explained by analysing the cumulative effect of repetitive nanosecond discharges and the residence time of air particles in the inter-electrode area.

In addition, the effect of harmonic oscillations superimposed to the mean steady flow was investigated. For a frequency range from 16 to 192 Hz, a moderate oscillation amplitude can promote the NRP spark regime. Higher oscillation amplitudes, on the other hand, promote the NRP corona regime. The oscillation amplitude at which spark-to-corona transition occurs is strongly frequency dependent. The dependence of the regime transitions on the oscillation amplitude

and frequency is explained by their effect on the residence time of air particles in the inter-electrode area. A model for the maximum residence time under the effect of acoustic oscillations was developed and qualitatively captured the experimentally-observed regime transitions in the frequency-amplitude space.

Chapter 3

Effect of laminar premixed flames on NRP corona discharges

The influence of laminar premixed flames on the behaviour of NRP corona discharges is studied in this chapter. In the first experimental configuration considered, NRP corona discharges are applied with an orientation parallel to the flame front, inducing a motion of the flame towards the electrodes. The visual aspect of the plasma discharges is shown to be a function of the flame's proximity to the electrodes. When the flame is sufficiently close to them, a NRP corona to spark regime transition is observed. The second section considers NRP discharges applied in several inter-electrode environments: in an air flow, in an air and methane flow, and in an air and methane flow with a flame between the electrodes. Along with the influence of the flame's proximity on the NRP discharges, similar to the effect observed in the first section, an also significant effect of the inter-electrode gas mixture on the NRP discharges is observed. This work has been performed in the Institut für Strömungsmechanik und Technische Akustik (ISTA) of the Technische Universität Berlin (TUB), Germany, and in the Clean Combustion Research Center (CCRC) of the King Abdullah University of Science and Technology (KAUST), Saudi Arabia.

3.1 Introduction

The influence of a flame on NRP discharges is a topic rarely addressed in the literature. Yet, several effects related to a reactive mixture can affect the NRP discharges. First, a flame induces an increase in temperature, thus a decrease in the gas density, which in turn leads to an increase in the reduced electric field close to the flame. This parameter has been established as significant regarding the NRP discharge regime (see for instance Pai et al. 2010b) by its influence on the electron temperature, as explained by Nighan (1970).

Second, the flame itself is also a plasma, constituted of ions, electrons, and excited species. For a lean premixed methane-air flame ($\Phi = 0.5$), the density of positive ions has been measured as in the order of $10^{10}\,\mathrm{cm}^{-3}$, by Wortberg (1965) with a Langmuir probe and by Alquaity et al. (2017) by Molecular Beam Mass Spectrometry (MBMS). The paper of Fialkov (1997) provides a literature review on the electric properties of flames (such as ionisation rates, densities of anions, cations and electrons) for different types of flames. This study mentions, for a laminar premixed methane-oxygen flame, the density of positive ions to be of the order of $10^{10}\,\mathrm{cm}^{-3}$ while the electron density ranges from 10^{9} to $10^{10}\,\mathrm{cm}^{-3}$. Detailed chemistry of positive and negative ions in atmospheric methane-oxygen flames is provided by Goodings et al. (1979a); Goodings et al. (1979b). The evolution of the prominent ionic species as a function of the considered position compared to the flame front are presented. CHO^+ and O_2^-, are the dominant ionised species upstream of the flame; they are formed by chemi-ionisation and electron attachment. Downstream of the flame, H_3O^+ becomes the dominant ion.

Finally, the composition of the reactive gas mixture flowing between the electrodes also has an influence on the NRP discharges. Indeed, the cross-sections of the gases define the collisions of electrons with atoms and molecules and are the fundamental parameters governing the Electron Energy Distribution Function (EEDF) and energy branching in the discharge process, as well as the rate constants of the reactions, as mentioned in Starikovskaia (2014).

This chapter displays the effect of a laminar lean premixed methane-air flame on NRP plasma discharges in the corona regime. Two different configurations are used: in the first one, NRP corona discharges are pulsed in a parallel direction compared to a flat flame, stabilised with an acoustic forcing. In the second setup, the two electrodes are located respectively upstream and downstream of a stagnation flame, allowing for generation of NRP corona discharges perpendicular to the flame front. These two configurations have been chosen because they represent a simplified model of the two extreme cases of the generation of NRP discharges in the presence of a flame front. In the first setup, the flame

and the electrodes are parallel while, for the second setup, they are orthogonal. In addition, the second setup is designed in order to provide an axisymmetric configuration, thus allowing for a more feasible comparison with numerical simulations.

3.2 NRP discharges parallel to flame front

3.2.1 Experimental setup

The burner is displayed in Figure 3.1(a). A methane-air mixture at atmospheric pressure and ambient temperature is set at an equivalence ratio of 0.75 with two rotameters (DK800, Krohne). The mixture is brought inside the plenum of the burner where it flows successively through a perforated plate, a honeycomb, and a converging nozzle. These elements are designed to ensure reduction of boundary layer thickness and a quasi-uniform velocity profile of the laminar flow at the nozzle outlet. A conical quartz tube of 150 mm total length confines the mixture at the outlet of the nozzle; this tube has an inner diameter of 20 mm at its inlet (at the nozzle of the burner), and 40 mm at its outlet; the low angle of opening of the conical tube (3.2 °) prevents detachment of the boundary layer. The flow rate of fresh gas is set so as to obtain a velocity of $23.5\,\mathrm{cm.s^{-1}}$ just above the holes for the electrodes (pierced 93 mm above the inlet section), where the diameter of the tube is 32.4 mm. This value of fresh gas velocity corresponds to the laminar burning velocity of the flame at an equivalence ratio of 0.75. The Reynolds number resulting from these settings, determined with Equation (2.5), is 480.

Visualisation of the flame is performed with a single-lens reflex digital camera (D70s, Nikon) featuring an exposure time of 2 s, equipped with a visible-range lens of 50 mm focal length (Nikon). The spatial resolution of the pictures is 62.5 μm per pixel.

NRP plasma discharges are generated between two pin electrodes set in the tube. These 1-mm diameter electrodes are both made of tungsten and have a radius of curvature of 200 μm; one of them is linked to the high-voltage of a nanosecond pulse generator (FPG-series, FID Technologies) while the other electrode is connected to the ground. The gap distance between the electrodes is 8 mm. This setup allows application of 10 ns-duration pulses, with amplitudes up to 11 kV, at a Pulse Repetition Frequency (PRF) of 30 kHz. A voltage probe (PHV 4002, PMK GmbH), and a current probe (Current Monitor Model 6585, Pearson Electronics) linked to an attenuator (2-20, Barth Electronics) are used to evaluate the energy deposited by the NRP discharges in the inter-

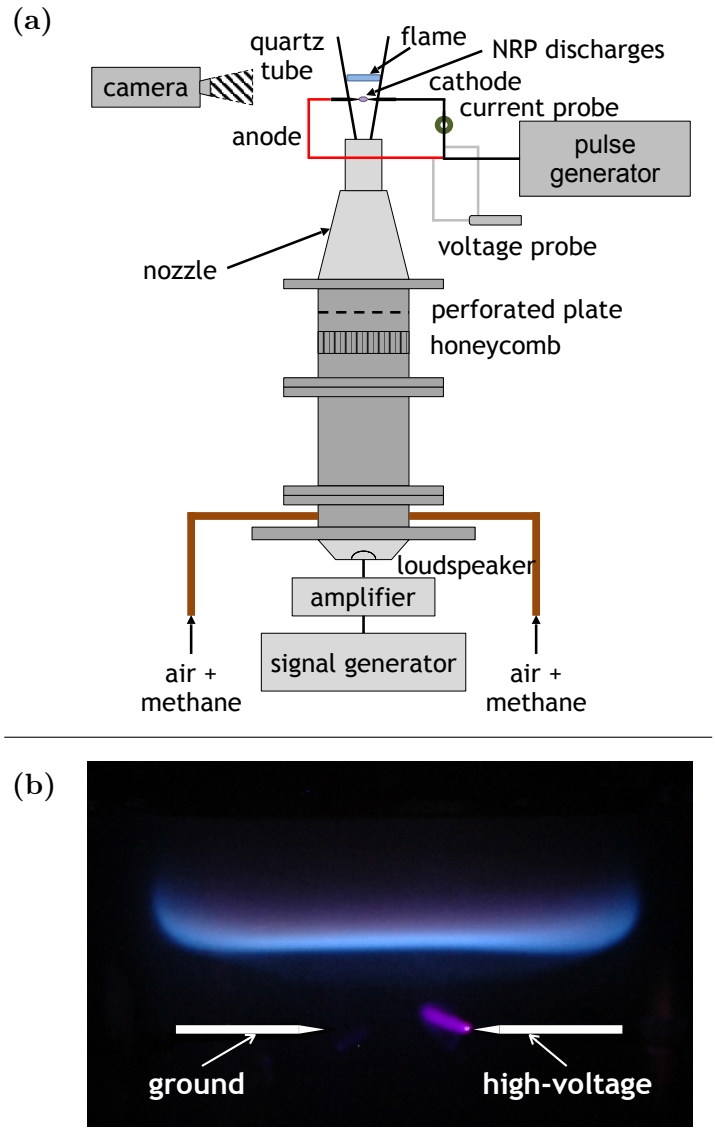

Figure 3.1: *(a) Experimental setup and (b) photograph of the flame (blue) and of the NRP corona discharges (violet); the exposure time is 2 s.*

electrode area. The voltage and current probes are connected to an oscilloscope (DSOX3024A, Agilent) for recording of the acquired signals. To match the impedances of each electrical circuit, the voltage probe is connected to the 1 MΩ impedance input of the oscilloscope and the current probe to the 50 Ω impedance input. The deposited energy per pulse for each experimental measurement has been determined in the manner presented in Appendix A. During these experiments, the NRP plasma discharges are in the NRP corona regime, as defined by Pai et al. (2009). The flame and NRP corona discharges are visualised on Figure 3.1(b). Since the exposure time of the camera is set to 2 s

and the discharges are pulsed at a PRF of 30 kHz, the photograph corresponds to a visualisation of 60,000 applied pulses. Figure 3.2 shows photographs of the NRP discharges for various applied voltages ranging from 4.7 to 10.7 kV in a transverse air flow. Figures 3.3 and 3.4 present the corresponding waveforms of the discharges: the voltage amplitude, U, the conduction current, I_{cond}, the instantaneous power, P, and the deposited energy per pulse, E_{p}. The PRF is set to 30 kHz, the inter-electrode gap distance is 8 mm and the air flow velocity is 23.5 cm.s^{-1}. A schematic of the electrodes has been superimposed in white on the images of Figure 3.2. Pictures (a), (b) and (c) show discharges in the NRP corona regime while picture (d) shows discharges in the NRP spark regime. This regime is not used in the following part of this section, as it has a too strong effect on the flame's behaviour. Considering the electrode configuration, the electromagnetic field generated by the NRP discharges is oriented in a direction parallel to the flame front.

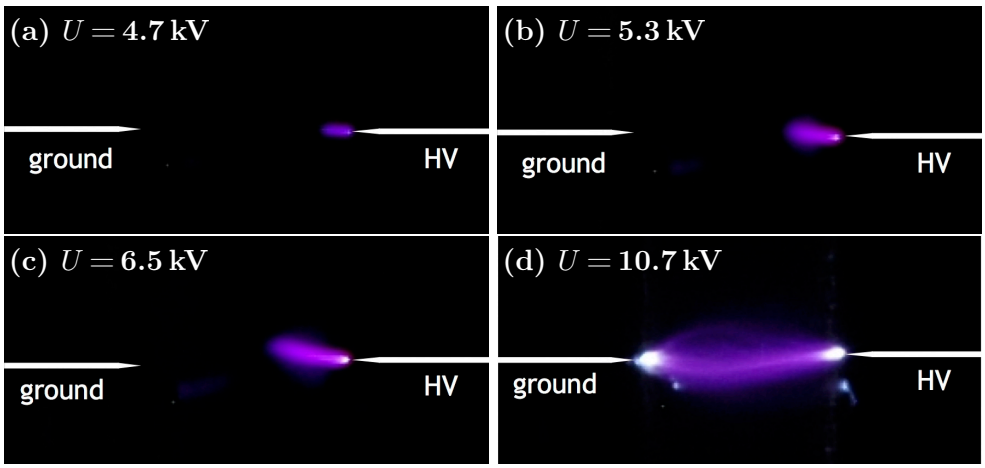

Figure 3.2: *NRP discharges in air. The high-voltage electrode (anode) is on the right, the ground is on the left. The gap distance between the electrodes is 8 mm, the PRF is 30 kHz and the velocity of the transverse air flow is 23.5 cm.s^{-1}. (a), (b) and (c) are in the NRP corona regime while (d) is in the NRP spark regime. The voltage and current waveforms corresponding to these photographs are given in Figure 3.3 while the power and energy waveforms are displayed in Figure 3.4.*

The values of conduction current and voltage increase from 1 to 3 A and from 5 to 7 kV for the NRP corona discharges (frames (a), (b) and (c) from Figure 3.2) while they reach up to 7 A and 11 kV for discharges in the NRP spark regime (frame (d) from Figure 3.2). The corresponding energies range from 50 to 200 μJ.pulse^{-1} in NRP corona discharges up to 700 μJ.pulse^{-1} in NRP spark discharges.

The bottom part of the burner is equipped with a loudspeaker (Monacor SPH-115, 80 W power), linked to an amplifier and signal generator. These elements

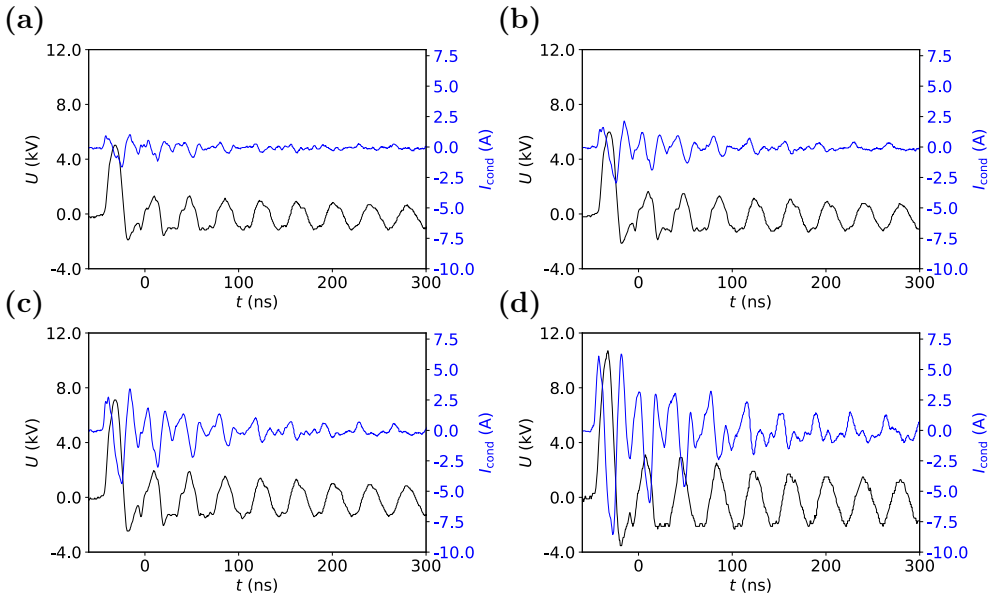

Figure 3.3: *Temporal evolution of the voltage amplitude, U (black line), and conduction current, I_{cond} (blue line), corresponding to the discharges presented in Figure 3.2.*

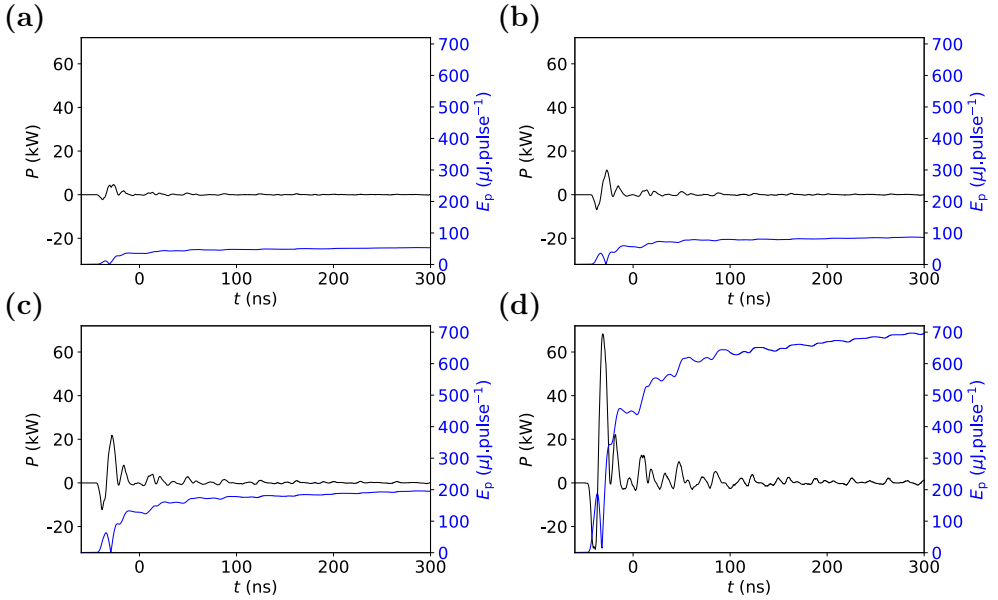

Figure 3.4: *Temporal evolution of the instantaneous power, P (black line), and deposited energy, E_{p} (blue line), corresponding to the discharges presented in Figure 3.2.*

are used to generate harmonic acoustic waves at controlled amplitudes and frequencies. Without acoustic modulation of the flow, it was not possible to obtain a flat flame, due to the Darrieus-Landau instability. However, it has been shown that an acoustic forcing of the flow allows for the restabilisation of a planar flame under certain conditions of frequency and amplitude. Fig-

ure 3.5 from Clanet and Searby (1998) displays the stability domain of a laminar lean premixed propane-air flame: at given conditions of frequency and forcing amplitude, the Darrieus-Landau instability can be suppressed. Another instability, named parametric instability, appears for high amplitudes of the forcing. Wangher et al. (2008) make use of such a stabilisation process to investigate flames with experimental parameters similar to those of this study. Therefore, in order to obtain a stable flat flame, an acoustic forcing with an amplitude of 1.7 times the flow velocity has been applied at 250 Hz.

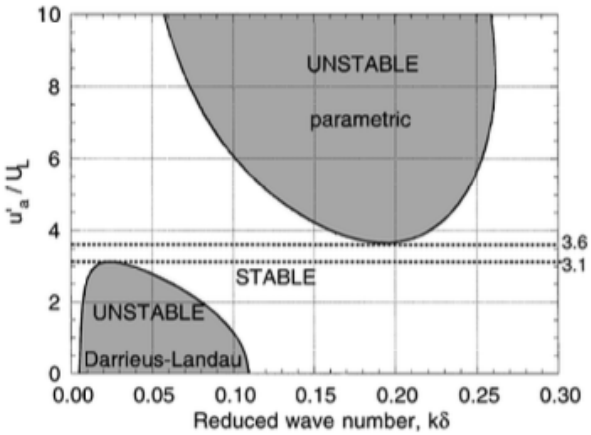

Figure 3.5: *Stability domains of a laminar planar lean propane-air flame, from Clanet and Searby (1998).*

Figure 3.6 shows a comparison in the shape of the flame when acoustic forcing is applied transversally to the flame front. The acoustic forcing frequency, f_{ac} is maintained constant at 250 Hz, and the forcing amplitude is increased from 0 to 2. A forcing amplitude of $u'_z/\bar{u}_z = 1.7$ allows to obtain a reasonably flat flame and is used in the following part of the study.

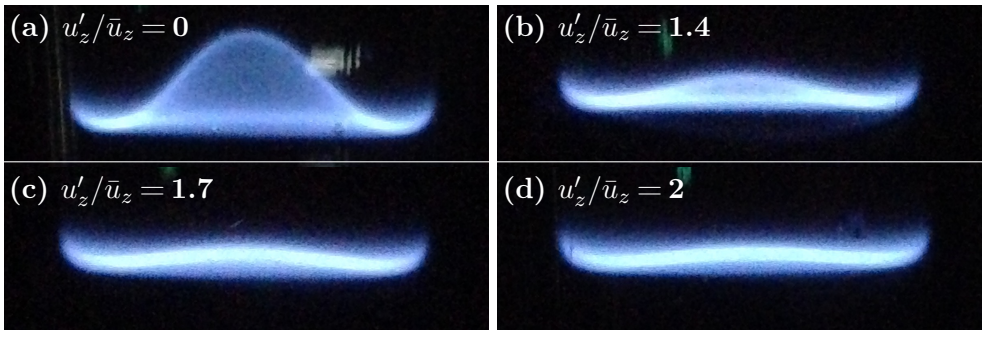

Figure 3.6: *Stabilisation of the laminar premixed flame with an acoustic forcing of $f_{ac} = 250$ Hz. (a) Flame with the Darrieus-Landau instability. (b), (c) and (d) for increasing relative velocity amplitude, $u'_z/\bar{u}_z$.*

3.2.2 Experimental procedure

This part of the study aims to display the fact that the flame and its proximity to the electrodes impacts the shape of the plasma discharges. This influence on the NRP corona discharges is assessed by visually comparing the discharges while varying the distance between electrodes and flame, z. This is realised by slightly changing the global flow rate of the methane-air mixture. Since the quartz tube has a conical shape, the velocity of the fresh gas evolves with the considered axial position. The stabilisation position of the flame corresponds to the axial position where the velocity of the fresh gas mixture is equal to the flame's propagation velocity. For three different distances, the shape and luminous intensity of the NRP plasma discharges are observed and analysed.

3.2.3 Results and discussion

Figure 3.7 compares the shape of the NRP plasma discharges for three different distances between electrodes and flame, z. The voltage amplitude is kept constant at $U = 5.4\,\mathrm{kV}$ and the PRF is 30 kHz.

In all pictures of Figure 3.7, the discharges are in the NRP corona regime. The distance between electrodes and flame is $z = 2.86\,\mathrm{mm}$ in frame (a); there is only a visible light emission at the anode. The NRP corona discharges are oriented in the horizontal direction, from the anode in the direction of the cathode. However, when the distance z is reduced to 2.63 mm, the NRP discharges deviate towards the flame, resulting into a longer, bended corona, with a horizontal part close to the high-voltage electrode and a vertical part—directed towards the flame front. When the distance between electrodes and flame is further decreased to 2.53 mm, the discharges deviate further in the vertical direction, towards the flame front, becoming nearly vertical. Some violet light is visible at the ground electrode of frame (c); it is in fact the reflection from the discharge at the high-voltage electrode on the quartz tube. An increase in the propagation velocity of the NRP discharges due to a local increase in the reduced electric field could be responsible for their increased length.

Pai et al. (2010b) studied the conditions of transition between NRP corona, glow and spark discharges in air for several parameters, such as pulse repetition frequency, voltage amplitude, inter-electrode gap distance and ambient gas temperature. A rather significant influence of the ambient gas temperature on the regimes of NRP discharges was highlighted. An explanation for this strong dependence on ambient gas temperature is the fact that an increase of

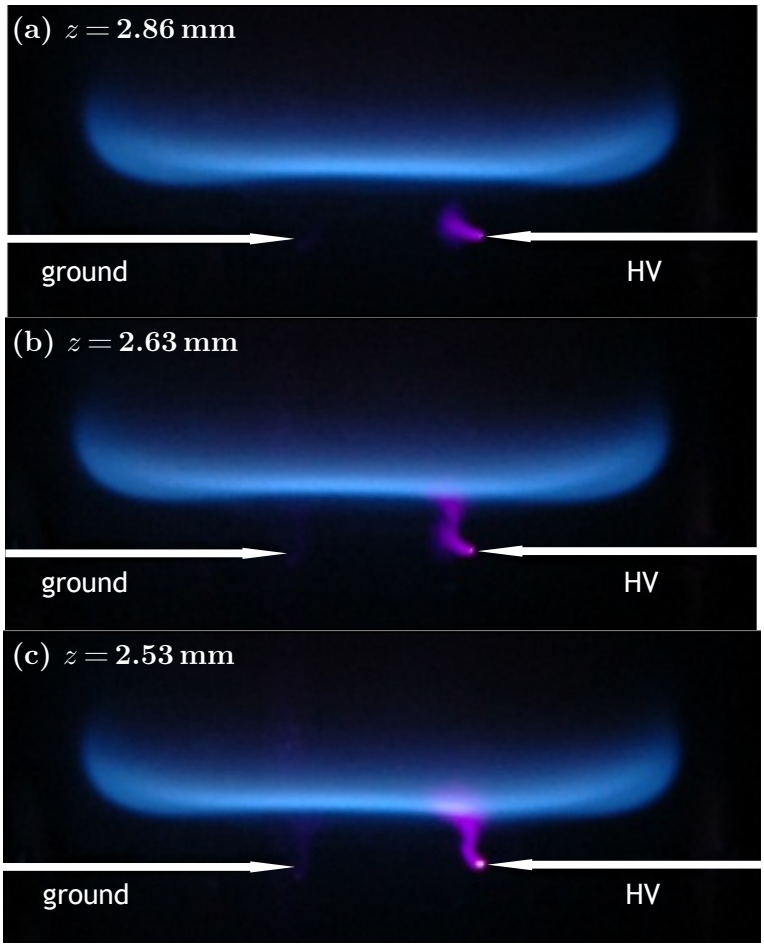

Figure 3.7: *Influence of the flame-to-electrodes distance, z, on the shape of NRP plasma discharges. The amplitude of the plasma discharges is constant: $U = 5.4\,kV$ and the PRF is $30\,kHz$. The equivalence ratio of the methane-air flame is $\Phi = 0.75$.*

temperature leads to a lower density of particles in the gas, thus to a higher value of reduced electric field, a parameter defined in Equation (1.1) and which favours the transition from corona to glow discharges and from glow to spark discharges. In the present study, radiative heating from the flame is a possible explanation for the observed change in the shape of the discharges. A fact that confirms this observation is that, when the flame was brought even closer to the electrodes, the discharges transited to the spark regime. This phenomenon has not been photographed since this transition to spark discharges led to a flashback of the flame.

In addition to the change in density, methane-air flames are known to have a relatively high density of charged particles (of the order of $10^{10}\,\mathrm{ions.cm^{-3}}$, see Wortberg 1965; Goodings et al. 1977; Fialkov 1997); this will also affect

the shape of the discharges as well as the discharge regime.

3.3 NRP discharges perpendicular to flame front

3.3.1 Experimental setup

The setup used in this section, a co-flow burner equipped with a stagnation plate, is displayed in Figure 3.8. Methane, air and nitrogen are brought to three flowmeters (respectively 2,000 sccm, 10,000 sccm and 10,000 sccm Mass-Flo Controller, MKS Instruments) regulated by a controller (Type 247D, MKS Instruments) in order to set the flows of methane and air at an equivalence ratio of 0.8. Methane and air are then premixed upstream of the burner and flow through a plenum and converging nozzle before exhausting at the nozzle outlet, which has an outer diameter of 10 mm. At the nozzle's outlet, the velocity of this methane-air mixture is 1.2 $m.s^{-1}$ which corresponds to 4.5 times the laminar flame speed (26.7 $cm.s^{-1}$) at this condition. Considering this velocity of 1.2 $m.s^{-1}$ and this diameter of 10 mm, the Reynolds number, defined in Equation (2.5), has a value of 780. Above the nozzle is a stainless steel, water-cooled stagnation plate, maintained at a constant temperature of 20 °C. Upon ignition of the methane-air flow, the flame under the plate is flat, but its edge is attached to the nozzle of the burner. An annular co-flow of nitrogen is blown from the annular section surrounding the central nozzle in order to detach the flame from the nozzle of the burner. A study by Johnson et al. (2015) demonstrated that, for the same separation distance than the one used in this study, the contribution of radial terms in the equations for energy and momentum conservation was negligible for nozzle diameters larger than 12 mm. Setting the co-flow of nitrogen at a velocity equal to the velocity of the central ignitable mixture of methane and air allows to virtually increase the hydraulic diameter of the nozzle.

In order to isolate the burner electrically, the converging nozzle and the annular part were made out of plastic material (PEEK). Two tungsten pin electrodes are inserted in the setup in order to apply NRP discharges: one has a diameter of 0.1 mm and is placed upstream of the flame, inside the nozzle, while the other electrode is set in the centre of the plate and has a diameter of 1 mm. The inter-electrode gap distance is 12 mm. The upstream electrode is linked, through a stainless steel perforated plate, to the high-voltage of a nanosecond pulse generator (FPG Series, FID Technologies) while the downstream electrode is grounded (thus actually grounding the whole stagnation plate). A current probe (model 6585, Pearson Electronics) is used to monitor the current while the voltage is measured with a probe (P6015A, Tektronix) connected between

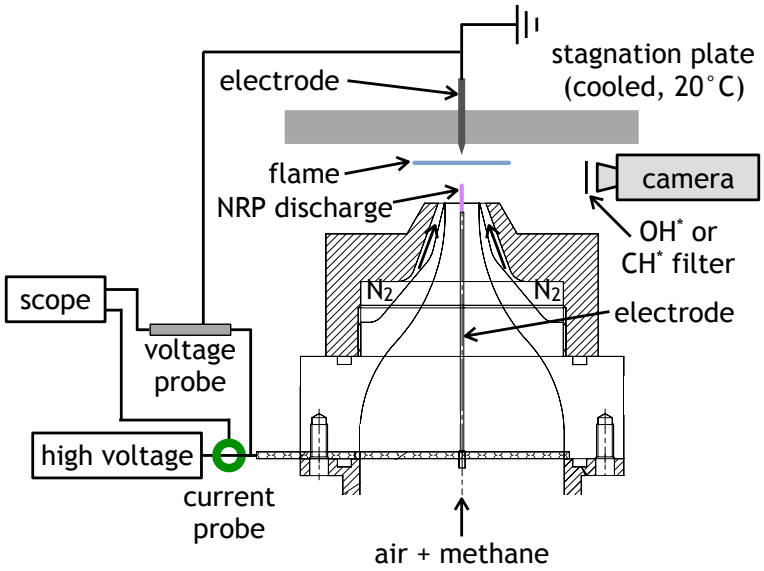

Figure 3.8: *Experimental setup used for the study of the effect of NRP discharges on a laminar premixed flame. The flame is stabilised upstream of a cooled stagnation plate and the discharges are pulsed perpendicularly to the flame front.*

high-voltage and ground. Both probe signals are acquired with an oscilloscope (Infiniium DSO9254A, Agilent Technologies) with a $2\,\mathrm{GSa.s^{-1}}$ sampling rate; the voltage probe is linked to the $1\,\mathrm{M\Omega}$ impedance input and the current probe to the $50\,\Omega$ impedance input. A low-voltage attenuator (Model 2-20, Barth Electronics) is attached between the current probe and the oscilloscope. Considering the transverse orientation of the electrodes compared to the flame front, the electromagnetic field generated by the NRP discharges is, in this configuration, mainly perpendicular to the flame front.

The area between the nozzle and the stagnation plate is visualised through an Intensified Charge-Coupled Device (ICCD) camera (PI-Max:1K.GenII, Princeton Instruments) equipped with a UV lens (105 mm f/4.5 250-650 nm, Jensoptik). A filter, either for CH^* (FB430-bandpass 430 ± 5 nm, Thorlabs) or for OH^* (XHQA310, Asahi Spectra) is mounted on the UV lens in order to acquire the luminous emission of the corresponding excited species.

The FID generator and the ICCD camera are synchronised with the help of a delay/pulse generator (Model 575, BNC), which is not shown in Figure 3.8. A pulsed trigger signal of width 100 ns and amplitude 5 V is sent to the FID generator while a TTL signal of $10\,\mu$s width is used to trigger the ICCD camera. Several parameters, such as the Pulse Repetition Frequency (PRF) of the NRP discharges, the gate width, the gate delay, and the number of gates per exposure of the ICCD camera are modified according to the needs of the study.

A CH* chemiluminescence image of the flame is presented in Figure 3.9. The ICCD camera has the following settings: a gate width of 98 μs and a number of gates per exposure of 400. The electrodes (HV and ground), as well as the stagnation plate and the nozzle of the burner, are displayed on the picture. The separation distance between the nozzle and the plate is 7.2 mm.

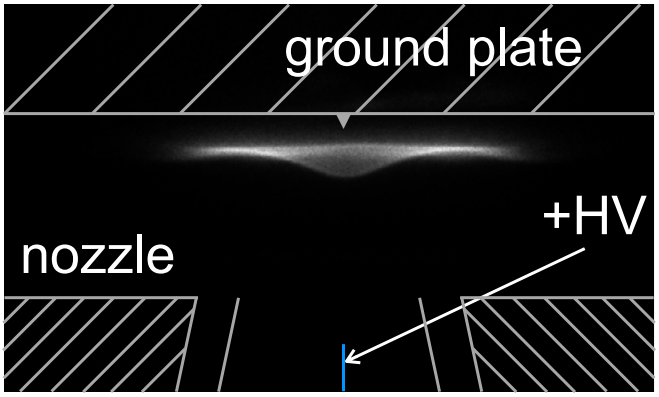

Figure 3.9: *Acquisition of the flame's CH* emission, acquired with the ICCD camera. The gate width of the camera is 98 μs and the number of gates per exposure is 400. The burner's elements are added in grey for visualisation. The distance between nozzle and plate is 7.2 mm, the nozzle's inner and outer diameters are 10 mm and 14 mm.*

Due to the high velocity of the unburnt gas compared to the laminar flame speed (4.5 times the laminar flame speed), the flame is rather close to the stagnation plate. The presence of the upstream electrode manifests itself through a velocity deficit causing a small bump in the centre of the flame. This velocity decrease in the centre of the flame is evaluated through numerical simulations in Appendix D, it corresponds to about 70 % of the mean axial velocity at the outlet of the burner.

Figure 3.10 is a comparison of the CH* and OH* emission of the flame. The two images look similar, yet the CH* emission of the flame (b) is slightly blurrier than the OH* emission (a), despite the fact that the camera's focus has been adjusted before both measurements. Because of the higher sharpness and more intense signal that the OH* emission provides, only the acquisitions of this species are presented in the coming work. The OH* emission is located approximately 400 μm downstream compared to the CH* emission profile, which also corresponds to the calculated shift between the maximum OH and CH concentrations in the reaction front (see Appendix D). Despite this difference of location in the two species emission, the measured flame displacement under application of NRP discharges, as well as the plasma light emission, remain the same whether they are determined with the OH* or the CH* emission.

Simultaneously to the ICCD camera acquisitions, the current and voltage of

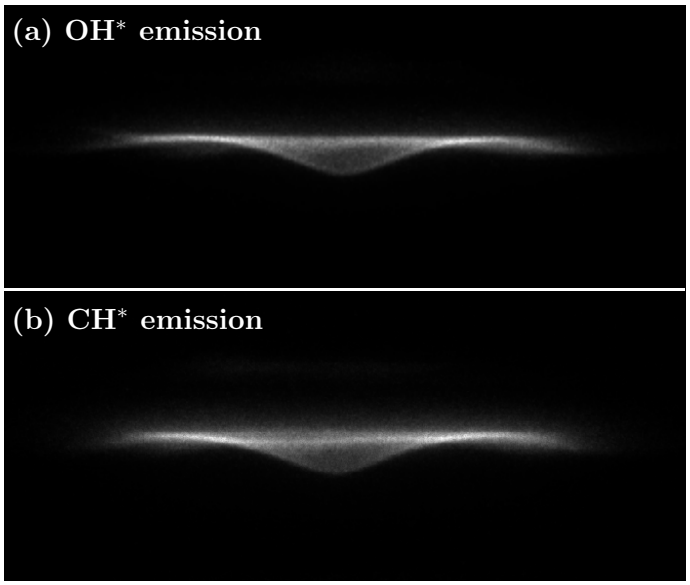

Figure 3.10: *Acquisition of the flame's luminous intensity: (a) is acquired with an OH* filter on the lens of the camera and 3 gates per exposure while (b) is acquired with a CH* filter on the lens of the camera and 25 gates per exposure. Both frames have been acquired with a gate width of 1 ms.*

the NRP discharges are measured. These two quantities allow to determine the instantaneous power and energy of the NRP discharges in the corona regime. Typical results of electrical measurements are given in Figure 3.11 where the PRF is 28 kHz and a 1,000 pulses were averaged. Figures 3.11(a) and (b) present the temporal evolution of voltage amplitude, U, (left, black line), total current, I (left, blue line), instantaneous power, P (right, black line) and deposited energy per pulse, E_p (right, blue line) for NRP discharges in an axial air flow. Figures 3.11(c) and (d) present the same quantities for NRP discharges in an axial methane-air premixture without flame ($\Phi = 0.8$). Figures 3.11(e) and (f) present these profiles when a methane-air flame ($\Phi = 0.8$) is stabilised in the inter-electrode area. The power and energy per pulse have been deduced from the current and voltage profiles according to the procedure detailed in Appendix A.

The voltage signal looks similar for the three considered conditions. By increasing the gap distance, a voltage-current measurement, without any discharge, has been performed and the obtained current, capacitive due to the high resistivity of the air in the gap, is thus considered as the displacement current, I_disp. The conduction current, I_cond, is deduced by subtracting the displacement current, I_disp, from the total current, I. Comparing the conduction currents for the three inter-electrode conditions (air, air-methane and air-methane with flame) shows that the conduction current's temporal evolution is different for each considered

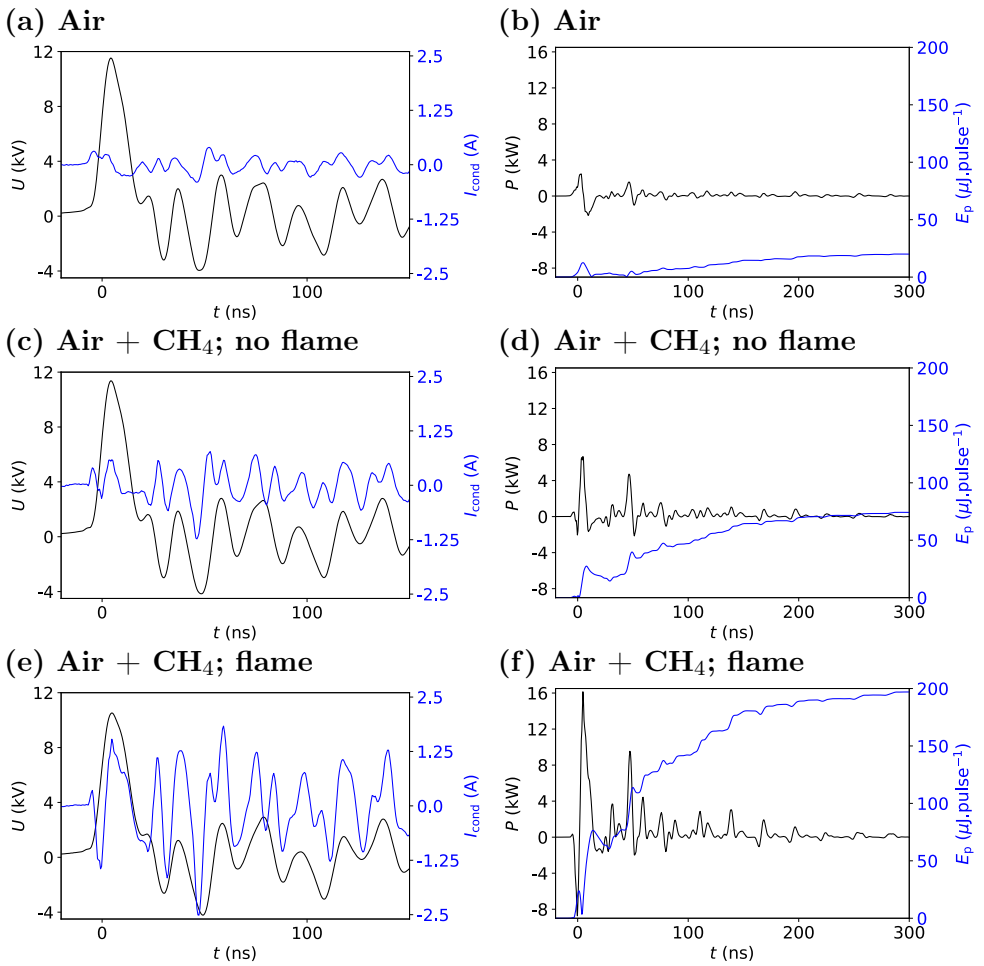

Figure 3.11: *Typical profiles of voltage, U (left, black line), and conduction current, I_{cond} (left, blue line), and power, P (right, black line), and energy per pulse, E_{p} (right, blue line), for NRP discharges, in (a) and (b) in a 318 $L.h^{-1}$ axial flow of air, in (c) and (d) in a methane-air flow ($\Phi = 0.8$) and in (e) and (f) close to a methane-air flame ($\Phi = 0.8$) at PRF = 28 kHz, averaged over 1,000 pulses.*

condition. In an air and in an air-methane flow, it has a value around 500 mA, while it increases to 1.3 A when a flame is stabilised in the inter-electrode area. This increase in conduction current accounts for the higher instantaneous power and the higher deposited energy: $P = 16$ kW and $E_{\text{p}} = 200\,\mu$J.pulse^{-1} in Figure 3.11(f), compared to $P = 6$ kW and $E_{\text{p}} = 70\,\mu$J.pulse^{-1} in Figure 3.11(d) and $P = 3$ kW and $E_{\text{p}} = 20\,\mu$J.pulse^{-1} in Figure 3.11(b). The measurements in the air flow and in the air-methane flow are all within the range of uncertainties of the energy measurements, estimated at 30 μJ.pulse^{-1}.

3.3.2 Experimental procedure

In order to visualise the NRP discharges, the camera equipped with the OH* filter is synchronised with the high-voltage pulse generator. The gate width of the camera is set to a value of 500 ns in order to acquire the light emission from the plasma alone. This setting is particularly important when a flame is present in the inter-electrode area: with a camera opening synchronised with the plasma discharges and a short exposure time, the OH* emission of the flame is small compared to the plasma light emission.

The image acquisition and energy measurements are realised for a range of PRF between 10 and 28 kHz and for the three different conditions considered in Figure 3.11: first, with an axial flow rate of 318 $\mathrm{L.h^{-1}}$ of air along with an annular co-flow of nitrogen. The second condition considers a similar air and nitrogen flow, where a flow rate of methane is added to the central flow of air, so that the mixture's equivalence ratio is 0.8. Finally, for the third condition, the methane-air mixture is ignited and an approximately planar stagnation flame is stabilised between the nozzle and the plate. With these air flow rates, the bulk velocity of the fresh gases at the outlet of the nozzle is kept constant at 1.2 $\mathrm{m.s^{-1}}$.

3.3.3 Results and discussion

As the voltage amplitude is kept constant, the energy deposited by the plasma discharges is varied by means of the PRF. Figure 3.12 displays the influence of the repetition frequency of the pulses on the measured electrical energy per pulse, E_p, for the three cases: with an axial air flow of 318 $\mathrm{L.h^{-1}}$ (blue circles), with an axial air and methane flow ($\Phi = 0.8$, green triangles) and with a laminar premixed flame ($\Phi = 0.8$, black squares) transverse to the electrodes.

The overall measured energy is lower than 200 μJ per pulse. The energy deposited in air is of the order of a few microjoules per pulse, close to the values of the literature for NRP discharges with these characteristics (see Pai et al. 2009). The energy deposited in the air-methane mixture seems to be slightly higher, though still within the range of uncertainties (30 $\mu\mathrm{J.pulse^{-1}}$) for PRFs lower than 15 kHz. The electrical energy is also higher when considering a case with a flame in the inter-electrode area, especially at PRF = 28 kHz, where the energy reaches 175 $\mu\mathrm{J.pulse^{-1}}$.

Images of the plasma discharges as a function of the PRF are displayed in Figure 3.13 for an axial air flow with a velocity of 1.2 $\mathrm{m.s^{-1}}$ in the inter-electrode

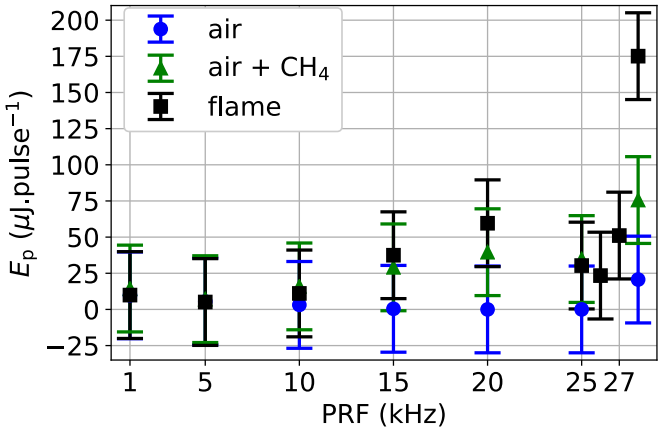

Figure 3.12: *Measured electrical energy of the NRP discharges as a function of the PRF for three different types of inter-electrode environment: with a 0.8-equivalence ratio methane-air flame (black squares), in an air and methane flow at equivalence ratio 0.8 (green triangles) and in an air flow (blue circles). The gas flows in the direction of the electrodes, with a velocity of 1.2 m.s^{-1}.*

area, in Figure 3.14 for an air and methane flow (equivalence ratio 0.8), and in Figure 3.15 when a laminar premixed flame is stabilised between the burner's nozzle and the stagnation plate. The nozzle and the stagnation plate have been added in grey lines to the photos.

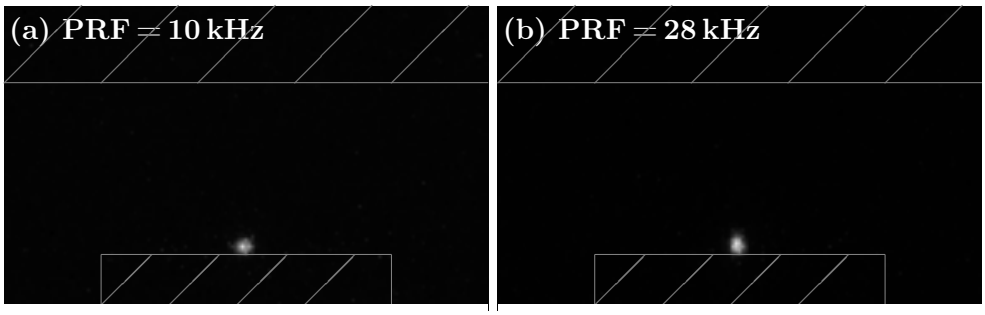

Figure 3.13: *Effect of PRF on the NRP corona discharges. Air flows from the nozzle (hatched lower part of each frame) to the stagnation plate (hatched upper part of each frame) with a flow rate of 318 L.h^{-1}, resulting in an axial velocity at the outlet of the nozzle of 1.2 m.s^{-1}. The voltage amplitude of the discharges is 12 kV, the ICCD camera is set at a gate width of 500 ns, the minimum gate delay of 26 ns and a number of gates per exposure of 1,800.*

The NRP discharges in Figure 3.13 are visible out of the burner's nozzle starting from 10 kHz but remain localised very close to the anode's tip. There is no visible change in their aspect between 10 and 28 kHz, and their energy varies only slightly, between 0 and 20 μJ.pulse^{-1}, remaining within the range of uncertainty.

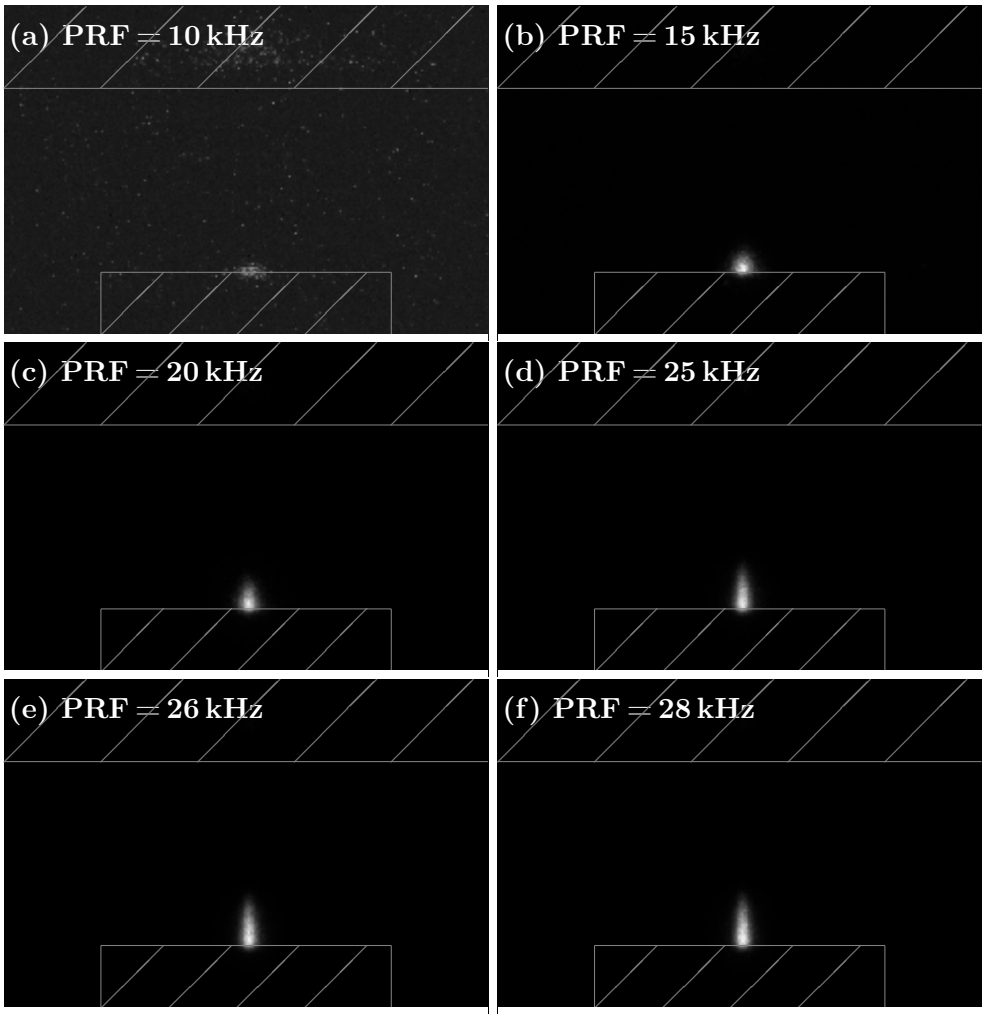

Figure 3.14: *Effect of PRF on the NRP corona discharges. A premix of air and methane ($\Phi = 0.8$) flows from the nozzle (hatched lower part of each frame) to the stagnation plate (hatched upper part of each frame) with a flow rate of 318 $L.h^{-1}$. The voltage amplitude of the discharges is 12 kV, the ICCD camera is set at a gate width of 500 ns, the minimum gate delay of 26 ns and a number of gates per exposure of 1,800.*

The discharges in an axial flow of air and methane (see Figure 3.14) are also visible from 10 kHz on, yet they are much longer and more luminous compared to the case in air alone (see Figure 3.13). This is in good agreement with the fact that the measured electrical energy in air and methane is slightly higher than in the case with air. This increased length of the NRP corona discharges in air and methane mixture is linked to an increase in the propagation velocity of the discharges.

The flame is visible in all the frames of Figure 3.15 because of the low intensity of

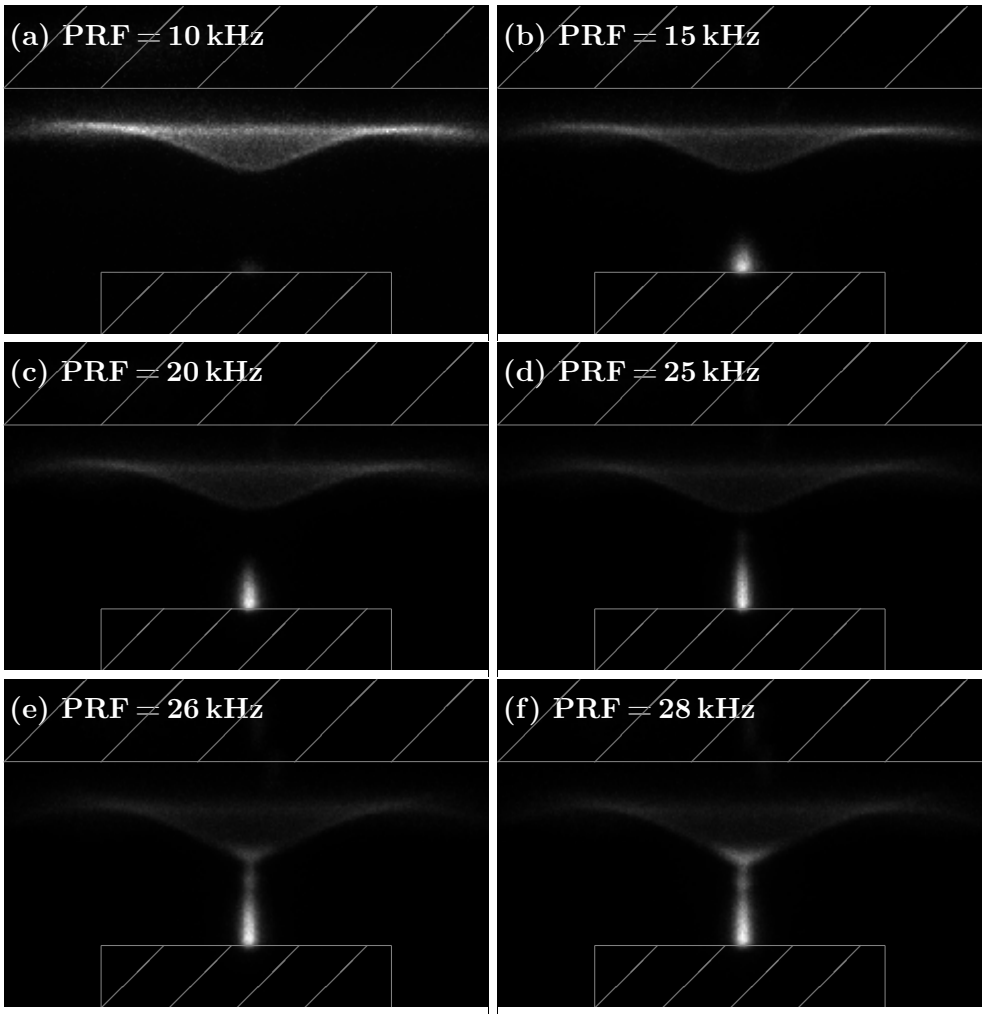

Figure 3.15: *Effect of PRF on the NRP corona discharges. A methane-air flame ($\Phi = 0.8$, visible in each frame) is stabilised between the nozzle (hatched lower part of each frame) and the stagnation plate (hatched upper part of each frame). The voltage amplitude of the discharges is 12 kV, the ICCD camera is set at a gate width of 500 ns, the minimum gate delay of 26 ns and a number of gates per exposure of 1,800.*

the NRP discharges, especially at PRFs smaller than 20 kHz. The discharges in the presence of a flame (see Figure 3.15) are similar to the ones in the methane-air mixture (see Figure 3.14) for PRFs below 20 kHz (frames (a) and (b)). For higher PRFs, the discharges are more elongated when a flame is stabilised in the inter-electrode area. For repetition frequencies between 26 and 28 kHz, the discharges stretch up to the flame front (frames (e) and (f)). For these two cases, the NRP corona discharge propagates into the flame front and does not go straight to the stagnation plate. This means that the energy of the plasma discharges is distributed inside the flame itself. This matter is further discussed

and interpreted in Section 3.3.3.

As shown in Figure 3.12, for PRFs higher than 15 kHz, the deposited energy per pulse is higher when a flame is stabilised in the inter-electrode area, compared to the energy in an air-methane or in an air flow. This correlates with the length of the plasma. Another interesting phenomenon is the visible influence of the fresh gas composition: the NRP discharges pulsed in an axial flow of air (see Figure 3.13) are barely visible and lead to deposited energies smaller than $30\,\mu\text{J.pulse}^{-1}$, corresponding to the limit for the measurements. When methane is added (see Figure 3.14), the deposited energy per pulse increases slightly, and this only for PRFs above 15 kHz. Despite this quasi-similar energy, the discharges are much longer.

The contours of the NRP discharges are determined with an edge detection method. This algorithm, developed by Canny (1986) and detailed in other works, such as Parker (2011), is based on the detection of contrast gradients in an image, the edges being detected by adjusting the lower and upper values for the thresholds of these gradients. Figure 3.16 presents an example of application of the edge detection method on the pictures from Figures 3.14 and 3.15. The upper and lower position of the NRP discharges are marked with red lines. In frames (a) and (b) which correspond to the case without ignited flame, considerable parasitic light emission is observed. In the case with flame (frames (c) and (d)), the flame is also detected above the NRP discharges, and frame (d) shows that the NRP discharges touch the flame front for this repetition frequency.

From the detected upper and lower positions of the plasma light emission, the length of the NRP corona discharges is determined by adding 4 mm of the measured distance between the two red lines, corresponding to the distance between the tip of the anode and the field of view of the camera. Figure 3.17 presents the evolution of this length, Δz_{pl}, as a function of the PRF of the pulses. The NRP corona discharges are detected when PRF > 10 kHz. For PRFs of 10 and 15 kHz, they are approximately of the same length for the case without flame and the case with flame. For PRFs of 20 kHz or higher, the NRP corona discharges in the presence of a flame are much longer than the discharges in cold gas mixture. The length of the NRP corona discharges, Δz_{pl}, is expressed as a function of the discharges's mean power, P_{p}, and displayed in Figure 3.18. When the electrical power of the discharges is smaller than 1 W, the length of the NRP corona discharges is the same whether or not there is a flame in the inter-electrode area. For higher power values, the length of the NRP corona discharges increases dramatically in the presence of a flame in the inter-electrode area. The experimental points where the discharges's length is 7.5 mm corresponds to the cases where the flame is touching the NRP

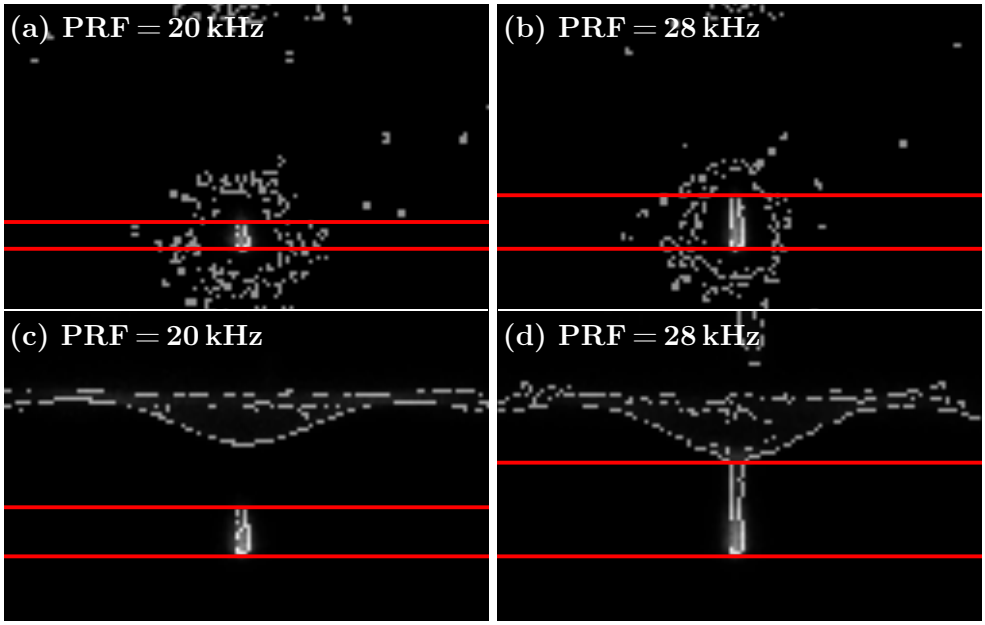

Figure 3.16: *Detected upper position and lower position of the NRP plasma discharges (red lines) in a methane-air mixture: (a) and (b) without flame and (c) and (d) with a flame (visible above the plasma discharges).*

discharges.

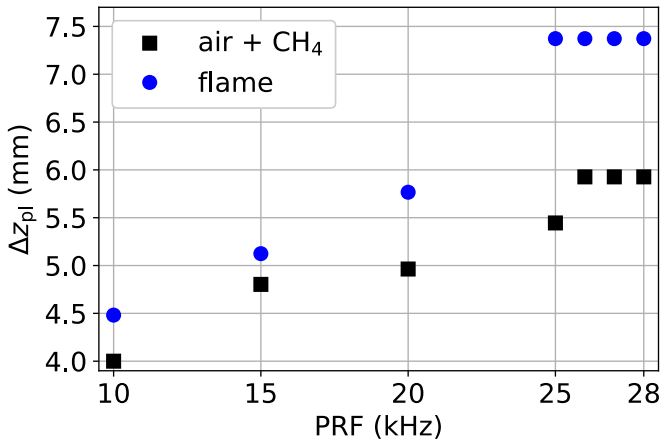

Figure 3.17: *Discharge length, Δz_{pl}, as a function of the PRF: for NRP discharges pulsed in a methane-air mixture with $\Phi = 0.8$ (black squares) and for the case when a methane-air flame is stabilised in the inter-electrode area (blue circles).*

As mentioned in Section 3.2.3, the shape of NRP discharges and their energy is a function of the reduced electric field, E/n, defined in Equation (1.1). The composition of the inter-electrode gas influences the reduced electric field through

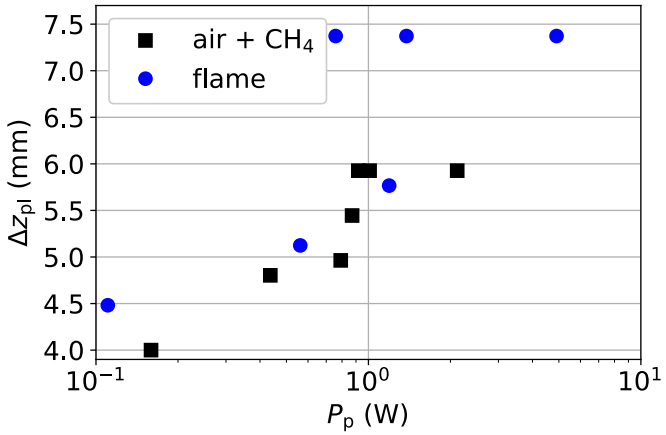

Figure 3.18: *Length of NRP corona discharges, Δz_{pl}, as a function of the discharges's mean power, P_p, for NRP discharges pulsed in a methane-air mixture ($\Phi = 0.8$) without flame (black squares) and with a flame (blue circles) in the inter-electrode area.*

the density, ρ, of the gas. Table 3.1 compares the gas densities and molar weights corresponding to the conditions presented in Figure 3.13 where the gas is air, in Figure 3.14 where the gas is a mixture of air and methane ($\Phi = 0.8$), and in Figure 3.15 where the influence of a laminar premixed flame on the fresh gas in the inter-electrode area is considered by assuming a heating of the gas close to the flame from 293 K to 900 K, corresponding to half the maximum temperature in the flame. Along with the gas density and the molar weights, the ratio of the reduced electric field in the inter-electrode mixture, E/n', to the reference case reduced electric field, E/n, in air at 293 K is determined by:

$$\frac{E/n'}{E/n} = \left(\frac{\rho}{\rho'}\right) \times \left(\frac{M'}{M}\right), \tag{3.1}$$

where ρ and ρ' are the densities of the mixture in air (reference case) and in the modified inter-electrode environment and M and M' are the molar weights of these same environments.

Due to the much lower density close to the flame, the reduced electric field increases from a reference value of 1 to 3.27. This increase in reduced electric field leads to the visual modification of the NRP corona discharges observed in Figure 3.15. The corresponding higher value of the conduction current accounts for the higher deposited energy in the case with a flame in the inter-electrode area (see black squares from Figure 3.12) as well as the change in the visual aspect of the NRP discharges observed in Figure 3.15 compared to Figures 3.13 and 3.14. Yet the heating of the gas takes place only very close to the flame front, meaning its influence also manifests itself only close to the flame, which

Table 3.1: *Densities and molar weights of fresh gas in the presented experimental conditions: in air, in air and methane ($\Phi = 0.8$) and in air and methane ($\Phi = 0.8$) heated at half the temperature from the flame, $T = 900\,K$.*

gas	T (K)	ρ (kg.m^{-3})	M (g.mol^{-1})	$\frac{E/n'}{E/n}$ (.)
air	293	1.20	28.85	1.00
air + CH_4 ($\Phi = 0.8$)	293	1.16	27.86	1.00
air + CH_4 ($\Phi = 0.8$)	900	0.38	27.86	3.07

is an explanation for the change in the length of the NRP corona discharges when they are close enough to the flame, *i.e.* when the electrical power of the NRP discharges is higher than 1 W.

The temperature is not the only criterion of importance here. A significant change in the NRP corona discharges has indeed been observed by the mere addition of methane in the air flow. Methane addition to the air accounts for a decrease in the mixture's density from 1.20 to 1.16 kg.m^{-3}, which is quite small compared to the density difference resulting from gas heating. Yet the visual effect of methane addition is significant, meaning that the mixture composition plays a role in the plasma chemistry that the consideration of the reduced electric field alone cannot take into account. A second effect is thus brought to light here: this influence of the mixture composition is in fact due to the modification of the spectroscopic properties of the mixture; the Electron Energy Distribution Function (EEDF) is indeed highly dependent on the nature of the inter-electrode gas and its modification by addition of a small amount of methane leads to a different energy branching and to different reaction pathways in the discharge process (see Starikovskaia 2014). These changes account for the increase in length of the NRP corona discharge (see Figures 3.13 and 3.14) itself due to an increase in the propagation velocity of the discharges.

Furthermore, as mentioned in Section 3.1, the flame is constituted of positive and negative ions and electrons (at a density around 10^{10} cm^{-3} for a methane-air premixed flame at atmospheric pressure). These charged particles have an effect on the behaviour of the discharge, compared to the cases without flame. This could explain the deviation of the corona discharge from the electrodes's axis which has been observed in Section 3.2 when the distance between electrodes and flame was decreased (see Figure 3.7). An experimental and numerical study by Nijdam et al. (2014) investigated the deviation of a streamer discharge generated by one high-voltage pulse in a pin-plate configuration. A laser beam, generating a density of ionised species of 10^9 cm^{-3}, crossed the

inter-electrode area. While generating no space-charge effects and inducing an only negligible change in the electric field, the pre-ionisation from the laser beam caused a significant deviation of the discharge towards the direction of the laser beam where the electrons concentration was higher. An estimation of the electron density in streamer discharges at these experimental conditions highlighted the fact that this effect was significant despite the fact that the pre-ionisation was three orders of magnitude below the ionisation in the streamer channel. The electron density of NRP glow discharges has been calculated in a configuration similar to the present study in Tholin and Bourdon (2011) and yielded a density of $10^{13}\,\mathrm{cm}^{-3}$. As mentioned in Chapter 1, the density of electrons in an atmospheric lean methane-air flame is about $10^{10}\,\mathrm{cm}^{-3}$, meaning that the electrons in the flame are expected to cause the same guiding effect. Additionally to this, also the effect of the flame on the electric field between the electrodes has to be taken into account. Considering the experimental configuration in Section 3.2, only part of the NRP field lines are interacting with the charged species in the flame. With the setup implemented in Section 3.3, the electric field lines are generated across the flame front (see Figure 3.15). The consequence is that, in Section 3.3, all the field lines interact with the charged species upstream, in, and downstream of the flame front, thus leading to a more pronounced interaction between flame and NRP discharges.

3.4 Conclusion

The effect of a lean laminar premixed methane-air flame on NRP corona discharges has been assessed experimentally in two different configurations. In the first one, as the NRP discharges were pulsed parallel to the flame front, the corona discharge was observed to deviate towards the flame front; this deviation increased as the flame moved closer to the discharge location. In the second setup, the electrodes were located on either sides of the flame, so that the NRP discharges were applied perpendicularly across the flame front. Both configurations allowed to observe an increase in the propagation velocity of the NRP discharges in the presence of a flame. These effects of a flame on NRP discharges were attributed to two different phenomena. The first is a thermal effect which, due to a density decrease in the gases close to the flame, results in an increase in the local reduced electric field, thus enhancing the NRP discharges. The second effect is the influence of the electrically charged flame on the electromagnetic field lines generated by the high-voltage pulses between the electrodes.

Additionally to these studies, another experiment has been performed with the second setup in order to evaluate the effect of mixture composition on NRP

corona discharges. It was observed that the discharge became significantly longer when a lean methane-air mixture flowed between the electrodes (compared to pure air). This influence of the inter-electrode gas composition is due to a change in the spectroscopic properties of the gas when methane was added to air. This addition of methane alters the EEDF, as well as the energy branching and reaction pathways in the discharge.

Thus, in both configurations when the electrodes are parallel or perpendicular to the flame, the plasma discharges are affected by the presence of the combustion front. Namely, the NRP discharges are enhanced by the presence of a flame. The closer the flame is to the electrodes, the stronger its effect on the plasma. In the following chapter, we will investigate the reciprocal effect.

Chapter 4

Effect of NRP corona discharges on laminar premixed flames

This chapter focuses on establishing the influence of NRP discharges on laminar premixed methane-air flames. The steady-state response of the flame to NRP discharges application is investigated in two different configurations, namely with electrodes parallel or perpendicular to the flame front. In the configuration with electrodes perpendicular to the flame front, the transient response of the flame is also investigated. In both electrode configurations (parallel and perpendicular to the flame), the influence of the mean power of the discharges on the stabilisation position of the flame is studied and an explanation, involving an enhancement of the laminar speed of the flame by transport of plasma-activated species and heat to the flame front, is proposed. The third section of this chapter focuses on modeling numerically the influence of NRP discharges on a lean premixed methane-air flame at atmospheric pressure and ambient temperature. The effect of ozone production and unburnt gas heating by the plasma discharges is analysed, showing the effect of ozone addition to be more significant compared to the thermal effect of the NRP discharges. This work has been performed in the Institut für Strömungsmechanik und Technische Akustik (ISTA) of the Technische Universität Berlin (TUB), Germany, and in the Clean Combustion Research Center (CCRC) of the King Abdullah University of Science and Technology (KAUST), Saudi Arabia. The results of Section 4.3.1 have been published in Heitz et al. (2017a) and the results of the numerical model presented in Section 4.4 have been published in Heitz et al. (2017b).

4.1 Introduction

During the last decade, non-equilibrium plasma discharges have drawn increasing attention for their potential in influencing combustion in gas turbines and aeronautical engines. Studies have demonstrated the effect of these discharges on various combustion-related phenomena such as mitigation of thermoacoustic instabilities, as in Moeck et al. (2013) and in Lacoste et al. (2013a), extension of a flame's stability domains in Barbosa et al. (2015) and modification of the pollutant emissions, in particular the nitric oxides in Kim et al. (2007) and in Lacoste et al. (2013a).

Non-equilibrium plasma discharges are known to affect the flame in two distinct manners. The first one is the thermal effect of the discharges, in which the energy of the discharges is converted into heat, thus acting as a local heating source, leading to an increase in the temperature of the inter-electrode gas. The second effect of plasma discharges is chemical: it manifests itself as a production of excited species, ionised species and radicals produced by the plasma discharges, which modify the reaction pathways of the flame.

In Lacoste et al. (2017a), the response, in terms of heat release rate, of laminar premixed flames to positive or negative steps of NRP glow discharges forcing has been investigated. An upstream movement of the flame was observed once the discharges were activated. This was attributed to an increase in the burning velocity resulting from higher reactivity of the gas treated by the plasma. These NRP glow discharges are known to have a negligible thermal effect, as has been verified in Lacoste et al. (2017c), so that an increase in laminar flame speed could not be attributed to heating of the unburnt gas alone, but rather to the generation of active species by the discharges.

However, the previous configurations were too complicated to allow for comparison with one-dimensional simulations of the influence of plasma discharges on the laminar flame speed. This influence has been mentioned previously; yet there is still a lack of information in the literature as to the thermal and chemical effects one can expect from NRP corona and glow discharges. The objective of this chapter is to provide quantitative information on the thermal and chemical impact of NRP corona discharges on a laminar premixed methane-air flame.

The effect of NRP plasma discharges on a flame is assessed experimentally in Sections 4.2 and 4.3, for corona discharges respectively parallel and perpendicular to the flame front. These two electrode configurations allow to compare the effect of the orientation of NRP discharges on a flame. The enhancement of the laminar flame speed is pinpointed as a possible cause for the flame dis-

placement upstream observed in both experiments when plasma discharges are applied. In Section 4.3, one-dimensional simulations of the flame are performed in order to estimate the potential flame speed enhancement resulting from the thermal and chemical effect associated with the NRP discharges. In Section 4.4, a numerical model is developed in order to predict the thermal and chemical effects of NRP corona discharges on laminar flame speed and adiabatic flame temperature.

4.2 NRP discharges parallel to flame front

4.2.1 Experimental setup

The experimental setup used here is detailed in Section 3.2.1 (see Figure 3.1(a)). The laminar ($Re = 480$) methane-air flame has an equivalence ratio of 0.75 ($S_L = 22.50\,\mathrm{cm.s^{-1}}$). The acoustic forcing used to stabilise the flame has a relative velocity amplitude, $u'_z/\bar{u}_z$, of 1.7 and a frequency, f_{ac}, of 250 Hz. The PRF of the discharges is maintained constant throughout this part of the study, at 30 kHz, while the voltage amplitude, U, of the discharges is varied between 4 and 10 kV, thus allowing to modify the deposited energy per pulse of the NRP discharges, E_p.

4.2.2 Experimental procedure

The effect of NRP corona discharges on the flame is assessed by observing the axial position of the flame, z_{fl}, as a function of the voltage amplitude of the discharges, U, and of the initial axial distance between flame front and electrodes, $z_{fl;0}$. The camera is positioned so as to visualise the inter-electrode area and the region above, where the flame is stabilised (see Figure 3.1(b)).

The protocol for the experiments is as follows: first the combustible methane-air mixture is ignited. Once the flame is stable at a given position by acoustic forcing, the NRP discharges are activated: the flame then moves in the upstream direction, towards the electrodes, and stabilises at another position. Several initial positions of the flame and several amplitudes of the voltage are considered, and photographs are taken for each case. An example of this phenomenon of flame upstream displacement is given in Figure 4.1, where the planar flame has an equivalence ratio of 0.75, the inter-electrode gap distance is 8 mm, and the initial axial distance between flame and electrodes is $z_{fl;0} = 6.14\,\mathrm{mm}$. The electrodes and the NRP corona discharges are also visible in this figure. It is

interesting to notice that, in this experimental configuration, the flame moves as a whole towards the electrodes, with no noticeable deformation of its surface.

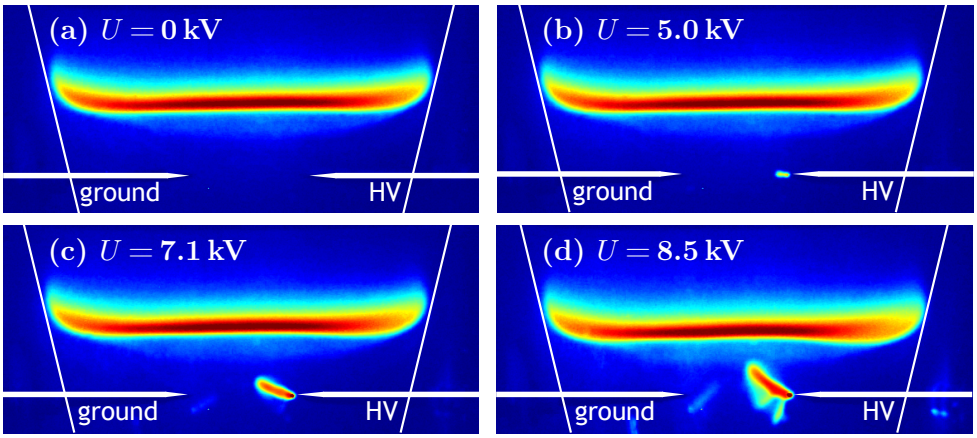

Figure 4.1: *Flame displacement as a function of applied voltage amplitude. The equivalence ratio is $\Phi = 0.75$, the inter-electrode gap distance is 8 mm and the initial distance between flame and electrodes is $z_{\mathrm{fl};0} = 6.14$ mm. The electrodes and the NRP corona discharges are located under (upstream) of the flame front.*

The flame displacement induced by NRP discharges is quantified based on the position of the flame's edge in its central part. This position is determined by means of the same algorithm for edge detection developed by Canny (1986) that has been used in Section 3.3. In the present study, applying this method allows for an identification of the flame front. An example of flame edge detection is given in Figure 4.2 where the algorithm is implemented to detect the leading edge of the flame front (black line).

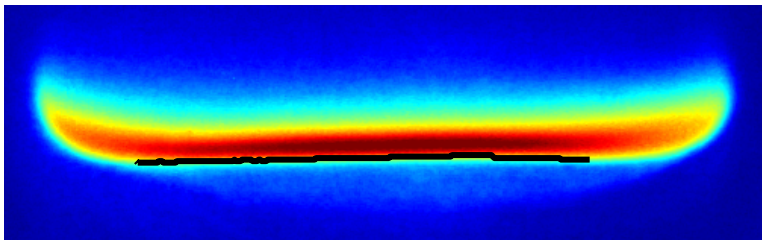

Figure 4.2: *Leading edge of the flame (black line) considered as the flame position.*

The mean position of this lower edge is considered as the flame position, z_{fl}. This flame position is compared to the initial flame position, $z_{\mathrm{fl};0}$, and the upstream displacement of the flame under NRP discharge application, Δz_{fl}, is deduced from these two parameters:

$$\Delta z_{\mathrm{fl}} = z_{\mathrm{fl}} - z_{\mathrm{fl};0}. \tag{4.1}$$

The displacement of the flame is analysed for different initial distances between flame and electrodes. The laminar flame speed enhancement, $\Delta S_L/S_L$, is calculated by invoking conservation of the flow rate between the initial section, where the diameter is D_0, and the stabilisation section when NRP discharges are applied, where the diameter is D_{NRP}:

$$\Delta S_L/S_L = \left(\frac{D_0}{D_{NRP}}\right)^2 - 1, \tag{4.2}$$

where $S_L = 22.50\,\mathrm{cm.s^{-1}}$ is the laminar flame speed without NRP discharges for an equivalence ratio of 0.75.

Equation (4.2) is based on the assumption that the flame is perfectly flat, and that the bulk velocity of the unburnt gases is equal to the laminar flame speed, S_L. Here, it is also assumed that the effect of acoustic forcing counterbalances the effects of intrinsic flame instabilities.

4.2.3 Results and discussion

The evolution of the flame position as a function of its initial distance to the electrodes, z_0, and of the voltage amplitude, U, is represented in Figure 4.3. Experimental data are represented with black squares for $z_0 = 1.79\,\mathrm{mm}$, blue circles for $z_0 = 3.80\,\mathrm{mm}$ and green triangles for $z_0 = 6.69\,\mathrm{mm}$. The lines represent linear fittings of these experimental data and show that the displacement of the flame does not depend on the initial flame-electrode distance within the considered range as the linear fits are almost parallel. The mean displacement of the flame is evaluated at approximately $0.28\,\mu\mathrm{m.kV^{-1}}$ for all three sets of experimental data.

The flame displacement is used to deduce the enhancement in laminar flame speed, $\Delta S_L/S_L$, resulting from the application of NRP plasma discharges, as in Equation (4.2). From the current-voltage profiles, the deposited energy is deduced according to the procedure detailed in Appendix A. The mean power of the NRP discharges, P_p, is deduced from their deposited energy, E_p, and their repetition frequency, by:

$$P_p = E_p \times \mathrm{PRF}. \tag{4.3}$$

Figure 4.4 displays the influence of the mean electrical power, P_p, of the NRP corona discharges on the enhancement of the laminar flame speed, $\Delta S_L/S_L$, for the three initial flame-electrode distances, z_0, considered in Figure 4.3. There is no experimental point corresponding to $z_0 = 1.79\,\mathrm{mm}$ (black squares) for the

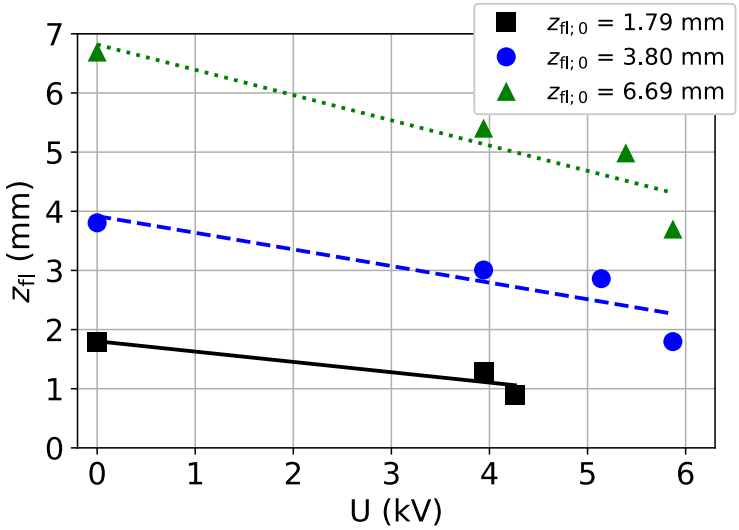

Figure 4.3: *Stabilisation position, z_{fl}, of the flame as a function of its initial position, z_0, and of the voltage amplitude, U, of the NRP corona discharges (black, blue and green markers). Black, green and blue lines are fitted from the experimental data.*

highest powers considered because of the flashback of the flame when the power was increased to values larger than 1 W.

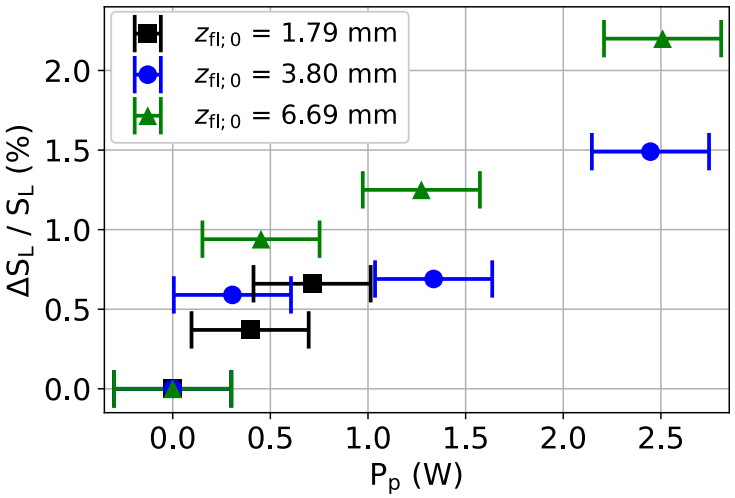

Figure 4.4: *Laminar flame speed enhancement, $\Delta S_L/S_L$, of a lean ($\Phi = 0.75$) premixed flame, as a function of mean electrical power of the pulses, P_p, and initial electrodes-flame distance, z_0. The PRF of the NRP discharges is 30 kHz and the discharges are in the NRP corona regime.*

The flame reaches a maximum upstream displacement of 2 mm for voltage am-

plitudes between 5 and 6 kV, corresponding to deposited energies per pulse of 50 to 80 μJ. With a PRF kept constant at 30 kHz, the corresponding maximum ratio of electrical to thermal power is $P_{\mathrm{el}}/P_{\mathrm{th}} = 0.5\,\%$. In this configuration, such an input electrical power leads to an increase in laminar flame speed up to 2.2 %.

The flame speed enhancement is highly sensible to the mean power of the NRP discharges for powers lower than 0.5 W. After this value, the sensibility of the flame speed enhancement to the NRP discharge power is less strong. The enhancement of the laminar flame speed can thus be estimated to be about 1.7 % for 1 W of NRP discharges power when $P_{\mathrm{p}} < 0.5$ W and 0.5 % for 1 W of electric power beyond this value. Due to the high uncertainty on the energy measurements (30 μJ.pulse^{-1} which is at least half the measured energy value), these two values also come with a high error.

It is interesting to take into account the fact that the Darrieus-Landau instability of the flame has been suppressed by application of an acoustic forcing of relative velocity amplitude 1.7 and acoustic frequency 250 Hz. Model 1, presented in Section 2.4.3.2 proved that this kind of acoustic forcing, with high relative velocity amplitudes and high frequencies, was detrimental to the NRP discharges in terms of the residence time of an air particle between the electrodes. While a quantitative comparison of the current forcing with the one from Chapter 2 is irrelevant—considering the differences between the two experimental configurations—, it is nonetheless possible to say that the acoustic forcing is probably reducing the number of pulses applied on each air particle, thus undermining the treatment of unburnt gas by NRP discharges. This means that the actual flame speed enhancement in a configuration where no acoustic forcing is needed would be higher than the one determined in this section.

In this section, an effect of NRP corona discharges on a laminar premixed methane-air flame has been observed: upon application of high-voltage pulses, the flame is translated towards the upstream direction and the electrodes. The enhancement in laminar speed of the flame has been deduced from this upstream displacement of the flame front and is expressed as a function of the mean power of the NRP corona discharges (see Figure 4.4). Unfortunately, the acoustic forcing used to stabilise the flame makes it difficult, in this experimental configuration, to decouple all the effects taking place, namely the interactions between flame, acoustic fluctuations and plasma discharges, as well as the heat losses to the quartz tube that change the flame dynamics. Thus, we move on to another configuration where the electrodes are perpendicular to the front of a laminar premixed stagnation flame (see Section 4.3).

4.3 NRP discharges perpendicular to flame front

4.3.1 Transient effect of NRP discharges

4.3.1.1 Experimental setup

The test-rig is displayed in Figure 4.5(a). An atmospheric pressure and ambient temperature methane-air premixture is set at an equivalence ratio of 0.7 with two rotameters (DK800, Krohne). It is delivered through the plenum of the burner with a perforated plate and honey- comb inside, followed by a converging nozzle (not displayed in Figure 4.5(a)). These elements are designed to ensure reduction of boundary layer thickness and a quasi-uniform velocity profile of the laminar flow at the nozzle outlet. A quartz tube of 10 mm inner diameter confines the mixture at the outlet of the nozzle. A cooled stagnation plate is placed 4 mm above the quartz tube. Impinging of the jet on the plate allows stabilisation of an approximately planar flame (see Figure 4.5(b)). Its rim is attached to the quartz tube so that the outer part of the flame is strongly curved.

NRP plasma discharges are generated perpendicular to the flame front between two tungsten pin electrodes. The high-voltage anode is a 0.1 mm-diameter tungsten wire, placed in the centre of the quartz tube. Despite the small diameter, the anode causes a velocity deficit on the centre axis and affects the flame shape. Figure 4.6 compares the flame (a) without central anode and (b) with central anode. The velocity deficit manifests itself as a deformation of the centre of the flame towards the upstream direction. A sharpened 1 mm-diameter grounded electrode is fitted in the centre of the stagnation plate, at a distance of 16 mm from the anode. A high-voltage pulse generator (FPG-Series, FID Technologies) generates pulses of 10 ns duration and a maximum amplitude $U = 3.5$ kV at a repetition rate of 30 kHz. A voltage probe (PHV 4002, PMK GmbH) and a current probe (Current Monitor Model 6585, Pearson Electronics) are used to evaluate the energy deposited in the inter-electrode area. An example of current and voltage profiles is given in Figure 4.7. The generated NRP discharges correspond to the corona regime, as defined in Pai et al. (2010b).

In Paragraph 4.3.1.3, the nanosecond plasma discharges are pulsed continuously between the two electrodes. In Pragraph 4.3.1.3, the pulses are gate-modulated: a given number of pulses, n, ranging from 100 to 30,000, is applied at a 30 kHz repetition rate in burst mode, with a modulation period of 2 s.

Visualisation of the flame is performed with a high-speed camera (FastCam

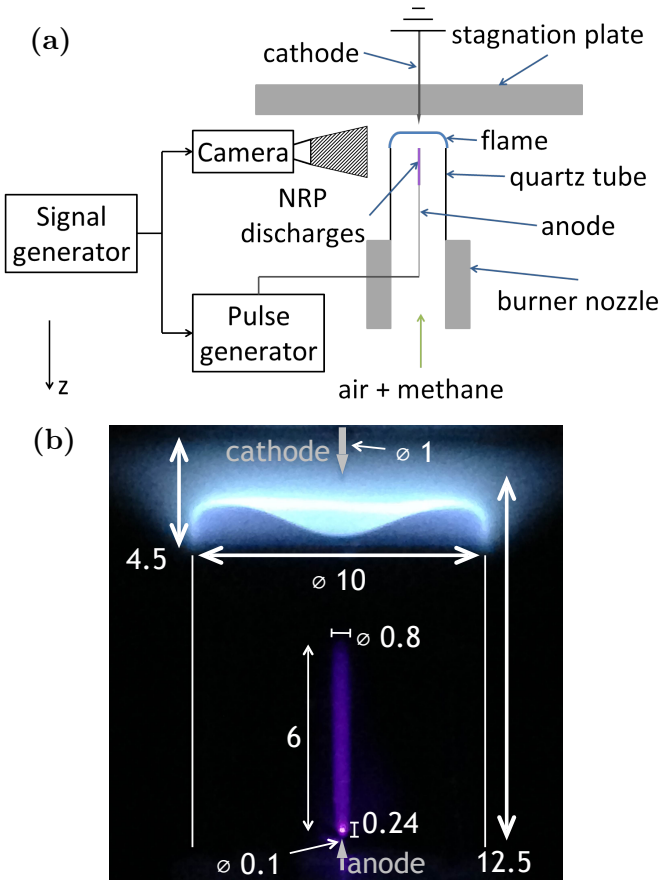

Figure 4.5: *(a) Experimental setup. The nozzle features a converging section, as well as a perforated plate and a honeycomb for laminarization and boundary thickness reduction (upstream of the sketch). (b) Photograph of the flame (blue) and NRP glow discharges (violet); the significant dimensions of the system are added in millimetres to Figure (b).*

SA1.1, Photron) featuring a frame rate of 1 kHz and an exposure time of 1 ms, equipped with a visible-range lens of 47 mm focal distance. A signal generator (33600A Series Trueform, Agilent) is used to synchronise the activation of high-voltage pulses with the camera exposure. The spatial resolution is 40 μm per pixel.

This visualisation has been made for three different sets of experimental conditions (summarized in Table 4.1), characterized by the two following parameters: thermal power of the flame, P_{th}, and voltage amplitude of the pulses, U.

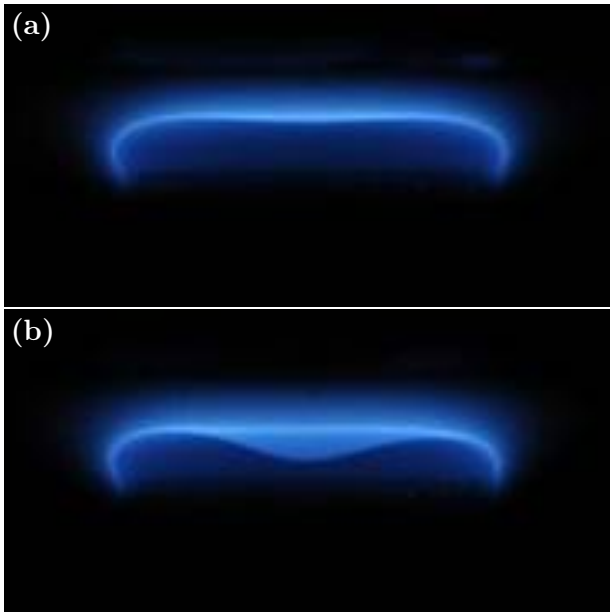

Figure 4.6: *Comparison of flame shape (a) without and (b) with central upstream anode. The thermal power of the flame, P_{th}, is 150 W.*

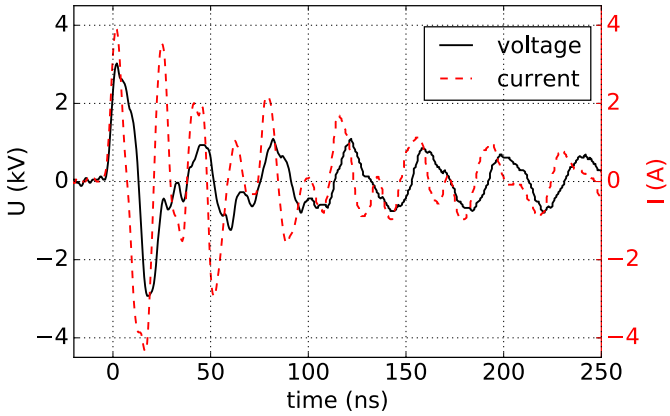

Figure 4.7: *Example of current, I, (dashed red line) and voltage, U, (solid black line) profiles.*

4.3.1.2 Experimental procedure

The flame displacement induced by NRP discharges is quantified based on the flame edge in the central part. The flame edge was identified using the same algorithm based on the detection of intensity gradients which is already implemented in Sections 3.3 and 4.2. This method allows an identification of the

Table 4.1: *Experimental conditions and corresponding label.*

Label of the set	P_{th} (W)	U (kV)
1	100	2.5
2	150	2.5
3	150	3.3

flame front. An example is given Figure 4.8: (a) was taken before application of NRP dis- charges; (b) was taken 40 ms after starting the discharges and (c) was taken 600 ms after starting the discharges. The black line is the lowest edge of the flame front; the mean position of the grey line is considered as the flame position, z, for this frame. For frames (b) and (c), the position of the flame before application of NRP plasma discharges as seen in (a) is also displayed for comparison.

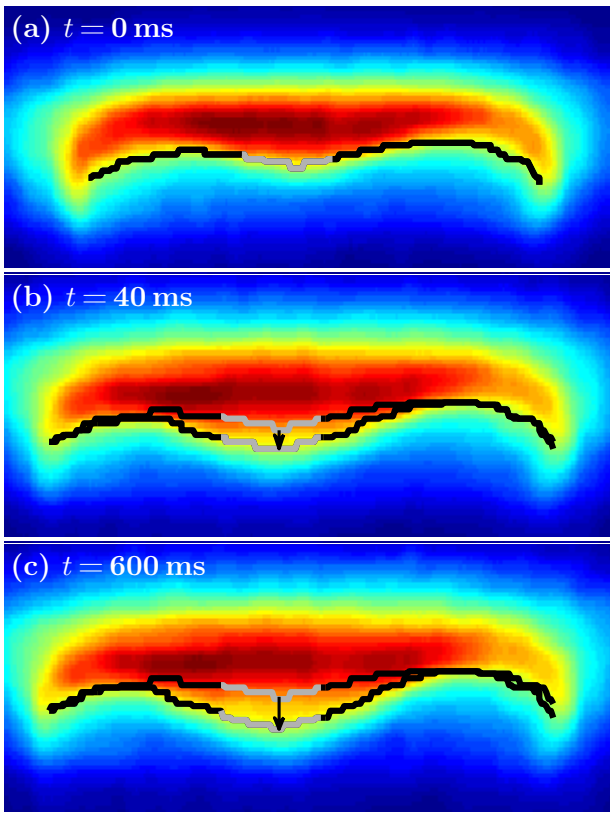

Figure 4.8: *Leading edge of the flame (black line) and area used for determination of the flame position (grey line) for different instants: (a) is taken before onset of NRP discharges; (b) is taken 40 ms after onset of NRP discharges; (c) is taken 600 ms after onset of NRP discharges. The position of the flame before NRP discharges application from (a) is added to frames (b) and (c) for comparison.*

The upstream flame displacement at a given instant, $\Delta z\,(t)$, is determined by comparing the position of the flame at this time, $z\,(t)$, to its initial position (without plasma discharges), z_{i}:

$$\Delta z\,(t) = z\,(t) - z_{\mathrm{i}}. \tag{4.4}$$

The mean displacement was determined thrice for each measurement and averaged. The resulting history of flame displacement was smoothed through a moving average lowpass filter:

$$\Delta \bar{z}\,(t) = \sum_{k=-s/2}^{s/2} \frac{\Delta z\,(t+k)}{s}, \tag{4.5}$$

where, s is the filter width, typically chosen as 10.

The uncertainty on the flame position is evaluated through its fluctuation when not subjected to NRP plasma discharges; this was determined as $\delta z = 50\,\mu$m.

4.3.1.3 Results and discussion

Steady-state effect

The maximum flame displacement under the action of continuously-pulsed NRP discharges allows for two observations on the influence of the experimental parameters: increasing the voltage amplitude of the discharges from 2.5 to 3.3 kV (set 2 to 3 from Table 4.1) causes a higher upstream displacement of the flame, from 0.5 mm to 0.65 mm. Higher voltage amplitude leads to a higher deposited energy in the inter-electrode area, which explains the enhanced influence of discharges on the flame. The flame displacement with the set 1 is 0.46 mm, and the displacement with set 2 is 0.50 mm, the difference of displacement is therefore within the experimental uncertainty.

Transient effect

Instead of the continuously pulsed discharges of the steady-state study, gated pulse trains are now considered. A given number of nanosecond discharges, n, is applied in burst mode, with a modulation period of 2 s. The upstream displacement of the flame as a function of time and number of applied pulses

is given in Figure 4.9; the red, black and green curves correspond respectively to the sets of experimental conditions 1, 2 and 3. It can be observed that the duration of the flame upstream displacement is increased with the number of applied pulses. During application of the first 2,000 pulses, the upstream displacement of the flame occurs fast, then slows down and finally reaches a maximum value around 10,000 applied pulses. When application of NRP discharges stops, the relaxation of the flame occurs in two steps: first a fast, linear relaxation, then a slower, exponential relaxation. If a small number of pulses is applied (for instance 2,000), only the fast upstream displacement occurs, the flame moving back to its initial position afterwards.

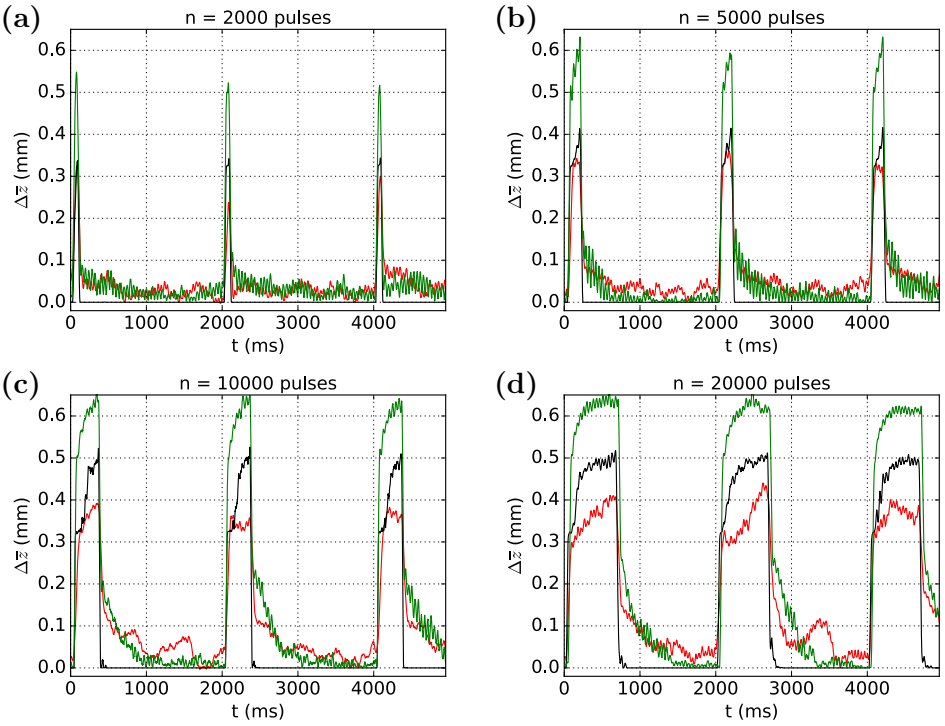

Figure 4.9: *Temporal evolution of the flame upstream displacement under the action of NRP discharges, for several trains of applied pulses, n. The red, black and green curves correspond respectively to sets of parameters 1, 2 and 3 from Table 4.1.*

Figure 4.10 represents the maximum upstream displacement of the flame as a function of the number of applied pulses for the three set of conditions. The behaviour of the flame submitted to NRP discharges is similar for all three conditions considered: a fast flame displacement over the first 2,000 pulses is observed, and the maximum flame displacement is reached after approximately 10,000 pulses; the upstream displacement at a given number of applied pulses decreases between set of conditions 1 and 2 and increases between set of conditions 2 and 3.

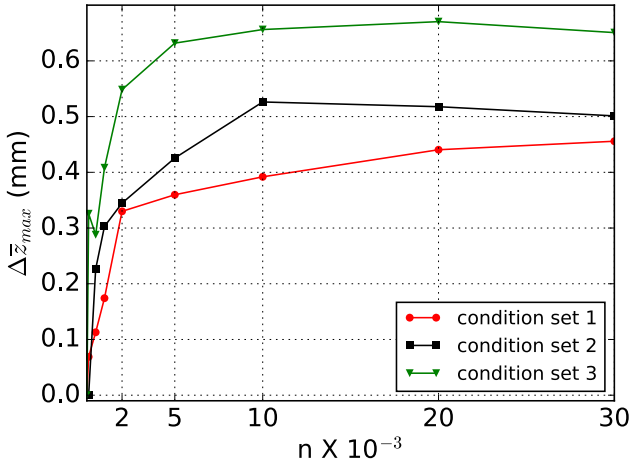

Figure 4.10: *Flame front displacement, $\Delta\bar{z}_{\max}$, as a function of the number of applied pulses, n, for the three sets of conditions from Table 4.1.*

Lacoste et al. (2017c) investigated the response of laminar premixed flames to a step forcing from NRP glow discharges. An upstream movement of the flame was observed once discharges were activated. This was attributed to an increase in the burning velocity resulting from higher reactivity of the gas treated by the plasma. The enhancement of laminar flame speed, ΔS_{L}, under application of NRP glow discharges is now estimated in the present study. First, a linear evolution of the axial gas velocity in the axial direction is assumed. Studies by Bergthorson et al. (2005); Bouvet et al. (2014) provide support for this assumption:

$$u_z(z) = az + b, \tag{4.6}$$

where a and b are constant. These two constants are determined with the velocity equilibrium conditions without and with flame speed enhancement:

$$u_z(z_1) = S_{\mathrm{L}}, \tag{4.7}$$

$$u_z(z_2) = S_{\mathrm{L}} + \Delta S_{\mathrm{L}}, \tag{4.8}$$

where S_{L} is the initial flame speed, z_1 and z_2 are the steady-state flame positions without and with application of NRP discharges. For the transition of the flame from z_1 to z_2, we can then formulate the kinematic equation:

$$\frac{dz}{dt} = S_{\mathrm{L}} + \Delta S_{\mathrm{L}} - u_z(z), \tag{4.9}$$

with the initial condition $z(0) = z_1$.

Combining Equations (4.6) and (4.9) yields the following expression for the flame position as a function of time:

$$z\,(t) - z_1 = (z_2 - z_1)\left(1 - e^{-\frac{\Delta S_\mathrm{L}}{(z_2 - z_1)}t}\right) \tag{4.10}$$

where ΔS_L is the increase of laminar flame speed when applying the NRP discharges. It remains to find the value of ΔS_L that fits the experimental evolution of $\Delta\bar{z}$; an example of this fitting is given in Figure 4.11 and the results for the three set of conditions are given in Table 4.2.

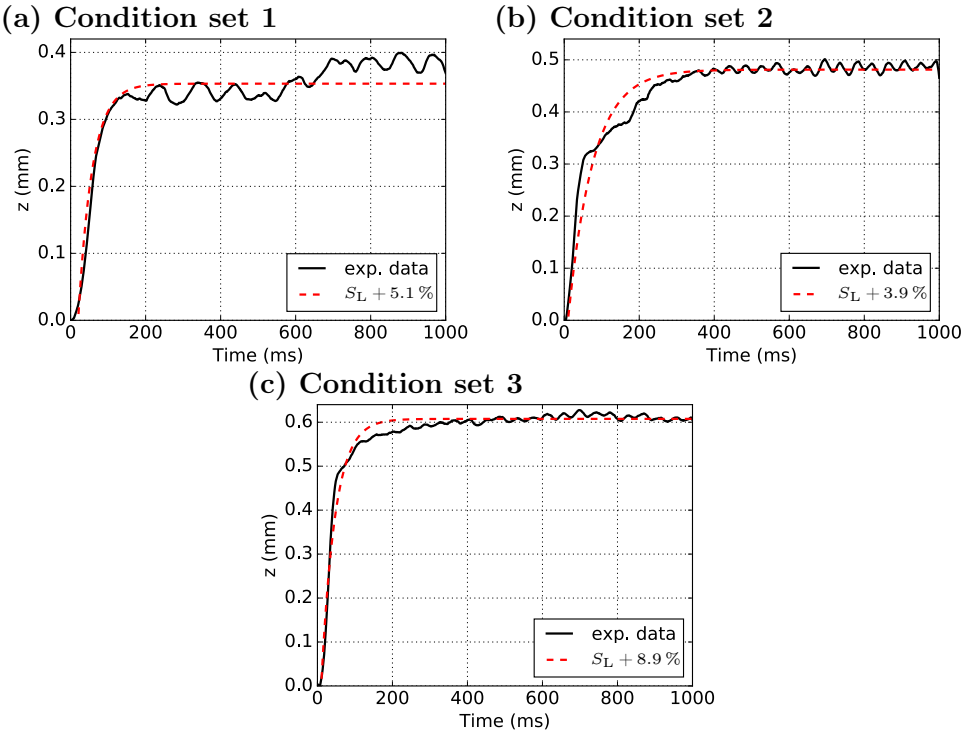

Figure 4.11: *Evolution of the flame upstream displacement; model from Equation (4.10) with ΔS_L providing best fit to the experimental data.*

Table 4.2: *Increase of flame speed with glow discharges. Initial flame speed, S_L, is 18.55 cm.s^{-1}, for the three sets of conditions from Table 4.1*

Set of conditions	ΔS_L (cm.s^{-1})	$\Delta S_\mathrm{L}/S_\mathrm{L}$ (%)
1	0.95	5.1
2	0.72	3.9
3	1.65	8.9

The observed enhancement, between 4 and 9 % of the initial laminar flame speed, confirms the potential of NRP glow discharges to increase the laminar flame speed in the studied configuration.

Figure 4.12 displays the upstream displacement of the flame under conditions of set 3. The dash-dotted vertical green line marks the visual appearance of the NRP glow discharges and the dashed green line marks their disappearance. The onset of flame upstream displace- ment is marked by the dash-dotted red line and the onset of downstream displacement by the dashed red line. This onset of flame up- or downstream displacement has been determined as the time when the up- or downstream displacement exceeds the spatial resolution, $z_{\mathrm{res}} = 40\,\mu$m per pixel, of the measurements:

$$\Delta\bar{z}\,(t) > z_{\mathrm{res}}, \tag{4.11}$$

$$(\Delta\bar{z}_{\mathrm{max}}\,(t) - \Delta\bar{z}\,(t)) > z_{\mathrm{res}}. \tag{4.12}$$

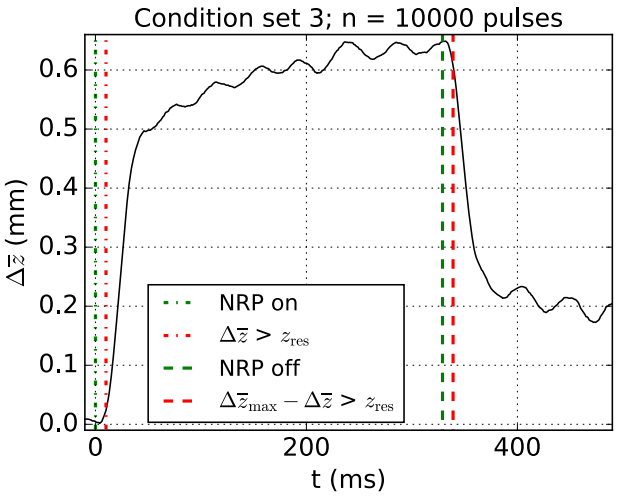

Figure 4.12: *Temporal evolution of flame displacement for conditions set 3 from Table 4.1 and a gate of n = 10,000 pulses.*

The delay between activation of plasma discharges and onset of the flame upstream displacement is approximately 10 ms. Convection of excited species and heat from the anode to the flame front may be responsible for the influence of plasma discharges on flame position. The convection time, t_{CV}, is defined as the time for a fluid element to be transported from the glow discharge location to the flame front and is estimated as:

$$t_{\mathrm{CV}} = \frac{d_{\mathrm{pf}}}{\bar{u}_z} \tag{4.13}$$

where d_{pf} is the distance between the centre of light of the NRP glow discharges and the flame front, and $\bar{u}_z$ is the bulk velocity in the quartz tube. The calculation yields $t_{\mathrm{CV}} = 14$ ms, which is close to the time between activation of plasma

discharges and onset of flame displacement (10 ms) observed in Figure 4.12. The time between visual disappearance of the nanosecond discharges and the start of the flame downstream displacement (back to its initial position) is the same and can therefore be attributed to the same convection process.

The thermal effect of the plasma is highlighted in Figure 4.13. After the linear relaxation (dash-dotted red line) attributed to the end of the convection of excited species to the flame, an exponential relaxation (dashed cyan line) of the flame displacement back to its initial position occurs. This exponential part of the curve can probably be attributed to a thermal effect, possibly a heating of the central anode when NRP discharges are active.

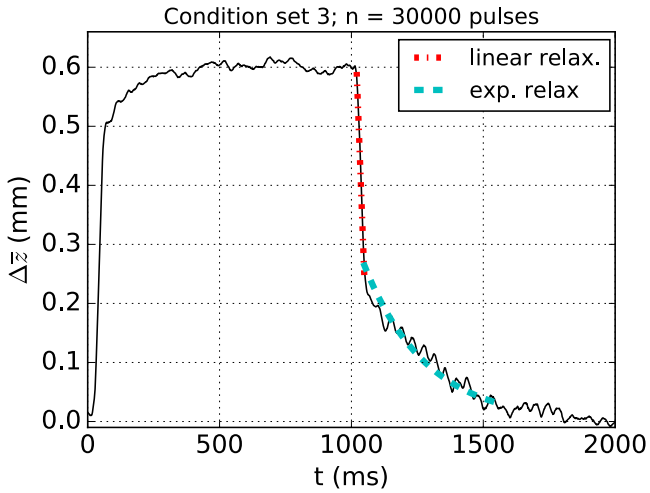

Figure 4.13: *Temporal evolution of flame displacement for conditions set 3 from Table 4.1 and a gate of n = 30,000 pulses. Linear relaxation is marked with the dash-dotted red line and exponential relaxation with the dashed cyan line.*

To conclude on this part of the study, the transient effect of nanosecond repetitively pulsed glow discharges on a laminar premixed stagnation flame was investigated. The application of NRP discharges induces an upstream displacement of the flame front. This displacement is a function of the number of pulses and their voltage amplitude: the more pulses are applied and the higher their amplitudes, the higher the resulting upstream displacement of the flame. The flame upstream displacement consists of a fast upstream movement during the first 2,000 pulses, then a slower displacement up to the most upstream location. The relaxation of the flame back to its initial position occurs first in a linear, then in an exponential manner.

An explanation based on convection of fluid elements with an increased reactivity was proposed: the particles excited and heated upstream by the NRP glow discharges are convected into the flame front and induce the flame displace-

ment upstream. It remains to give satisfactory details as to the nature and concentration of the active species. The coming numerical simulations from Section 4.4 are considered with this purpose in view and their comparison to the experimental results will allow for a better understanding of the parameters governing plasma-flame interactions. However, the fact that the flame in the present configuration is attached to the burner's nozzle induces a heat loss to the burner. This effect is detrimental if one wants to compare the experimental results to numerical simulations. Thus, another configuration is implemented in Section 4.3.2 where laminar premixed stagnation flames are detached from the nozzle of the burner.

4.3.2 Steady-state effect

4.3.2.1 Experimental setup

The experimental setup implemented here is the same as was used in Section 3.2. A complete description of the configuration and the material used can be found in this previous section, and a scheme of the setup is provided in Figure 3.8. Throughout the presented experiments, the Pulse Repetition Frequency (PRF) is varied between 1 and 28 kHz. The upper limit for the PRF has been set at 28 kHz because of the risk of flame flashback at higher repetition frequencies.

4.3.2.2 Experimental procedure

Chapter 3 focused on the effect of the flame on the NRP plasma discharges. There, the NRP discharges have been observed. Thus the OH^* emission coming from the flame has been minimised by synchronizing the camera intensification with the high-voltage pulses and keeping an integration time as low as possible. The purpose of this chapter is to observe the reaction of the flame to NRP discharge application, meaning it is here necessary to acquire the luminous emission from the flame without the one coming from the NRP discharges. In order to do so, the gate delay of the ICCD camera has been set to 1 μs and the gate width maximized during this period between pulses (for instance set to 48 μs when the PRF is 20 kHz). This way, the camera opens 1 μs after each high-voltage pulse, enough delay to observe no plasma light emission at all (as mentioned in Section 3.3.2, the plasma light emission ceases after approximately 200 ns), and collects only the light from the flame. The number of gates per exposure is adjusted in order to obtain a flame light emission as bright as possible (within the limits of saturation of the CCD). Table 4.3 displays the parameters used for each experimental condition.

Table 4.3: *Settings for acquisition of the flame with the ICCD camera. In order to avoid collecting the light emission of the NRP discharges, the gate delay is systematically set to 1 µs. The gain of the intensifier is set at its maximum.*

PRF (kHz)	gate width (μs)	number of gates per exposure
1	998	3
5	198	15
10	98	25
15	64	50
20	48	60
25	38	100
26	36	100
27	35	100
28	33	100

Once the images of the flame are obtained, the position of the flame front is detected by means of an algorithm for edge detection. This same algorithm has already been implemented in Sections 3.3 and 4.2. The spatial uncertainty in the experiments is 80 μm, which corresponds to the size of one pixel.

4.3.2.3 Results and discussion

The visual effect of NRP plasma discharges on the stagnation flame is displayed in Figure 4.14. The leading edge of the flame is detected (red, green and blue lines). Two areas of interest are displayed in the figure: the position of the centre of the flame (green line) and the position of its edge (blue lines). These two positions are used in order to quantify the displacement of the flame. For visual comparison, the mean position of the flame's centre without NRP discharges application (see Figure 4.14(a)) is indicated on each picture (cyan line).

The maximum displacement of the flame's leading edge is observed at the centre (see green line from Figure 4.14). This maximum displacement is considered to be the result of two effects: the first one is the upstream translation of the entire flame, quantified by determining the displacement of the edge of the flame (blue lines from Figure 4.14), while the second effect is the increase in the surface of the flame by the NRP discharges, determined by the increase in surface of the leading edge (the red, green and blue lines from Figure 4.14 are the flame's length, the surface is deduced by considering the flame to be axisymmetric).

As NRP discharges are applied in the inter-electrode area, the temporal evolu-

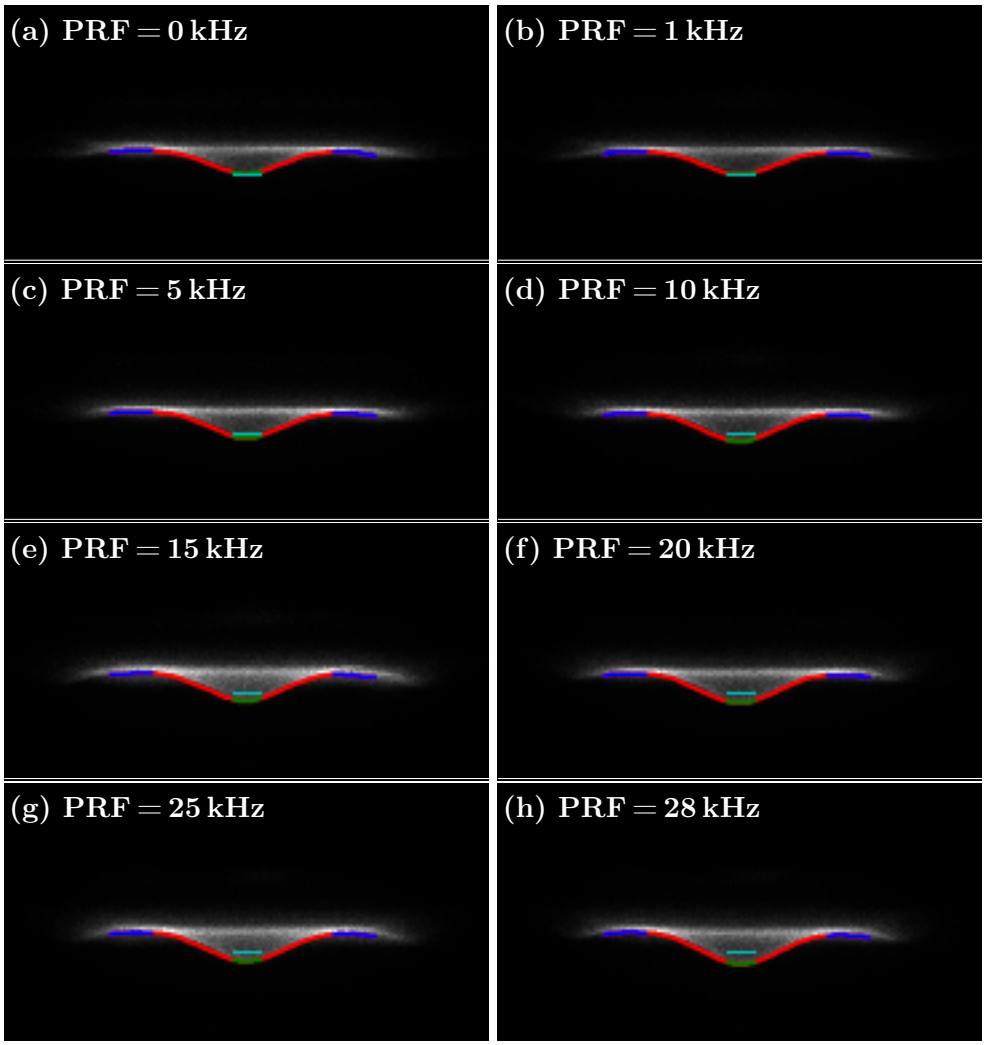

Figure 4.14: *Effect of the PRF on the steady-state position of the leading edge of a laminar premixed methane-air flame with an equivalence ratio of 0.8. The flame's leading edge is detected (red line). The position of the centre (green line) and of the edges (blue lines) of the flame are deduced. The cyan line corresponds to the mean position of the flame's centre when no discharges are applied (corresponding to picture (a)).*

tions of current and voltage are measured for each PRF, in the manner presented in Appendix A, and the results are given in Figure 3.12 (see Section 3.3.3). The influence of the discharges's pulse repetition frequency on the stabilisation position of the flame is quantified by comparing the steady-state position of the flame front in its centre, z_0, (see green line from Figure 4.14) and at its edge, z_R, (see blue lines from Figure 4.14) with NRP discharges pulsed at the PRFs from Table 4.3. Figure 4.15 compares the evolution of the mean displacement of the flame's centre, Δz_0, with the displacement of its edge, Δz_R, as a function of

the PRF. The reference position for the displacement is the case without NRP discharges applied to the flame, as displayed in Figure 4.14(a).

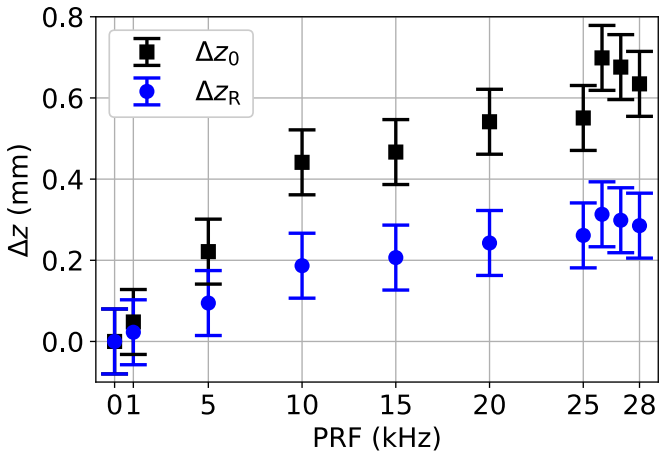

Figure 4.15: *Displacement of the centre part of the flame, Δz_0, (black squares) and of the outer part of the flame, Δz_R, (blue circles) as a function of the PRF of the NRP discharges. The reference position is the case without discharges (PRF = 0 kHz).*

The centre of the flame moves in the upstream direction for repetition frequencies up to 26 kHz. At this PRF value, the flame reaches a maximum displacement of about 0.7 mm, then slightly decreases for the next two PRFs (27 and 28 kHz) considered. This decrease, of about 70 μm, is comparable to the uncertainty for these experiments (80 μm). The edge of the flame moves following the same trend as the centre, with a displacement of half the value in the centre, peaking at 26 kHz with 0.37 mm. The displacement of the flame's edge also decreases beyond 26 kHz, although the maximum decrease is about 20 μm, thus negligible compared to the uncertainty of the experiments.

From Figure 3.12, the relation between the PRF and the deposited energy per pulse is known. The mean power of the NRP discharges, P_p, is deduced from these two quantities by means of Equation (4.3). The influence of the mean discharge power on the flame's displacement is thus displayed in Figure 4.16. The obtained power of the discharges is lower than 5 W; as a comparison, the thermal power of the flame is 250 W. As mentioned in Section 3.3.3, the NRP discharges do not stretch out from the high-voltage electrode all the way to the ground, but rather stop at the flame front (see Figure 3.15). For this reason, the measured energy of the NRP discharges is considered to be mostly distributed in the unburnt gases and inside the flame front itself.

The obtained data allow to distinguish two different trends, which are visible for both curves: first, when $P_p < 0.5$ W, the stabilisation position of the flame is highly dependent on the mean power of the NRP discharges. Beyond this power

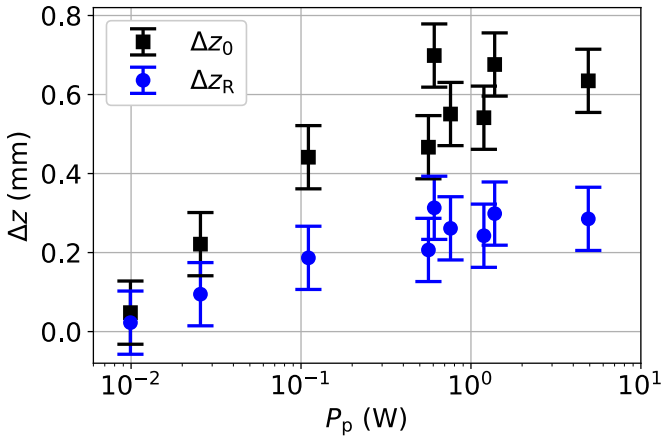

Figure 4.16: *Displacement of the centre part of the flame front, Δz_0, (black squares) and of its outer part, Δz_R, (blue circles) as a function of the mean power of the NRP discharges, P_p.*

value is the second trend where the position of the flame is not so sensible to the mean power of the NRP discharges any more. This is comparable to what has been observed in Section 4.2 for the electrodes parallel to the flame front. The flame's response is more sensitive to changes in the discharge power for low P_p than for higher P_p. A saturation seems to appear for $P_p > 0.5\,W$ here and 1 W in the previous configuration.

The deformation of the flame's surface is determined by evaluating the change in surface of the flame's leading edge when NRP discharges are applied to it. The length of the flame (see red, green and blue lines from Figure 4.14) is determined for each case and the surface of the flame, A_{fl}, is deduced by considering the flame as axisymmetric. The relative increase in the flame's surface, $\Delta A_{fl}/A_{fl}$, is calculated by subtracting the reference surface of the flame (when no NRP discharges are applied to it) from the surface of the flame submitted to NRP discharges, then dividing this quantity by the reference surface of the flame. Figure 4.17 displays the dependence of the flame area to the mean power of the NRP corona discharges. Each experimental point is annotated with the corresponding PRF.

Two different trends of the flame area increase are distinguished in Figure 4.17: for PRFs smaller than 25 kHz, the flame area increase when the power of the discharges is increased, until it reaches a saturation point for electrical powers higher than 0.5 W. For repetition frequencies higher than 25 kHz, the flame area decreases with the PRF, though the power of the discharges keeps increasing with the repetition frequency. This domain where PRF > 25 kHz also corresponds to the point where the NRP corona discharges start to reach up to the

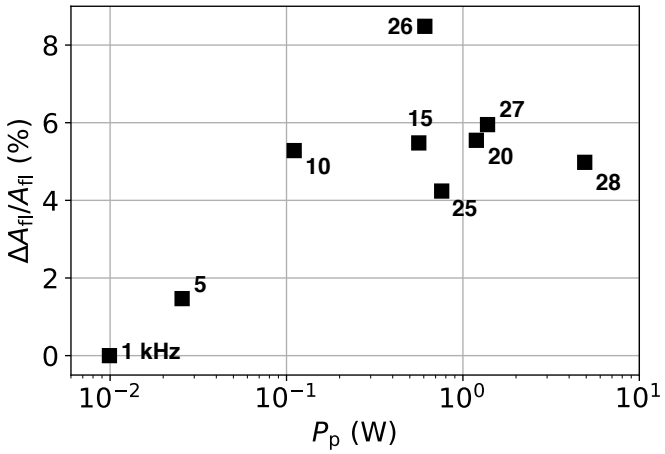

Figure 4.17: *Relative change in the flame's surface, $\Delta A_{\mathrm{fl}}/A_{\mathrm{fl}}$, as a function of the mean power of the NRP discharges, P_{p}. The NRP discharges touch the flame from PRF = 25 kHz on.*

flame front, as in Figures 3.15(e) and (f).

Considering the results in Figures 4.16 and 4.17, two different behaviours of the flame under application of NRP discharges are distinguished: first, when PRF $<$ 25 kHz, the surface of the flame increases with the power of the applied pulses, while it also translates in the upstream direction. For repetition frequencies higher than 25 kHz, the flame area decreases with the applied power of the discharges. This highlights the fact that, once the NRP discharges reach up to the flame front, the response of the flame to the discharges changes: from this point (PRF $>$ 25 kHz), the displacement of the flame and the deformation of its surface both remain strong; yet, an increase in the mean power of the NRP discharges seems to induce the flame to become more compact, instead of increasing its surface.

The fact that the flame's surface is deformed is hard to link to a local increase in the laminar flame speed because of the fact that the energy distribution across the surface of the flame is unknown. This energy distribution is assumed to be non-homogeneous and would have to be known in order to deduce the effect of energy on the flame's curvature and interpret the deformation in Figure 4.17 in terms of laminar flame speed enhancement.

4.4 Numerical model for estimation of NRP discharges effect

A numerical model is here developed to evaluate the thermal and chemical effects of NRP corona discharges and their relative influence on the burning velocity and the adiabatic temperature of a one-dimensional stagnation flame. In the first scenario considered (named chemical scenario), all the energy of the NRP corona discharges is used to excite electrons, thus inducing subsequent reactions eventually leading to ozone production. This unique species has been chosen in order to simplify the model and because it has a long lifetime. In addition, as no strong heating of the gas by the NRP corona discharges can be expected, ozone is likely to be the dominant species. Another model (named thermal scenario) is then developed to evaluate the effect of the NRP discharges on the flame if all the electrical energy of the discharges were to be converted to thermal energy and thus increased the temperature of the unburnt gases. A third, intermediate scenario (named mix scenario) considers that one half of the plasma energy goes to electron excitation and the other half to unburnt gas heating. In this approach, no transverse diffusion, either of heat or of active species, are considered.

4.4.1 Presentation of the model

The model has been developed based on the experimental configuration presented in Section 4.3.1.

4.4.1.1 Chemical scenario

In this first scenario, all the plasma energy serves to excite electrons. The focus of this scenario is on the ozone concentration resulting from the reactions in the plasma discharge. Ozone is a long-lived species which has been proved to be one of the main products of non-equilibrium plasma discharges (see Chen and Davidson 2002) and is also known to have an influence on a flame's burning velocity (see Ombrello et al. 2010b). Due to the convection from the high-voltage electrode to the flame front (with a convective time of a few milliseconds on average when the NRP discharges do not touch the flame front), only the long-lived species can affect the combustion kinetics. Although NOx particles, excited molecular and atomic oxygen could also present some interest towards modifying the considered flame properties, we only focus on the effect of ozone in this study. Indeed, NOx is usually produced in the case

of electrical discharges that significantly heat the gas (typically NRP spark discharges, as in Lacoste et al. 2013a) and the lifetime of atomic oxygen in air is short (about 25 μs, see Stancu et al. 2010). In a first step, two reactions of electron-impact dissociation of oxygen and excitation of nitrogen, happening during the 10 ns of the pulse, are considered:

$$N_2 + e^- \rightarrow N_2^* + e^-, \tag{4.14}$$

$$O_2 + e^- \rightarrow 2\,O + e^-. \tag{4.15}$$

A study by Nagaraja et al. (2015) established a path flux analysis of species production by NRP discharges at low pressure ($p = 0.033$ atm). The NRP glow discharges are pulsed in a lean ($\Phi = 0.5$) premixed hydrogen-air flame. The 200 discharges of the pulse train have a duration of 7 ns, an amplitude of 14 kV and are pulsed at a PRF of 40 kHz, yielding an energy per pulse of 3 mJ. This path flux analysis displays that, in this configuration, 75 % of atomic oxygen production by the NRP glow discharges results from reactions (4.14) and (1.3). A third reaction of nitrogen quenching is added, providing additional atomic oxygen:

$$N_2^* + O_2 \rightarrow N_2 + 2\,O, \tag{4.16}$$

Rusterholtz et al. (2013) have shown that it takes 25 ns for the excited nitrogen to be totally quenched, so this duration is considered in the model for Reaction (4.16). Finally, ozone production is considered with the three-body reaction:

$$O_2 + O + M \rightarrow O_3 + M, \tag{4.17}$$

where M is either nitrogen or oxygen. This reaction takes place during the convection time (taken at its minimum value of 1 ms) of the gases from the plasma discharge to the flame. Several studies, such as Chen and Davidson (2002); Ombrello et al. (2010b), mention this reaction as the most significant in terms of ozone production.

For the reaction:

$$A + B \rightarrow C + D, \tag{4.18}$$

the reaction rate, ω, is:

$$\omega = -\frac{d\,[A]}{dt} = -\frac{d\,[B]}{dt} = \frac{d\,[C]}{dt} = \frac{d\,[D]}{dt} = k \times [A] \times [B]\,, \tag{4.19}$$

where k is the reaction rate constant and [A], [B], [C] and [D] are the molar concentrations in species A, B, C and D. Integration of (4.19) yields the temporal evolution of each species involved in the reactions from this model. Particularly, this method allows to obtain the temporal evolution of the concentrations of excited nitrogen in (4.14), atomic oxygen in (4.15) and (4.16), and ozone in (4.17). The electron number density is supposed to be constant for the calculations of Reactions (4.14) and (4.15) which both take place during the 10 ns of the high-voltage pulse.

The reaction rate constants from (4.14) and (4.15) as a function of the applied reduced electric field were determined by solving the Boltzmann equation with the BOLSIG+ code developed by Hagelaar and Pitchford (2005). The process of determination of the reaction rate constants for these two reactions, as well as a comparison between the results yielded by several databases are given in Appendix C. A set of cross sections for electron collisions with nitrogen and oxygen molecules were taken from the IST-Lisbon database on the BOLSIG+ website (see Alves 2014). The reaction rates for (4.16) and (4.17) are taken respectively from Rusterholtz et al. (2013) and Ibraguimova et al. (2003). The BOLSIG+ code also provides electron temperatures as a function of the reduced electric field. For electric fields estimated between 40 and 500 Td, the electron temperature, T_{e^-}, is between 1.2 and 10 eV. The number density of electrons, n_{e^-}, is taken as $1.2 \times 10^{15}\,\mathrm{cm}^{-3}$, an average value estimated from Tholin and Bourdon (2011) for NRP glow discharges with an electric field similar to the range considered in this study. The volume considered for the discharge energy deposition, V_1, is defined as the plasma region where the light emission is maximum (see Figure 4.5(b)). This volume is represented as a cylinder of 400 μm radius and 240 μm height, so that its value is $0.12\,\mathrm{mm}^3$. Multiplying the electron number density by the discharge volume and the electron temperature allows for an estimation of the deposited energy of the discharges, E_p:

$$E_\mathrm{p} = n_{e^-} \times V_1 \times T_{e^-}. \tag{4.20}$$

This energy lies between 0.03 and 0.25 μJ per pulse. It has not been possible to measure the deposited energy in Section 4.3.1 in a quantitative manner, but the electrical energy of NRP corona discharges is known to be of the order of a few microjoules per pulse (see Pai et al. 2009). This range of energy values is lower than the energies measured for the NRP discharges in Sections 3.2 and 3.3, but as the energy measurement uncertainty is about $30\,\mu\mathrm{J.pulse}^{-1}$, these values can be compared with the experimental energy measured for PRF < 15 kHz. Considering the dimensions of the volume V_1 and the 30 kHz PRF of the discharge, a volume of gas flowing into the discharge region is subjected to 8 high-voltage pulses before exiting it.

4.4.1.2 Thermal scenario

In this second scenario, the energy is considered to be deposited integrally in the form of thermal energy within the discharge volume, V_1, defined in Section 4.4.1.1. Therefore, the unburnt gases flowing through the discharge are heated with the same energy range as in Section 4.4.1.1. The temperature increase of the gas is then in the range of 1 to 11 K. After this temperature increase, the gas at temperature T_1 exits from the discharge volume and expands to a volume V_2, decreasing the gas temperature in the process. Assuming an adiabatic expansion of the gas, the new volume, V_2, is determined with:

$$p_1 \times V_1^{\gamma_1} = p_2 \times V_2^{\gamma_2}, \tag{4.21}$$

where p_2 is the atmospheric pressure and γ_1 and γ_2 are the heat capacity ratios, before and after expansion of the gas, respectively. The new gas temperature after expansion, T_2, is then deduced from the ideal gas law.

4.4.1.3 Mix scenario

This scenario considers an intermediate situation where 50 % of the energy goes into electron excitation, resulting in approximately half the final ozone concentration compared to the chemical scenario. The other half of the discharge energy goes into unburnt gas heating, leading to approximately half of the temperature increase from the thermal scenario. This case is considered in order to observe the possible existence of a synergetic effect between thermal and chemical effects on the flame characteristics.

4.4.1.4 Effect of the different scenarios on the flame

Once the ozone concentrations and temperature increases are estimated over the entire energy range considered, they are implemented in a Cantera (see Goodwin et al. 2017) script allowing to determine laminar flame speed and adiabatic flame temperature of a one-dimensional stagnation flame. This script is presented in Appendix D. The GRI-Mech 3.0 reaction mechanism from Smith et al. is designed for use in natural gas-air combustion mixtures; its basic version features 53 species and 325 reactions. Here, it is modified to include reactions between ozone and air molecules (taken from Ibraguimova et al. 2003, Atkinson et al. 2003 and Starik et al. 2007). The reaction mechanism is then

validated with experimental data published by Wang et al. (2012) and Gao et al. (2015). Details on the modification of the reaction mechanism and the validation results are presented in Appendix E. In the following simulations, the pressure is one atmosphere, the initial fresh gas temperature is 293 K, the bulk velocity of the methane-air mixture is 0.8 $m.s^{-1}$ and the equivalence ratio is 0.8. The axial separation distance between the inlet (the nozzle of the burner) and the stagnation plate is 7.8 mm. The fresh gas temperature and ozone content of the gas are modified according to the results from the three scenarios presented in Sections 4.4.1.1, 4.4.1.2 and 4.4.1.3.

4.4.2 Results and discussion

4.4.2.1 Chemical scenario

As the electric field—and so the energy deposited by each NRP discharge—is increased, so is the ozone production. Figure 4.18 displays the concentration of ozone in the fresh gas, $[O_3]$, as a function of the energy per pulse, E_p, also expressed in terms of the reduced electric field, E/n. The ozone molecules come from the recombination reaction of atomic oxygen with molecular oxygen (4.17). For this reason, two pathways of ozone formation are distinguished: the first one where atomic oxygen is produced by direct electron-impact dissociation, as expressed in (4.15), and the other one coming from the excitation and quenching of nitrogen, as in (4.14) and (4.16). Ozone generated by this first pathway is represented by the dotted blue line and ozone originating from the second pathway by the dashed green line.

Ozone production is strongly dependent on the input energy of the plasma discharges. The total concentration of ozone reaches 10,000 ppm at the highest energy considered. The pathways decomposition shows that both pathways considered (direct electron-impact dissociation of oxygen, see blue curve, and nitrogen excitation and quenching, see green curve) are responsible for a significant share of the total amount of atomic oxygen produced on the entire range of energy considered.

4.4.2.2 Thermal scenario

The linear increase in the temperature of the unburnt gas, ΔT, as a function of the deposited energy, E_p, is displayed in Figure 4.19. For the considered range of deposited energies, the resulting temperature increase reaches a maximum of about 10 K.

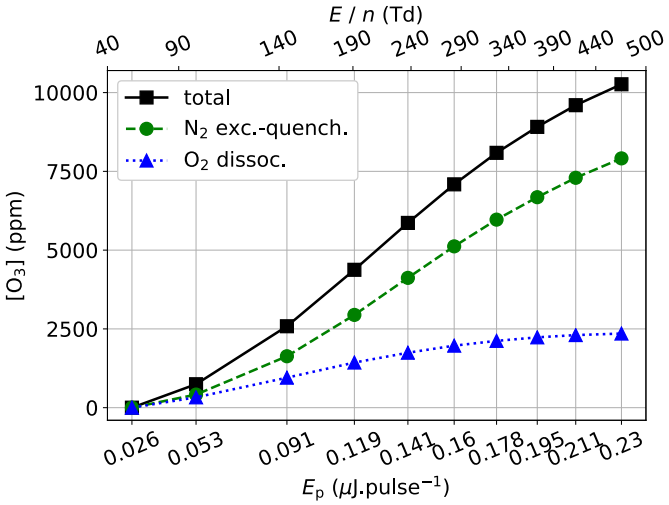

Figure 4.18: *Ozone production,* $[O_3]$*, as a function of deposited energy,* E_p*, and reduced electric field,* E/n*.*

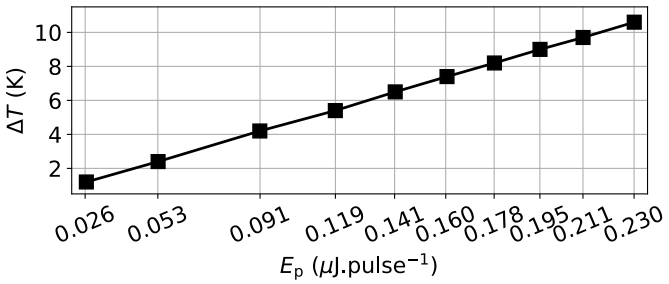

Figure 4.19: *Increase of the temperature of the unburnt gas,* ΔT*, as a function of the plasma-deposited energy per pulse,* E_p*.*

4.4.2.3 Comparison of thermal and chemical scenarios

Figures 4.20 and 4.21 show the evolution of the laminar flame speed enhancement, $\Delta S_L/S_L$, and the adiabatic flame temperature increase, $\Delta T_{ad}/T_{ad}$, as a function of the deposited energy per pulse, E_p.

Due to the linear evolution of both the laminar flame speed and the adiabatic flame temperature with the ozone concentration in the fresh gases and with the fresh gas temperature, the adiabatic flame speed and temperature evolve with the energy per pulse in a similar manner as the ozone content and temperature increase from Figures 4.18 and 4.19. The flame speed enhancement provided by ozone (solid black line) reaches 25 %, a value far higher than the thermally-induced flame speed increase (dashed green line) which reaches 7 %

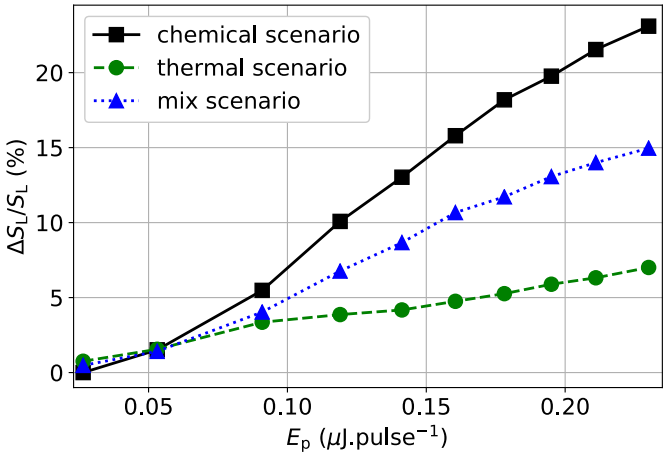

Figure 4.20: *Laminar flame speed enhancement, $\Delta S_L/S_L$, as a function of the deposited energy per pulse, E_p.*

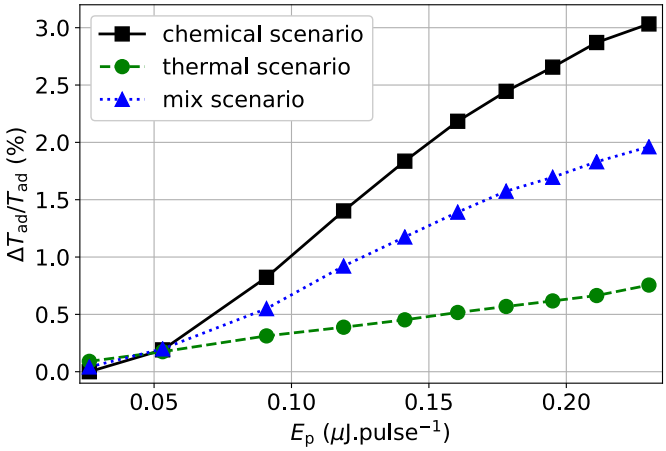

Figure 4.21: *Adiabatic flame temperature enhancement, $\Delta T_{ad}/T_{ad}$, as a function of the deposited energy per pulse, E_p.*

for a similar deposited energy. The enhancement at low energy deposition is similar for all three scenarios, but increases far more when all the energy goes to ozone production, than when it goes to the heating of the unburnt gases. The enhancement provided by the mix scenario (dotted blue line) corresponds to the intermediary value in-between the 100 % thermal and 100 % chemical cases. The model in its current state does not display the existence of a synergetic effect between plasma-induced unburnt gas heating and plasma-produced ozone.

The trend of adiabatic flame temperature evolution is similar to the one of

the laminar flame speed, but smaller by an order of magnitude. The ozone-induced flame temperature increase is eight times higher than the one induced by heating of the unburnt gas.

4.4.3 Comparison with the experimental results

The numerical model presented in Part 4.4.1 yielded a maximum increase in the fresh gas temperature of 10 K and a maximum ozone production of 10,000 ppm. The increase in unburnt gas temperature and the generation of ozone by the NRP discharges are now estimated by using the experimental data obtained in Section 4.3.

The upstream displacement of the flame is considered as the comparison parameter between numerical calculations and experiments: either the ozone concentration in the inlet mixture or the temperature of the fresh gases is increased until the displacement of the computed flame corresponds to the one observed experimentally. Considering the one-dimensional nature of the numerical simulations performed here, only one displacement of the flame could be considered; we chose to use the position of the flame in its centre, Δz_0 (see black squares from Figure 4.16). This provides an estimation of the thermal and chemical production of the NRP discharges for each applied discharge power.

4.4.3.1 Influence of ozone concentration and fresh gas temperature on the flame displacement

Figure 4.22 displays the influence of (a) unburnt gas temperature increase, ΔT_u, and (b) ozone concentration in the inlet gas, $[O_3]$, on the displacement of the centre of the flame, Δz_0. The energy per pulse, E_p, calculated to obtain the ozone concentration and unburnt gas temperature increase is also indicated in the figure. In these simulations, the axial position of the flame is assumed to be the position of maximum concentration in OH while the position of the experimental flame has been detected with the edge of OH^* emission. These two different criteria for the flame position induce a shift between the positions of the computed and experimental flames. In addition, the experimental flame is not perfectly axisymmetric; therefore some correcting factors have been introduced in order to match the stabilisation distance of the flame without NRP discharges experimentally and numerically. Appendix D explains how this shift in axial position has been corrected in order to allow comparison between numerical and experimental flame positions. Except for the parameter that is explicitly changed in the simulations (so as to evaluate its influence on the sta-

bilisation position of the flame), the values of the input parameters are taken so as to match the experimental conditions:

- Pressure: $p = 1\,\text{atm}$
- Fresh gas temperature: $T_\text{u} = 293\,\text{K}$
- Cooled plate temperature: $T_\text{cp} = 393\,\text{K}$; this value is only estimated, but the sensitivity analysis in Appendix D showed that the stabilisation position of the flame is not strongly dependent on it (see Figure D.2(b))
- Fresh gas velocity: $u_z = 0.8\,\text{m.s}^{-1}$ (see Appendix D for justification of this value)
- Equivalence ratio: $\Phi = 0.8$
- Ozone concentration without NRP discharges: $[O_3] = 0\,\text{ppm}$
- Nozzle-plate distance: $Z = 7.8\,\text{mm}$

Appendix D provides a sensitivity analysis for the position of the flame, the laminar flame speed, and the adiabatic flame temperature as a function of these input parameters.

The stabilisation position of the centre of the flame is a linear function of the temperature of the fresh gases and of their ozone content. Figure 4.22 displays the fact that the maximum flame displacement in its centre (measured as $\Delta z_0 = 0.7\,\text{mm}$, see Figure 4.16) is equivalent to an increase in the unburnt gas temperature of 47 K and in the ozone content in the fresh gas of 15,000 ppm. This corresponds to an energy per pulse, E_p, of $0.43\,\mu\text{J}$ for the chemical scenario presented in Section 4.4.2.2 and an energy of $0.85\,\mu\text{J}$ for the thermal scenario presented in Section 4.4.2.1. Thus, the energy required for a given displacement of the flame by ozone generation is approximately half the amount of energy needed to obtain the same flame displacement by heating of the unburnt gas. These estimates for the deposited energy are smaller than the energy determined from the voltage-current measurements (see Figure 3.12).

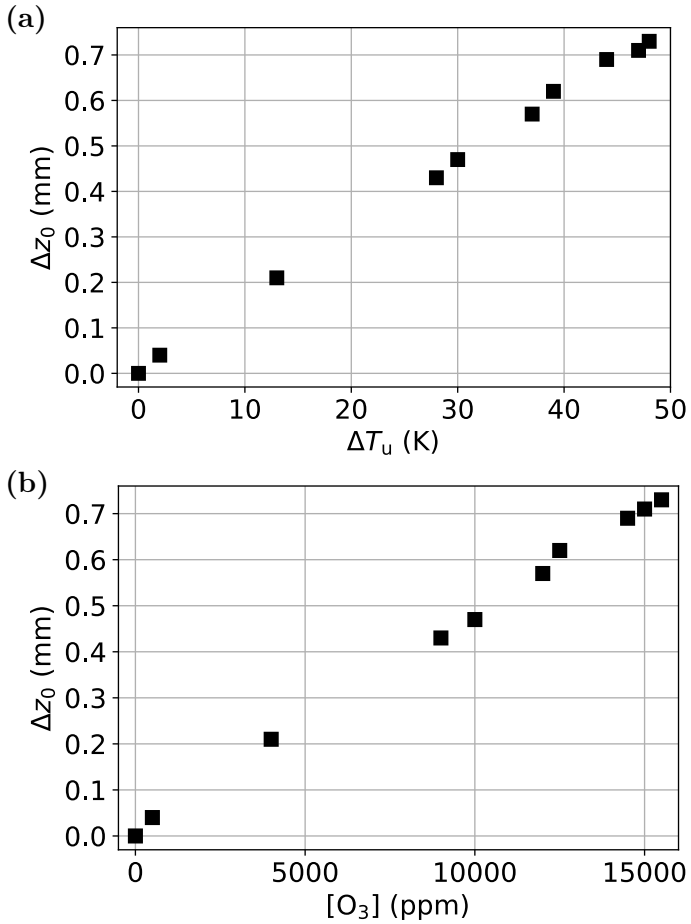

Figure 4.22: *Increase in (a) unburnt gas temperature, ΔT_u, and (b) ozone concentration in the fresh gas mixture, $[O_3]$, used to match the experimental flame displacement, Δz_0, from Figure 4.16. Initial parameters for the computation are: atmospheric pressure ($p = 1\,atm$), ambient gas temperature ($T_u = 293\,K$), stagnation plate temperature, T_{cp}, of 393 K, fresh gas velocity, u_z, of $0.8\,m.s^{-1}$, distance between burner nozzle and stagnation plate, Z, of 7.8 mm, and methane-air equivalence ratio, Φ, of 0.8.*

4.4.3.2 Influence of the NRP discharge power on the laminar flame speed enhancement and the adiabatic flame temperature increase

The laminar flame speed is defined as the speed at which an adiabatic unstretched laminar flame propagates through an unburnt gas mixture. The computed position of the flame changes following ozone or heat addition to the fresh gas. The velocity of the gases at the position where the OH concentration is maximum is considered as the speed of the flame.

The laminar flame speed without application of NRP discharges is estimated at 26.8 cm.s^{-1}. Simultaneously to the laminar flame speed, the adiabatic flame temperature for each case is determined as the maximum temperature on the computational domain.

Figure 4.23 presents the enhancements of (a) the laminar flame speed, $\Delta S_L/S_L$, and (b) the adiabatic flame temperature, $\Delta T_{ad}/T_{ad}$, calculated with the inlet parameters of fresh gas temperature and ozone content from Figure 4.22. The values are expressed as a function of the plasma discharge mean power, P_p, which has been deduced from the ozone production and unburnt gas temperature increase from Figure 4.22.

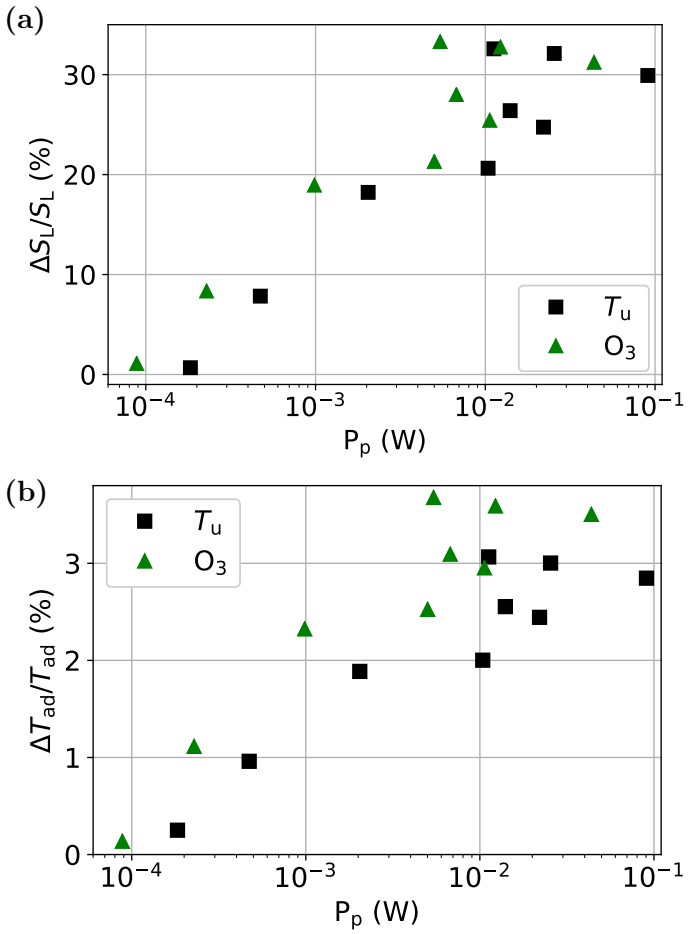

Figure 4.23: *Enhancements of (a) laminar flame speed, $\Delta S_L/S_L$, and (b) adiabatic flame temperature, $\Delta T_{ad}/T_{ad}$, as a function of the mean power of the NRP discharges, P_p, applied to the flame. These enhancements are generated either by a computed increase in the fresh gas temperature, T_u (black squares), or in the ozone content, O_3 (green triangles).*

The flame speed enhancement reaches a maximum value of 35 %. As expected, the laminar flame speed enhancement deduced from the flame displacement is the same whether the energy is deposited in the form of heat (increase in the fresh gas temperature), or if it is used to modify the chemistry of the fresh gas (ozone added in the unburnt gas mixture). The difference lies in the discharge powers required to generate ozone concentration or fresh gas temperature increase: the energy required for a given increase in the laminar flame speed is lower when it is used for ozone production rather than for fresh gas temperature increase.

The two trends of Figure 4.23(a) (high sensitivity of flame speed to power for low discharge power, then saturation of the enhancement) are also observed in Figure 4.4. The energies measured by means of the current and voltage probes have similar values in Sections 4.3 and 4.4. A comparison of the flame speed enhancements shows that the maximum enhancement for the configuration from Section 4.3—about 30 %— is much higher than the maximum enhancement yielded by the configuration from Section 4.2, which is 2.2 %. An explanation for the different enhancement values is linked to the electrode configuration: in Section 4.2, the electrodes are oriented so as to generate an electromagnetic field parallel to the flame front. In Section 4.3, the electromagnetic field is perpendicular to the flame and, moreover, all the field lines cross the flame front. Since the flame is a plasma itself, constituted of electrons and ions, it is also influenced by the orientation of the electromagnetic field generated by the NRP discharge. However, effects such as ionic wind can be ruled out due to the short duration of the applied electric field (which is applied less than 0.03 % of the time).

The adiabatic flame temperature enhancement follows the same trend as the laminar flame speed, but its value is much lower, reaching a maximum of 4 % in the considered range of NRP discharge power. The adiabatic flame temperature increase caused by ozone addition in the fresh gas (green triangles) is slightly higher than the adiabatic temperature increase from fresh gas heating (black squares), though this difference reaches a maximum of only 0.6 %, which corresponds to 1 K difference between the two adiabatic flame temperatures for a given discharge power. Practically, such a difference could be neglected.

As displayed in Figure 4.16, the central area of the flame is displaced more than its edge, resulting into a increase in the flame's surface. This difference in displacement is linked to the fact that the NRP discharges are applied in the centre of the flame only. The flame speed enhancement is estimated from the displacement of the flame in its centre, meaning that only a local value, representing the maximum flame speed enhancement over the surface of the flame, is here taken into account for the estimation of laminar flame speed enhancement.

The overall enhancement of the flame is much harder to quantify—and would require two-dimensional axisymmetric simulations.

4.5 Conclusion

The visualisation of a flame subjected to NRP corona discharges parallel to the flame front has been realised in Section 4.2 and brought to light an influence of the discharges on the stabilisation position of the flame: when the NRP discharges were activated, an upstream displacement of the flame towards the electrodes was observed. On the basis of the conical shape of the quartz tube used to confine the flame, the displacement of the flame has been quantitatively linked to an increase in its burning velocity. An enhancement of up to 2.2 % of the laminar flame speed was deduced, for a mean electrical power input of the NRP discharges estimated at 0.5 % of the flame thermal power.

As well as demonstrating an effect of the flame on the topology of NRP discharges in Section 3.2, the experiments in Section 4.2 have also allowed to display an influence of the NRP discharges on the flame. This effect of the NRP discharges on the flame, and the opposite effect of the flame on NRP discharges confirms the fact that the relation between NRP discharges and flame is not only an effect of the former on the latter, but rather an interaction between the two of them. Nevertheless, the fact that the flame required an acoustic forcing to mitigate the inherent Darrieus-Landau instability, as well as the presence of the quartz walls make it a complex configuration.

In Section 4.3, NRP corona discharges pulsed in a transverse direction compared to a laminar premixed stagnation flame were considered. First, in Section 4.3.1, the transient response of laminar premixed flames to application of NRP corona discharges was studied. A model for the temporal evolution of flame displacement as a function of the flame speed enhancement was developed and used to fit the experimental data, thus yielding experimentally determined flame speed enhancements ranging from 4 to 9 %. However, throughout the experiments from Section 4.3.1, the flame was attached to the burner's nozzle; thus this configuration is not comparable to numerical simulations. In Section 4.3.2, the steady-state effect of NRP discharges on laminar premixed stagnation flames was studied, in a configuration where the flames were detached from the burner's nozzle. Application of high-voltage pulses between the electrodes led to an upstream displacement of the flame (towards the high-voltage electrode). This displacement was analysed as a function of the mean power of the discharges and, from the displacements obtained in the experiments, the flame speed enhancement was deduced. The analysis of flame speed

enhancement as a function of the NRP discharge power allowed to display the existence of two regions. In the first one, corresponding to discharge powers between 0 and 0.5 W, the laminar flame speed evolves linearly with the discharge power and is highly sensible to this parameter. In the second region, for electrical powers higher than 0.5 W, the laminar flame speed is less sensitive to the discharge power and reaches a maximum value of up to 30 % of the initial flame speed.

Finally, Section 4.4 has been dedicated to the development of a numerical model in order to estimate the chemical and thermal effects of NRP corona discharges and their impact on a laminar premixed methane-air stagnation flame by considering, on the one hand, a purely thermal effect of the discharges, and, on the other hand, a purely chemical effect, through the production of ozone. The simplified model shows, for low increase of the temperature, that a greater effect of the chemical scenario is to be expected. Even at the low deposited energies considered, an increase of up to 25 % in the laminar flame speed was obtained with 10,000 ppm of ozone addition. The thermal enhancement of the laminar flame speed for the same plasma energy is 7 % only. The adiabatic temperature increase of the flame follows a trend similar to the flame speed enhancement but is less significant. The flame speed enhancement is similar to the values determined in the experimental study in Section 4.3, although the experimental values for the energy deposited by the NRP discharges are two orders of magnitude higher than the ones considered in the model.

Chapter 5

Conclusion and outlook

5.1 Contributions of this thesis

In this work, Nanosecond Repetitively Pulsed plasma discharges were generated in atmospheric conditions (1 atm and 300 K) in different electrode configurations. These NRP discharges had pulse durations of 10 ns, voltage amplitudes up to 15 kV and Pulse Repetition Frequencies (PRF) up to 30 kHz and were generated either in air or in ignitable mixtures of methane and air.

The introduction mentions the need for more investigations regarding the interactions taking place between flows and NRP discharges, especially the effect of these flows on the discharges. This literature review also addressed the lack of information regarding the mechanism of plasma-induced enhancement of the flame and vice versa.

The interactions of NRP discharges with the laminar flow were studied; the investigations and the resulting findings are summarized as follows:

Effect of an air flow on NRP discharges

NRP plasma discharges were generated between a pin high-voltage electrode and an annular ground, with a laminar swirled flow of air transversal to the inter-electrode area. The use of a steady-state air flow between the electrodes has allowed to display the transition voltage between the NRP corona and NRP spark regime as being a function of the transverse air velocity, while the

azimuthal part of the air flow had no influence on these regime transitions. This experiment also highlighted the existence of an hysteresis between the NRP corona-to-spark and the NRP spark-to-corona transitions.

Modification of the amplitude and frequency of a sine acoustic forcing of the air in the inter-electrode area allowed to reach either a corona-to-spark, or a spark-to-corona regime transition. A map of existence of the two regimes of NRP discharges as a function of the acoustic frequency and the relative velocity amplitude of the forcing was established. Analysis and use of non-dimensional numbers enabled to attribute this effect of air flow on NRP discharge regime to a modification in the number of applied high-voltage pulses on each air particle during their transit in the inter-electrode area. The higher this number of applied pulses, the closer the NRP corona discharges find themselves from transiting to the NRP spark regime. Modelling the air flow influence on the total power applied to an air particle during its transit in the inter-electrode area reproduces the trends of the experimental results, thus validating the explanation for the observed NRP regime transitions.

Effect of a laminar premixed flame on NRP discharges

Two different burners were used in the second part of this study. In the first one, the NRP discharges were pulsed in a direction parallel to a laminar premixed methane-air flame. Influence of the proximity of the flame to the discharges was demonstrated by the effect of the flame on the visual aspect of the discharges. When the electrodes-flame distance was sufficiently small, transition of the NRP corona discharges to the NRP spark discharges was observed.

A second burner was used, in which the NRP corona discharges were pulsed perpendicularly to the flame front of a laminar premixed methane-air stagnation flame. First, the influence of the mixture composition was assessed: the visual aspect of the NRP corona discharges was compared in an air flow and in a methane-air flow. The significant difference in the resulting discharges, as well as their slightly higher energy in the second composition, proved the inter-electrode mixture to play a significant role on the NRP discharges characteristics. This influence was caused by a modification in the spectroscopic properties of the inter-electrode gas due to the methane addition. Ignition of the reactive mixture allowed stabilisation of a stagnation flame in the inter-electrode area. The presence of this flame led to an increased length of the NRP corona discharges compared to the case without flame.

In these two experimental configurations, the influence of the flame was attributed first to the lower density resulting from the high gas temperature close

to the flame front, where the reduced electric field was thus locally enhanced, and second to the interaction between the electromagnetic field generated between the electrodes and the charged species in the flame.

Effect of NRP discharges on a laminar premixed flame

The influence of NRP corona discharges on a laminar premixed methane-air flame was assessed experimentally in two different experimental configurations. The assumption for this effect was validated by developing a numerical model for the estimation of the plasma production of heat and active species (limited to ozone).

In the first experimental configuration, the NRP discharges were pulsed in a direction parallel to the flame front. The discharges induced the flame to move as a whole in the upstream direction. The increase in laminar flame speed under application of NRP discharges was deduced from the flame displacement and quantified as a function of the mean power of the NRP corona discharges. This allowed to estimate a maximum flame speed enhancement of 2.2 % when the plasma-to-flame power ratio was 0.5 %. For low NRP powers, the flame speed enhancement was thrice as sensible to the NRP power than at high power values.

The second configuration considered NRP corona discharges perpendicular to the leading edge of a stagnation flame. In a first setup, the transient response of laminar premixed stagnation flames to NRP corona discharges was studied and a model developed in order to evaluate the flame speed enhancement resulting from the effect of plasma discharges. This model yielded flame speed enhancements from 4 up to 9 % of the initial flame speed. In the second setup, a steady-state influence of NRP discharges on laminar premixed flames detached from the nozzle was observed. The electrical-to-thermal ratio was higher than in the previous settings, up to 2 %. As with the two previous setups, application of NRP discharges caused an upstream displacement of the flame as a whole, as well as a deformation of the flame front's surface, thus indicating a non-homogeneous distribution of the plasma energy inside the flame front. The flame speed enhancement has been quantified thanks to the displacement of the flame's central part under application of NRP discharges and estimated as reaching a maximum value of 40 %. Analysis of the flame speed enhancement as a function of the mean power of the NRP discharges highlighted, like in the previous configuration, the existence of a high- and a low-sensitivity area of the flame speed enhancement to the plasma power.

A hypothesis for the observed phenomenon was the production of heat and a

pool of active species by the plasma discharges. Development of a numerical model for the heat production and the chemical production (considering ozone alone) and their effect on the laminar flame speed enhancement allowed to validate the plasma production of heat and ozone as a likely cause for the observed effect of NRP discharges on the flame.

5.2 Perspectives and future work

This work has provided insight on the interaction mechanisms occurring between NRP discharges and laminar reactive flows. Yet it also brought to light a certain number of questions and recommendations for useful future work in this research field.

The first item on this list of future work concerns the observed effect of flow on NRP discharges and its explanation based on gas residence time between the electrodes and the discharge mean power. While the qualitative relation between these parameters and the regime transition of NRP discharges has been modelled, it remains to determine the domains of existence for the NRP corona and the NRP spark regimes quantitatively. The influence of the voltage amplitude on the regimes of NRP discharges would also need to be included in such a predictive model. The NRP discharges have been implemented in a setup with a specific set of parameters (atmospheric pressure, ambient temperature, laminar flow, gap distance in the order of one centimetre). The implemented system would need to be scaled up if the NRP discharges were to be used in bigger-dimensioned systems (in gas turbines for instance), or under different reactive flow conditions.

The influence of a flame's proximity to the NRP discharges has been attributed to two different effects: first was the increase in local reduced electric field close to the low-density combustion gases. The second effect of the flame on the NRP discharges was the interaction of the charged species in the flame with the discharges. The influence of the electrode configuration and its orientation (parallel or perpendicular) and distance to the flame could be modelled in order to determine an optimal setup to yield a maximum influence of the discharges on the flame.

The effect of NRP discharges on a flame has been assessed experimentally and its origin investigated numerically. Many questions still remain to be answered and optimisation to be done in the experimental study. Foremost, there is a need for an improvement in the method for energy determination. Indeed, while the current methodology for energy measurement allows for low levels

of uncertainty (about $30\,\mu$J.pulse^{-1}), the range of energies measured in the NRP corona and glow regimes is nevertheless in the same order of magnitude, resulting in a poor confidence in the given values of deposited energy per pulse (and the mean power of the NRP discharges calculated from them). Moreover, the understanding as to the proportion of NRP corona discharges energy going to heat and the proportion going to the chemical production of active species are needed.

A numerical model has been developed in order to establish the production of heat and active species (limited to ozone) by the NRP discharges. The results yielded by this model should be verified by experimental measurements. Quantitative information as to the concentration of the chemical species produced by NRP discharges could be deduced from optical emission spectroscopy, absorption spectroscopy, or a gas analyser, depending on the species investigated. These experimental results could serve as a basis to improve the numerical model: by including new, long-lived species to it, the chemical effect of the NRP discharges could be predicted in a more precise manner. Top on the list of species to take into consideration are NOx, which are known to be crucial species in the combustion process, as pollutants as well as potential enhancing agents of the laminar flame speed. Finally, the experiments proved that the NRP corona discharges energy was distributed in an non-homogeneous manner across the surface of the flame. This non-homogeneous energy distribution resulted in a deformation of the flame when NRP discharges were applied in its central part. This deformation phenomenon cannot be taken into account by mere one-dimensional simulations, prompting the need for two-dimensional simulations which would aim, first, at estimating the energy distribution over the flame's surface and, second, to capture this effect of flame deformation. In order to include this phenomenon in the computations, the numerical model for plasma-produced heat and active species would have to take into account the two-dimensional nature of the problem as well, by estimation and inclusion of radial diffusion of heat and species.

This study focused on interactions between flow and plasma, and between combustion and plasma. In fact, in industrial applications, a much more complex, trilateral, interaction between flow, combustion and plasma would take place. Now that the individual effects and interactions are identified and known, it remains to combine them in order to apply this theory to setups closer in design to actual combustion chambers.

Appendix A

Characterisation of NRP plasma discharges

Throughout all experiments, the energy per pulse of the NRP discharges has been determined. This appendix presents the methodology for determination of the deposited energy per pulse of the nanosecond discharges. NRP corona and glow discharges are considered first, followed by NRP spark discharges.

The plasma discharges are pulsed with a high-voltage pulse generator (FPG Series, FID Technologies). All measurements throughout this work are performed with equipment of similar characteristics: a current probe (model 6585, Pearson Electronics) equipped with an attenuator (model 2-20, Barth Electronics), a voltage probe linked to high-voltage and ground (PPE 20 kV, LeCroy). These two probes are linked to an oscilloscope (1 GHz or more, Agilent Technologies) with a sampling rate between 10 and 20 GHz. The high-voltage probe is linked to a 1 MΩ impedance input of the oscilloscope and the current probe to a 50 Ω impedance input.

Figure A.1 presents a typical pulse measurement obtained for an NRP discharge, where the voltage amplitude, U, and the current, I, are presented as a function of time, t. The maximum voltage is 11 kV, the maximum current is 10 A and the PRF is 25 kHz. The gap distance separating the two pin electrodes is 12 mm and the signals are averaged over 1,000 pulses.

The signals of Figure A.1 have been acquired with separate probes. Although each probe was linked to the same oscilloscope, the electrical circuit for the two of them differs, inducing a difference of transition time from the measurement point (at the experimental setup) to the acquisition point (at the oscilloscope's

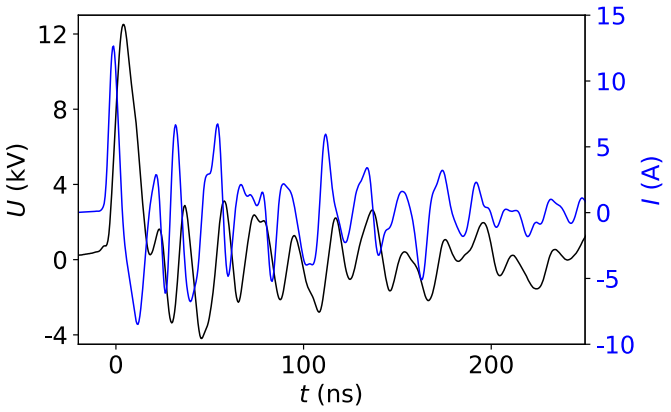

Figure A.1: *Example of voltage and current waveforms for a pulse of an NRP corona discharge between two pin electrodes separated by a gap of 12 mm, with a transversal air and methane flow velocity of 1.20 m.s^{-1} and equivalence ratio of 0.8. The PRF is set to 25 kHz, the maximum voltage amplitude, U (black line), is 11 kV and the maximum current, I (blue line), is 10 A. The measurements are averaged over 1,000 pulses.*

input). This means the voltage and current signals are impaired with a deskew in time. This deskew is determined and removed by assuming the setup of the two electrodes and the high-voltage pulse source to constitute a capacitive circuit. Under this hypothesis, the measured current without discharge is a purely capacitive current, also called displacement current, I_{disp}:

$$I_{\text{disp}} = C \times \frac{dU}{dt}. \tag{A.1}$$

The derivative dU/dt is determined from the voltage signal for a high-voltage pulse without discharge by taking the derivative with respect to time. The circuit's equivalent capacity, C, is determined by dividing the current without discharge, I_{disp}, by dU/dt; in other words, the capacitance was chosen so as to scale the calculated displacement current I_{disp} to the same maximum value as the measured current I_{total}. Numerical application with the data of Chapter 4 yields a capacitance of 6 pF, a value that coincides with the ones given by Pai (2008) for similar discharges in the NRP diffuse and filamentary regime. This obtained capacitive current is considered constant in all the measurements that follow, as long as the configuration (gap distance, applied voltage) remains the same.

The current being assumed as entirely capacitive in the case without discharge, the signals of capacitive current and measured current are compared and synchronised, giving the information of the deskew between the current and voltage acquisition. Figure A.2 shows the deskew determination for current and voltage

signals acquired in the configuration of Figure A.1.

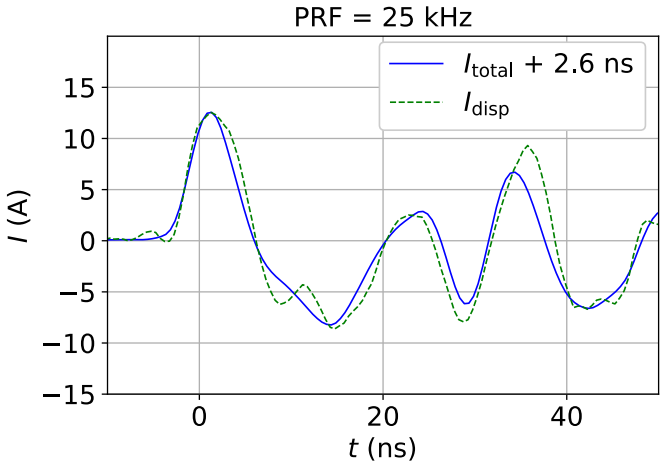

Figure A.2: *Determination of the deskew between current and voltage acquisition, for measurements in the experimental conditions from Figure A.1: the current waveform, I_{total}, (solid blue line) is moved 2.6 ns backwards in time in order to adjust it to the displacement current, I_{disp}, (dashed green line); these 2.6 ns correspond to the deskew.*

The deskew of 2.6 ns found in this example is in the range of typical values (between 2 and 5 ns).

Once the deskew is known, it is applied to the signals measured with a discharge between the electrodes. After synchronisation, the total (measured) current, I_{total}, is decomposed into its capacitive component, I_{disp}, and its conductive component, I_{cond}, as follows:

$$I_{total} = I_{disp} + I_{cond}, \tag{A.2}$$

where the capacitive part of the current, I_{disp}, has been determined previously in the measurements without discharge (see Figure A.2). Figure A.3 gives an example of the decomposition into total, displacement and conductive currents for the experimental conditions of Figure A.1.

As mentioned earlier, the capacitive current becomes negligible compared to the conductive current when the discharges are in the NRP spark regime. This is because the spark discharges consist in a channel that forms between the electrodes. This channel is electrically conductive, thus allowing a high transport of electrons from the ground electrode (cathode) to the high-voltage electrode (anode).

Although it is the case when the NRP discharges are in the spark regime, the displacement part of the current is far from negligible compared to its conductive component in the NRP corona and glow regimes. Since this conductive

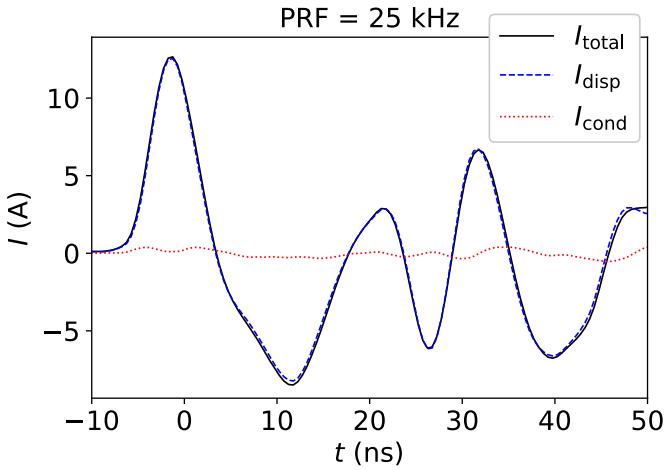

Figure A.3: *Decomposition of the total current, I_{total} (solid black line), into displacement current, I_{disp} (dashed blue line), and conductive current, I_{cond} (dotted red line), for the NRP corona discharges presented in Figure A.1.*

current corresponds to the actual current flowing between the electrodes, it is this component of the current which is used in order to determine the evolution of the instantaneous power, P, of the NRP discharges:

$$P(t) = U(t) \times I_{\text{cond}}(t), \tag{A.3}$$

and deduce the deposited energy per pulse, E_{p}:

$$E_{\text{p}} = \int_t P(t)dt. \tag{A.4}$$

From this deposited energy per pulse, the parasitic energy from the electrical circuit, taken as the energy per pulse obtained for the case without discharge, is subtracted. An example of temporal evolution of the deposited energy per pulse and the instantaneous power is given in Figure A.4, where the experimental conditions are the same as in Figure A.3.

Each energy measurement has been repeated thrice, and the standard deviation of the results yields an uncertainty in the energy measurements of 30 μJ.pulse^{-1}. A sensibility study on the time deskew between current and voltage has also been realised: the value of this deskew is modified from 0 to 10 ns and its influence on the obtained deposited energy is given in Figure A.5. The red line is the value that has been used to synchronise current and voltage signals.

The energy per pulse varies from 5 to 45 μJ.pulse^{-1} when the deskew is modified between 0 and 10 ns. Considering the position of the red line (corresponding

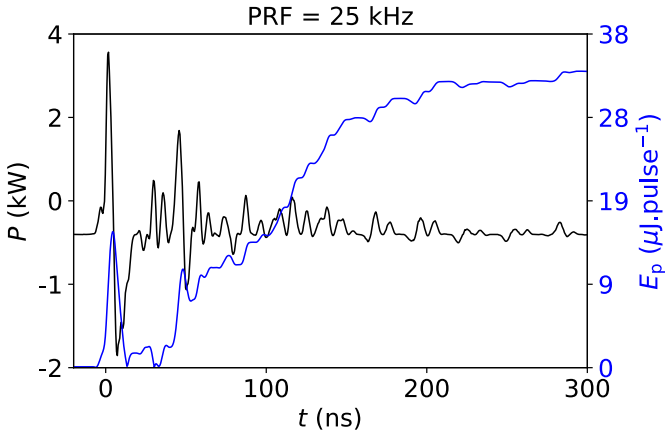

Figure A.4: *Temporal evolution of instantaneous power (black line) and deposited energy per pulse (blue line) of NRP corona discharges in the same conditions as in Figure A.3.*

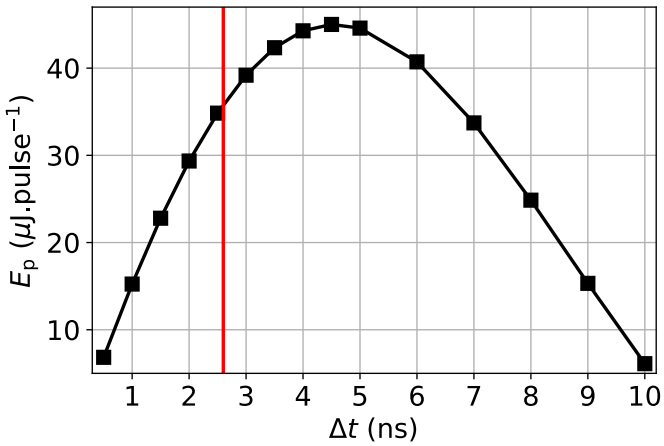

Figure A.5: *Deposited energy per pulse, E_p, as a function of the deskew applied between current and voltage signals, Δt. The red line is the value used in the study, 2.6 ns. The experimental data used for the energy determination correspond to the ones from Figure A.1.*

to the actual value of the deskew), it can be seen that if the uncertainty on the deskew is 0.5 ns, the uncertainty on the deposited energy is about 5 μJ.pulse^{-1}. This uncertainty on the deskew determination is considered as included in the total uncertainty on the energy measurements (30 μJ.pulse^{-1}).

Appendix B

Hot wire calibration procedure

The air flow velocity has been measured in Chapter 2 with a hot wire (55P16 from Dantec Dynamics) located in the plenum of the experimental setup. The velocity in the inter-electrode area has been deduced from this energy measurement by the principle of mass flow rate conservation between the plenum and the nozzle of the burner. Considering that there is no density modification of the air between these two locations, the conservation in mass flow rate implies conservation of volume flow rate. Thus the velocity at the nozzle's outlet is deduced by multiplying the velocity in the plenum by the ratio of surface area between these two sections.

Prior to the measurements in the setup, the hot wire needed to be calibrated on a calibration test-rig in the EM2C lab. This setup is presented in Figure B.1. A mass flow controller (EL-Flow from Bronkhorst) is set upstream of the setup and controls the volume flow rate of air, so that the velocity of air at the nozzle outlet is known. Due to the profile of the converging section in the test-rig, the velocity profile along the radial axis is uniform, as it is also supposed to be in Chapter 2. The uniform velocity profile, as well as the correct value of velocity at the nozzle, have been verified by means of PIV measurements.

The hot wire is linked to a power supply in order to heat up the thin tungsten wire at the end of the fork (see Figure B.1) at a constant temperature. When air flows past the heated wire, its temperature decreases, leading to an increase in the wire's electrical resistance. In order to maintain the temperature of the hot wire constant, the applied voltage is increased. Thus, the measured voltage increase is a function of the velocity of the gas.

Prior to installing a new hot wire into the setup, it required calibration on

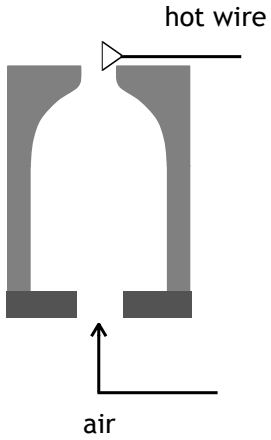

Figure B.1: *Setup for hot wire calibration*

the test-rig B.1. The velocity of the gas is increased with the flowmeters and the variation of voltage is deduced. Thus, a curve of voltage as a function of gas velocity is obtained and used in the experiments of Chapter 2 in order to obtain the air velocity as a function of the measured voltage. This relation is then fitted in order to simplify the determination of air velocity. An example of the obtained curve and its fitting is given in Figure B.2. The measured profile of air velocity as a function of the hot wire voltage (solid black line) is fitted with a polynomial function (dashed red line). The obtained function is the following one:

$$u_z = 22.93 \times U^3 - 74.06 \times U^2 + 79.65 \times U - 28.56, \tag{B.1}$$

where u_z is the velocity in $\mathrm{m.s^{-1}}$ and U is the voltage applied to the hot wire in V. The measurement of voltage as a function of air velocity has been performed thrice and the uncertainty was found to be smaller than 0.5 % of the measured voltage value, corresponding to an uncertainty of about $0.02\,\mathrm{m.s^{-1}}$ in the velocity range $[0; 14]\,\mathrm{m.s^{-1}}$.

It is important to note that since the hot wire provides only the velocity magnitude in the plane perpendicular to the wire, the sign of the velocity had to be adjusted when the local velocity had a negative value, as in Figure 2.3(b), where the local azimuthal velocity along the axis was measured as positive, despite the fact that the velocity was negative on half the diameter. From the curve in Figure B.2, the voltage measured by the hot wire allows to deduce the velocity of the flowing gas.

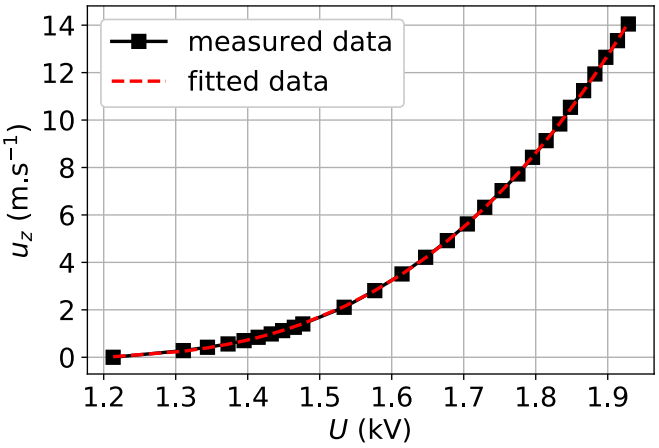

Figure B.2: *Example of hot wire calibration curve: the voltage given by the hot wire, U, is expressed as a function of the velocity at the nozzle's outlet, u_z (see Figure B.1).*

Appendix C

Determination of reaction rate constants with BOLSIG+

The chemical scenario of the numerical model presented in Part 4.4 makes use of four reactions, two of them (Equations (4.14) and (4.15)) of the initial collision of electrons with air molecules. These two initial reactions, (4.14) and (4.15) are crucial to the implemented model and the utmost care should be taken when handling the constants used in the reactions. While the reaction rate constants for reactions (4.16) and (4.17) are well documented in the literature (see Popov 2001; Ibraguimova et al. 2003; Ombrello et al. 2010b; Rusterholtz et al. 2013), the ones for electron-impact excitation of nitrogen (4.14) and electron-impact dissociation of oxygen (4.15) are not well known and rather hard to find in the literature. Due to their high dependence on the discharge conditions, the need arises to determine the reaction rate constants for these two reactions.

The BOLSIG+ code Hagelaar and Pitchford (2005) is a popular software designed to solve the Boltzmann equation. Assuming spatial uniformity of the electric field and collision probabilities, as well as a two term approximation to the Boltzmann equation in order to simplify it, the solver yields several useful output parameters. In order to determine the reaction rate constants for the reactions of interest, the input parameters are:

- reduced electric field, E/n
- gas temperature
- gas composition

- database of collision reactions

A range of reduced electric fields, relevant to our study, is considered; it ranges from 40 to 500 Td ($1\,\mathrm{Td} = 10^{-21}\,\mathrm{V.m^{-2}}$). The gas temperature is kept constant at 300 K and the gas composition is adjusted to the air molar composition (79 % nitrogen and 21 % oxygen). Six databases are compared: the Biagi database (Magboltz version 8.9, see Biagi 2010), the IST-Lisbon database (see Alves 2014), the Itikawa database (see Itikawa 2017), the Morgan database (Kinema Research and Software, see Morgan 2017), the Phelps database (see Phelps 2017) and the Triniti database (see Napartovich et al. 2017). All these databases are available online, on the LXCat website (see Pitchford et al. 2017).

A number of output parameters is obtained from this code; the ones that are relevant to our model are: the electron temperature, T_{e^-}, expressed in eV, and the reaction rate constants, k_{11} for reaction (4.14) and k_{12} for reaction (4.15), both expressed in $\mathrm{cm^3.mol^{-1}.s^{-1}}$. The obtained reaction rate constants, k_{11} and k_{12}, are compared for the range of reduced electric field, E/n mentioned above. The results are displayed in Figure C.1. In both cases, four of the six mechanisms agree well. The Biagi, Lisbon and Phelps mechanism yield similar reaction rates for the range of reduced electric field considered. The reaction rates have a very low value when the E/n value is smaller than 100 Td, then increase rapidly between 100 and 300 Td before nearing a saturation point around 500 Td. These very low values at low reduced electric fields have consequences on the production of ozone determined in Part 4.4 which is very small, below 100 Td.

As mentioned above, the BOLSIG+ solver also allows the determination of the mean electron temperature, T_{e^-}, as a function of the reduced electric field. Figure C.2 displays this evolution. These values of electron temperature are used in order to determine the deposited energy of the plasma discharges used in the model of Part 4.4.

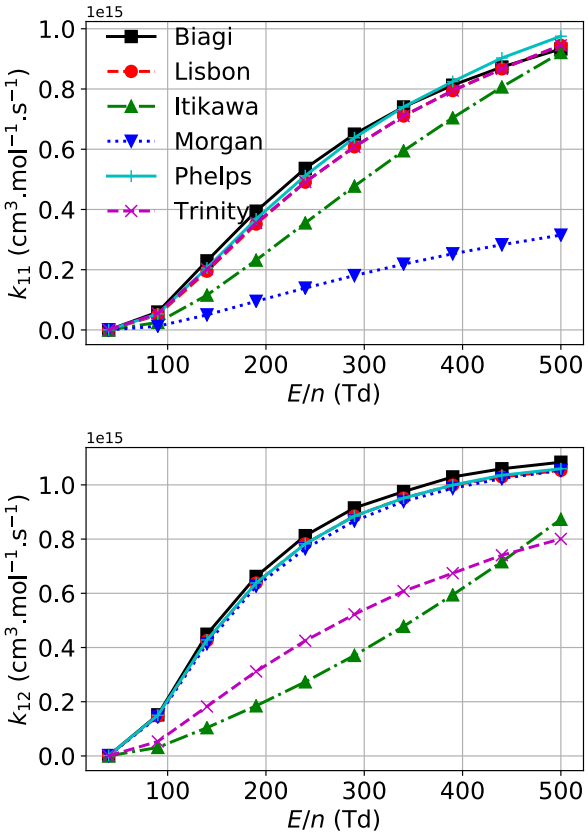

Figure C.1: *Reaction rate constants, k_{11} and k_{12}, for the reactions of nitrogen excitation (4.14) and oxygen dissociation (4.15), as a function of the reduced electric field, E/n, for the six compared mechanisms.*

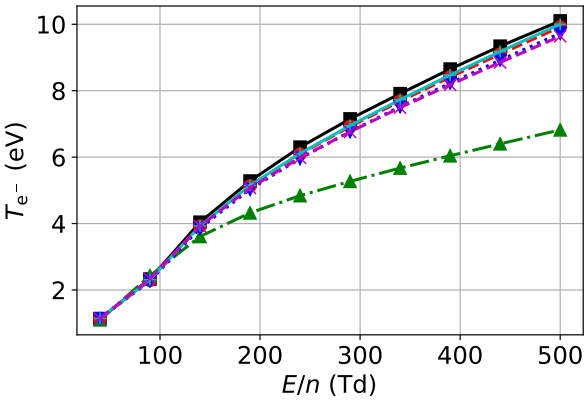

Figure C.2: *Electron temperature, T_{e^-}, evolution as a function of the reduced electric field, E/n, for the six compared mechanisms.*

Appendix D

One-dimensional simulations of a stagnation flame and sensitivity analysis

In Chapter 4, numerical simulations are performed in order to evaluate the influence of NRP discharges on a laminar premixed methane-air stagnation flame. These simulations use the Cantera software package (see Goodwin et al. 2017) with a Python input script. The script used is presented below. Several input parameters, such as boundary conditions, are given and a gas object is created according to the GRI-Mech 3.0 (see Smith et al.). From this gas, a stagnation flame object in a strained flow field is defined. The determination of the equilibrium concentrations and flow field provides a solution, first without, then with the energy equation. The grid is refined throughout the solution process in order to remove the unnecessary grid points and refine the grid close to the newly determined position of the flame.

The script, partly modified from the one called stagnation_flame.py, available on the Cantera website, is given here:

```
import cantera as ct
import numpy as np

# parameter values
p = ct.one_atm                  # pressure [Pa]
Tu = 293                        # unburnt gas temperature [K]
Tcp = 393                       # plate temperature [K]
Phi = 0.8                       # equivalence ratio
uz = 0.80                       # inlet velocity [m.s-1]
```

```
Z = 7.8E-03                 # domain size [m]
initial_grid = np.linspace(0, Z, 201)

mechanism = 'gri30' # reaction mechanism
comp = 'CH4:' + str(Phi) + ',O2:2,N2:7.52' # fresh gas composition

tol_ss = [1.0e-5, 1.0e-13]
tol_ts = [1.0e-4, 1.0e-9]
loglevel = 1
refine_grid = True

# grid refinement parameters
ratio = 3
slope = 0.1
curve = 0.2
prune = 0.06

# creation of the gas object
gas = ct.Solution(mechanism + '.cti')

# set state of gas to unburnt gas conditions
gas.TPX = Tu, p, comp
mdot = gas.density * uz

# creation of the stagnation flow object with a non-reactive surface
sim = ct.ImpingingJet(gas = gas, grid = initial_grid)

# mass flow rate at the inlet
sim.inlet.mdot = mdot

# surface temperature of the cooled plate
sim.surface.T = Tcp

sim.flame.set_steady_tolerances(default = tol_ss)
sim.flame.set_transient_tolerances(default = tol_ts)
sim.set_grid_min(1e-4)
sim.energy_enabled = False

sim.set_initial_guess(products = 'equil')
sim.show_solution()

sim.solve(loglevel, refine_grid)

# grid refinement, activation of energy equation and solving
```

```
sim.set_refine_criteria(ratio=ratio,slope=slope,
curve=curve,prune=prune)
sim.energy_enabled = True
sim.solve(loglevel, refine_grid)
sim.save(mechanism + '_mix.xml', 'energy', 'methane')
data_path = 'Phi_' + str(Phi)
sim.write_csv(data_path + '.csv', quiet = False)
print('finished solution with mechanism: ' + mechanism)

sim.show_stats()
```

The spatial evolution of several output parameters (such as gas temperature, density or species concentrations) is obtained. Typical profiles for these output parameters are provided in Figure D.1 where z is the coordinate on the axis, u_z is the gas velocity, T is the gas temperature and ρ is the density of the gas. The position $z = 0$ corresponds to the nozzle of the burner (where the inlet conditions for the simulation are defined) and $z = 7.74\,\text{mm}$ is the position of the constant temperature plate. The input parameters are the same that are given in the script presented above.

The velocity decreases downstream of the burner nozzle. Close to the flame, the higher temperature induces a density decrease, thus increasing the gas velocity. The velocity increases first but then decreases to zero at the stagnation plate (where the boundary condition on the velocity is $0\,\text{m.s}^{-1}$). The temperature is constant (at the value given as inlet condition, here 293 K) until the gases are close to the flame front. There, the temperature increases up to about 1,900 K, then decreases again because of the imposed temperature at the plate. Since the pressure is constant, the density profile follows an inverted trend compared to the temperature: from an initial value of $1.2\,\text{kg.m}^{-3}$, it decreases to $0.2\,\text{kg.m}^{-3}$ where the gas temperature is at its maximum. This decrease in density of the gas is also mentioned in Chapter 3 where the influence of a flame on NRP corona discharges is explained as linked to a decrease in the density of the gas close to the flame, thus increasing the local reduced electric field. The oxygen and methane concentrations decrease sharply at the flame front (at $z = 4.7\,\text{mm}$). Due to the lean mixture ($\Phi = 0.8$), the methane is entirely consumed while 20 % of the oxygen remains in the burnt gas. As methane and oxygen are consumed, the combustion products carbon dioxide and water are produced. The reaction of methane and oxygen produces several intermediate species which are themselves reacting into other species. OH and CH are two of them and their peak concentration can be used as a tracer for the flame front position. From the relative position of the two peaks, it can be seen that the CH concentration peak is located $380\,\mu\text{m}$ upstream of the OH concentration peak.

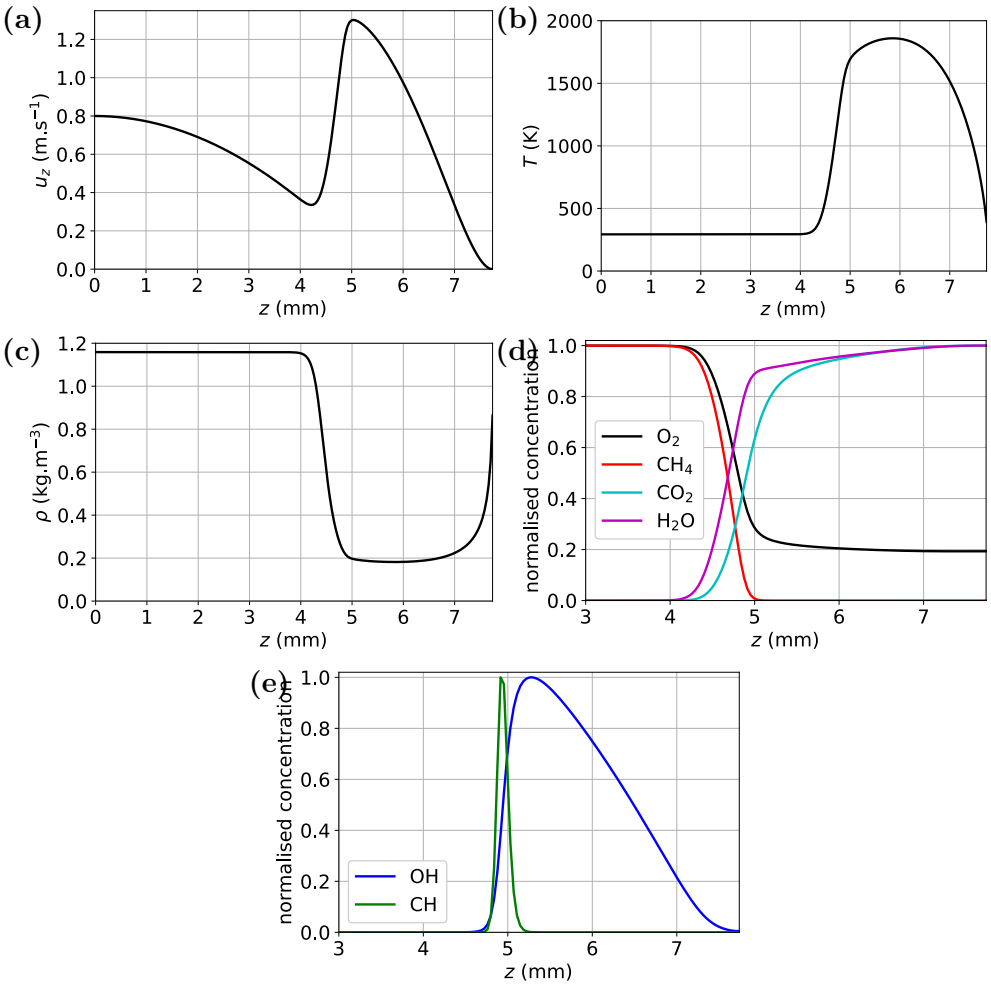

Figure D.1: *Output parameters obtained by computation of the one-dimensional stagnation flame: (a) gas velocity, u_z, (b) temperature, T, (c) and (d) normalised concentrations of species: reactants O_2 and CH_4, intermediate species: OH and CH, and products: CO_2 and H_2O.*

The sensitivity of the results to the input parameters is analysed in terms of three outputs: the displacement of the flame, Δz_0, the laminar flame speed enhancement, $\Delta S_\mathrm{L}/S_\mathrm{L}$, and the flame temperature enhancement, $\Delta T/T$, compared to the reference case whose input parameters are given below. As mentioned in Section 4.4.3, the position of the numerical flame is considered as being the axial position where the OH concentration reaches its peak value. The obtained velocity provides a good estimation for the laminar flame speed under these conditions (3 % discrepancy from the laminar flame speed yielded by computation of a freely-propagating flame). The maximum flame temperature for one set of input parameters is taken as the maximum temperature

reached in the nozzle-to-plate domain.

The input parameters in this sensitivity study are the following: fresh gas temperature, T_{u}, stagnation plate temperature, T_{cp}, equivalence ratio of the methane-air mixture, Φ, domain size, Z, and axial gas velocity, u_z. These input parameters are varied around the nominal values of the experiments and their influence on the flame position, flame speed and temperature observed. Figure D.2 presents the influence of the input parameters listed above on the flame position. With the exception of the parameters explicitly modified, the other parameters take the following values: $p = 1\,\mathrm{atm}$, $T_{\mathrm{u}} = 293\,\mathrm{K}$, $T_{\mathrm{cp}} = 393\,\mathrm{K}$, $\Phi = 0.8$, $u_z = 0.8\,\mathrm{m.s^{-1}}$, $Z = 8\,\mathrm{mm}$. The reference flame position, flame speed and temperature (with which the displacement and enhancements are determined) has these input parameters.

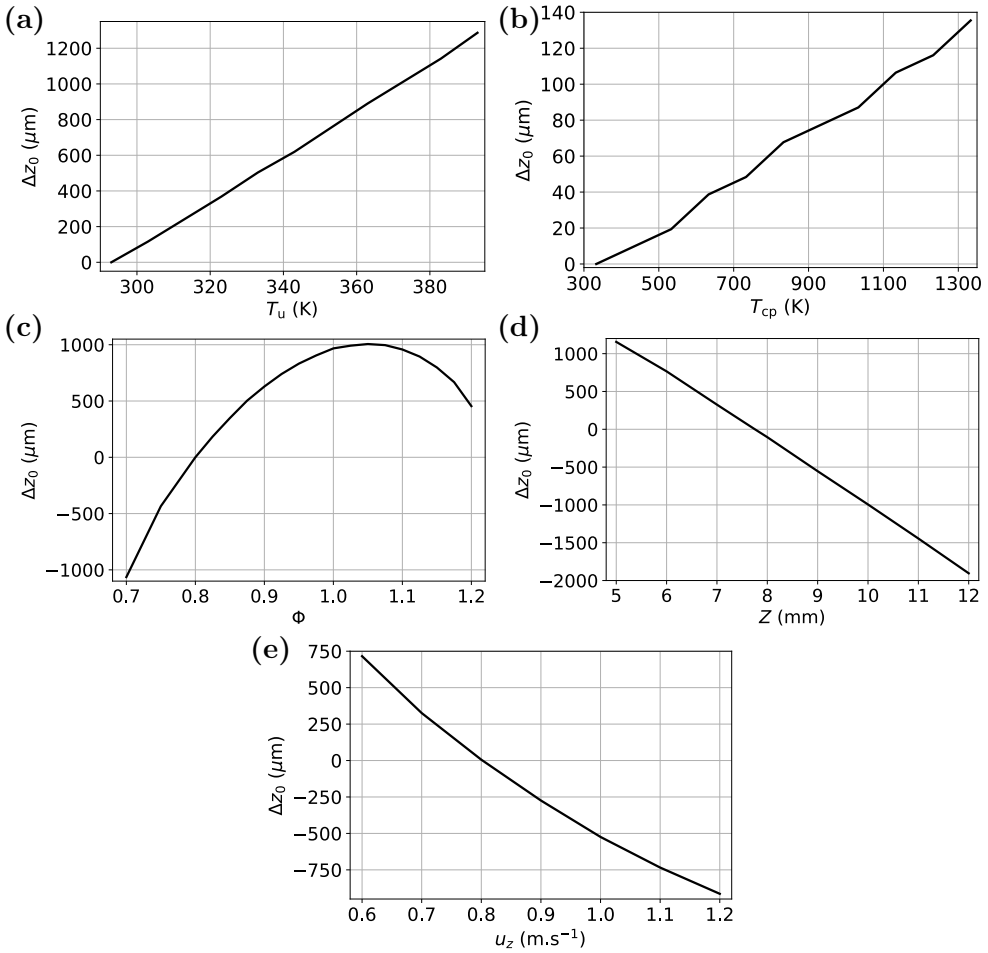

Figure D.2: *Influence of simulation input parameters on the displacement of the flame, Δz_0, determined from the maximum of OH concentration on the computational domain.*

The parameters with the highest influence are the unburnt gas temperature (see Figure D.2(a)) and the equivalence ratio (see Figure D.2(c)). The displacement in the considered range reaches a maximum of 1.2 mm. The flame moves linearly upstream with the fresh gas temperature. When the equivalence ratio is increased, the flame moves upstream until a maximum upstream position at $\Phi = 1.05$, then the flame starts moving downstream. The temperature of the cooled stagnation plate has almost no influence on the flame's position for the wide range of temperatures considered. The size of the domain influences the stabilisation position of the flame in a linear manner: when the distance between inlet of the domain and stagnation point (cooled plate) is increased, the flame moves in the downstream direction. Finally, increasing the speed of the inlet gas causes the flame to move downstream.

While the unburnt gas temperature and the equivalence ratio of the methane-air mixture have already been proved to have a significant effect on the laminar speed and the temperature of a laminar premixed flame, the simulations displayed next to no influence of the remaining three parameters (cooled plate temperature, gas inlet velocity and domain size) on these two output parameters. Figures D.3 and D.4 display the influence of fresh gas temperature, T_u, and equivalence ratio, Φ, on the laminar flame speed enhancement, $\Delta S_\mathrm{L}/S_\mathrm{L}$, and on the flame temperature enhancement, $\Delta T/T$. The enhancement of laminar flame speed is significant, reaching up to 80 % over the range of unburnt gas temperature considered (up to 393 K), while reaching 50 % when the equivalence ratio went from its initial value of 0.8 to 1.05. The relative increase in flame speed is lower; it reaches indeed only 5 % over the same range of unburnt gas temperature considered and 12 % for an equivalence ratio of 1.05.

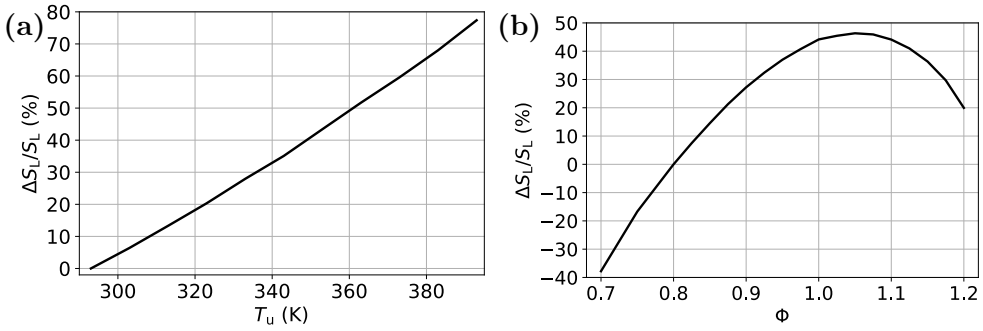

Figure D.3: *Influence of simulation input parameters on the laminar flame speed enhancement, $\Delta S_\mathrm{L}/S_\mathrm{L}$, determined from the gas velocity at the flame location, z_0.*

It has been mentioned above that the effect of the cooled plate temperature, domain size and fresh gas velocity on the flame speed and temperature enhancement are negligible compared to the established effects of equivalence ratio and fresh gas temperature. Indeed, the only way these parameters influ-

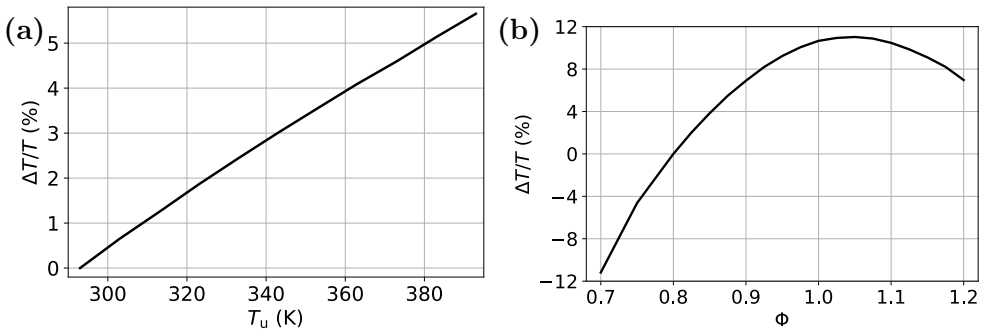

Figure D.4: *Influence of simulation input parameters on the flame temperature enhancement, $\Delta T/T$, determined as the maximum temperature reached by the gases on the computational domain.*

ence the flame is by modifying—slightly so—the distance between flame and cooled plate temperature, thus modifying the heat transfer of the flame with it. This minimal influence is considered as the numerical uncertainty on the flames computed in this work, it is estimated as 5 % for the laminar flame speed enhancement and 1 % for the flame temperature enhancement.

The position of the flame yielded by the numerical simulations needs to be corrected to take into account two effects. First is the numerical-experimental deskew: all throughout Sections 4.3.2 and 4.4, the experimentally observed flame front has been detected with the OH* emission while the computed flame has been considered to be located where the concentration of OH reached its maximum value. These two criteria for flame detection result in different positions of the flame; the position of the computed flame is thus corrected. Second is the fact that, due to the presence of the central electrode upstream of the nozzle, the velocity at the outlet of the nozzle is lower than the bulk velocity of the rest of the flow. Once the computed flame position is corrected, the velocity of the inlet gas is adjusted so as to match the position of the flame's centre in the experiments.

The numerical-experimental mismatch is displayed in Figure D.5, where the position of the side of the experimental flame, determined by the OH* emission, is plotted (blue line) and compared to the numerical OH concentration (black line).

The comparison of the two peaks of OH* emission and OH concentration (both peaks indicated with red lines), allows to display that the computed flame's position is located 0.84 mm upstream of the experimental flame's leading edge. This correction between experimental and numerical flame position is applied to each computed flame in order to allow comparison between simulations and

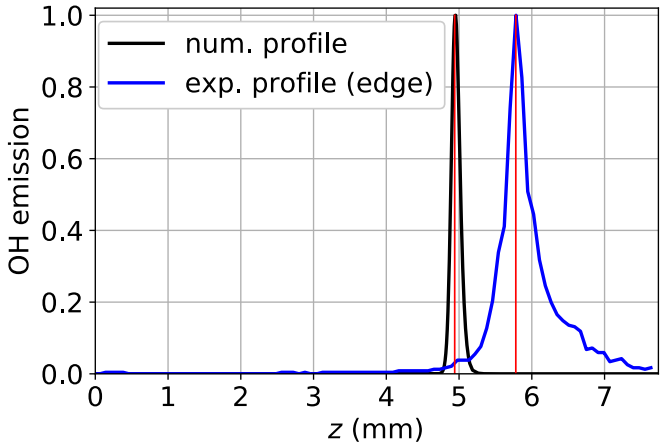

Figure D.5: *Comparison of the experimental profile of OH* emission (blue line) with the computed OH concentration profile (black line). The shift between numerical and experimental positions of the flame is yielded by comparing the position of the peaks (red lines).*

experimental results.

The second issue is due to the presence of the central electrode upstream of the flame. This electrode generates a velocity deficit in the centre of the nozzle jet resulting in a curved flame (see Figure 3.9). This velocity deficit is estimated by matching the position of the computed flame with the position in the centre of the leading edge of the flame. Figure D.6 presents this process: the OH* emission in the centre of the flame (solid blue line) increases sharply until reaching a first plateau 4.7 mm from the burner's nozzle, which corresponds to the position of the lower edge of the flame. After this plateau, the value of OH* emission increases again until reaching its maximum at 5.8 mm, the same position as the sides of the flame (green line). The experimental bulk velocity of the fresh gases is $1.2\,\mathrm{m.s^{-1}}$ and the experimental-numerical shift of 0.84 mm is applied to match the computed flame position (solid black line) to the experimental position of the sides as explained previously. Then, to take into account the velocity deficit in the centre of the flame, the numerical inlet velocity is decreased until the position of the computed flame (peak of OH concentration) matches the position of the centre of the flame (detected with OH* emission) in the experiments. This match is obtained for an inlet velocity of $0.8\,\mathrm{m.s^{-1}}$. This value is used as the computational inlet velocity of the fresh gases in all the numerical simulations presented in this work, meaning that, instead of the value of 4.5 times the flame velocity, the actual velocity of the unburnt gases in the centre of the nozzle is only three times the laminar flame speed.

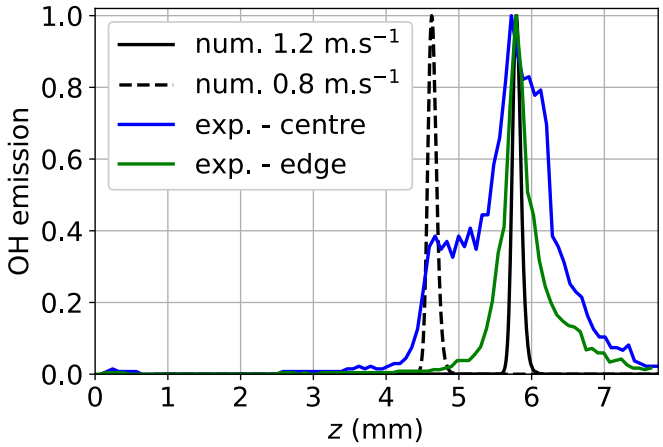

Figure D.6: *OH emission profile along the axial direction of the computed flame (black lines) with two velocities and of the centre (blue line) and the edge (green line) of the experimental flame. The computed flame's position (black lines) is matched with the experimental flame's central position by decreasing the inlet gas velocity from 1.2 to 0.8 m.s^{-1}.*

Appendix E

Modified GRI-Mech 3.0 for inclusion of ozone and nitric oxide effect

Simulations with the Cantera (see Goodwin et al. 2017) package have been realised, in order to estimate the effect of species generated by the NRP discharges in Section 4.4. The original GRI-Mech 3.0 mechanism from Smith et al. has been modified in order to include reactions involving ozone and nitric oxide. The transport properties for ozone and nitric oxide have been taken from Kee et al. (1986) and the coefficients for calculation of thermodynamic data from Mcbride et al. (1993).

Table E.1 contains the reactions added to the GRI-Mech 3.0 mechanism, as well as the Arrhenius coefficients used. The reactions have been taken from Ibraguimova et al. (2003), and from Atkinson et al. (2003) for the reaction of ozone with the molecules of air and from Starik et al. (2007) for the last three reactions of ozone with fuel fragments.

Table E.2 contains the equations which have been added to the GRI-Mech 3.0 mechanism. Lamoureux et al. (2015) mention the lack of a low-chemistry mechanism and develop such a mechanism in Lamoureux et al. (2016), as well as validate it for methane-air premixed flames. This mechanism includes prompt NO formation through a pathway involving the NCN species and is given in Table E.2. Although the reactions from Table E.2 have been added in the mechanism, the influence of nitric oxides on the properties of a one-dimensional axisymmetric computed flame have not been studied. The mechanism of reaction is given for the purpose of possible future works.

Reaction	A $[\mathrm{cm^3.mol^{-1}.s^{-1}}]$	b [.]	E_a/r [K]
$O_3 + O_2 \rightarrow O_2 + O + O_2$	1.54×10^{14}	0	11,600
$O_3 + O \rightarrow O_2 + O + O$	2.48×10^{15}	0	11,430
$O_3 + O_3 \rightarrow O_2 + O + O_3$	4.40×10^{14}	0	11,600
$O_3 + N_2 \rightarrow O_2 + O + N_2$	4.40×10^{14}	0	11,400
$O_2 + O + O_2 \rightarrow O_3 + O_2$	3.26×10^{19}	-2.06	0
$O_2 + O + N_2 \rightarrow O_3 + N_2$	1.60×10^{14}	-0.39	-700
$O_2 + O + O \rightarrow O_3 + O$	2.28×10^{15}	-0.50	-700
$O_2 + O + O_3 \rightarrow O_3 + O_3$	1.67×10^{15}	-0.51	-700
$O_2 + O_2 \rightarrow O + O + O_2$	9.80×10^{24}	-2.50	59,380
$O_2 + O \rightarrow O + O + O$	3.50×10^{25}	-2.50	59,380
$O_2 + O_3 \rightarrow O + O + O_3$	1.20×10^{19}	-1.00	59,380
$O_2 + H_2O \rightarrow O + O + H_2O$	1.20×10^{19}	-1.00	59,380
$O + O + O_2 \rightarrow O_2 + O_2$	1.50×10^{16}	-0.41	0
$O + O + N_2 \rightarrow O_2 + N_2$	6.00×10^{13}	0	-900
$O + O + O \rightarrow O_2 + O$	5.34×10^{16}	-0.41	0
$O + O + O_3 \rightarrow O_2 + O_3$	1.30×10^{14}	0	-900
$O_2 + O_2 \rightarrow O_3 + O$	1.20×10^{13}	0	50,500
$O_3 + O \rightarrow O_2 + O_2$	4.82×10^{12}	0	2,060
$O_3 + H \rightarrow O_2 + OH$	6.87×10^{13}	0	437
$O_2 + OH \rightarrow H + O_3$	4.40×10^{7}	1.44	38,600
$O_3 + OH \rightarrow HO_2 + O_2$	9.60×10^{11}	0	1,000
$O_3 + HO_2 \rightarrow OH + O_2 + O_2$	1.66×10^{11}	-0.3	1,000
$NO + O_3 \rightarrow NO_2 + O_2$	8.43×10^{11}	0	1,310
$CH_3 + NO_2 \rightarrow CH_3O + NO$	1.39×10^{13}	0	0
$CH_3O_2 + NO \rightarrow CH_3O + NO_2$	2.53×10^{12}	0	-358
$CH_3 + O_2 \rightarrow CH_3O_2$	1.01×10^{8}	1.6	0
$CH_3 + O_3 \rightarrow CH_3O + O_2$	3.13×10^{12}	0	220
$CH_4 + O_3 \rightarrow CH_3O + HO_2$	8.13×10^{10}	0	7,700
$CH_4 + O_3 \rightarrow CH_3O_2 + OH$	8.13×10^{10}	0	7,700

Table E.1: *Reactions included in the GRI-Mech 3.0 mechanism for inclusion of an ozone reaction mechanism.*

Once the reactions were added to the GRI-Mech 3.0, the updated mechanism has been validated with experimental and numerical data from the bibliography. First of all, it has been checked that the addition of these new reactions hasn't altered the capacity of the mechanism to predict the laminar flame speed of a methane-air premixed flame in atmospheric conditions. Figure E.1 compares the laminar flame speed of a freely-propagating flame with the initial mechanism (dashed blue line) to the ones obtained with the GRI-Mech 3.0 modified according to Tables E.1 and E.2 (dotted green line). A third set of data (solid black line), experimentally determined by Vagelopoulos and Egolpoulos (1998),

Reaction	A $[\mathrm{cm^3.mol^{-1}.s^{-1}}]$	b [.]	E_a/r [K]
$CH + N_2 \rightarrow NCN + H$	1.95×10^{12}	0	16,915
$NCN + H \rightarrow HCN + N$	3.84×10^{14}	0	7,956
$NCN + O_2 \rightarrow NO + NCO$	3.80×10^{12}	0.51	24,616
$NCN + OH \rightarrow HCN + NO$	4.71×10^{13}	0.44	4,006
$NCN + O \rightarrow CN + NO$	9.60×10^{13}	0	1,387
$NCN + H_2 \rightarrow HNCN + H$	4.11×10^{13}	0.51	24,163
$NCN + M \rightarrow C + N_2 + M$	8.90×10^{13}	0.51	62,127
$NCN + NCN \rightarrow CN + CN + N_2$	3.70×10^{12}	0	0
$NCN + C \rightarrow CN + CN$	1.00×10^{14}	0	0
$NCN + N \rightarrow CN + N_2$	1.00×10^{13}	0	0
$NCN + CN \rightarrow C_2N_2 + N$	1.25×10^{14}	0	8,000
$NCN + H \rightarrow HNCN$	1.79×10^{42}	-9.28	3,300
$HNCN + O \rightarrow NO + HNC$	1.22×10^{14}	-0.05	72
$HNCN + O \rightarrow NH + NCO$	5.60×10^{13}	-0.05	72
$HNCN + O \rightarrow CN + HNO$	9.36×10^{12}	-0.05	72
$HNCN + O_2 \rightarrow HO2 + NCN$	1.26×10^{8}	1.28	24,235
$HNCN + OH \rightarrow H_2O + NCN$	1.04×10^{5}	2.48	-1,890
$HNCN + O \rightarrow NH + NCO$	5.60×10^{13}	-0.05	72
$NO + O + M \rightarrow NO_2 + M$	1.35×10^{15}	-0.8	0
$N_2O + M \rightarrow N_2 + O + M$	1.30×10^{12}	-0.05	31,442
$HCN + M \rightarrow HNC + M$	3.50×10^{13}	0	23,750
$HCNO \rightarrow HCN + O$	4.20×10^{31}	-6.1	30,800
$CH_3 + NO_2 \rightarrow CH_3O + NO$	1.39×10^{13}	0	0
$CH_3O_2 + NO \rightarrow CH_3O + NO_2$	2.53×10^{12}	0	-358
$CH_3 + O_2 \rightarrow CH_3O_2$	1.01×10^{8}	1.6	0

Table E.2: *Reactions included in the GRI-Mech 3.0 mechanism for inclusion of a nitric oxide reaction mechanism.*

is added for comparison with the numerically determined data.

Results for the laminar flame speed with ozone addition are now compared to several experimental studies in order to validate the implemented reactions. Figure E.2 compares the evolution of the predicted laminar flame speed (dashed blue line) with the equivalence ratio for a methane-air flame at atmospheric pressure and temperature to laminar flame speeds determined experimentally in Gao et al. (2015) (solid black line) where this laminar flame speed has been determined for axisymmetric laminar methane-air Bunsen flames, for an ozone addition in the fresh gases of 6,334 ppm.

The laminar flame speed evolution follows the same trend in both studies.

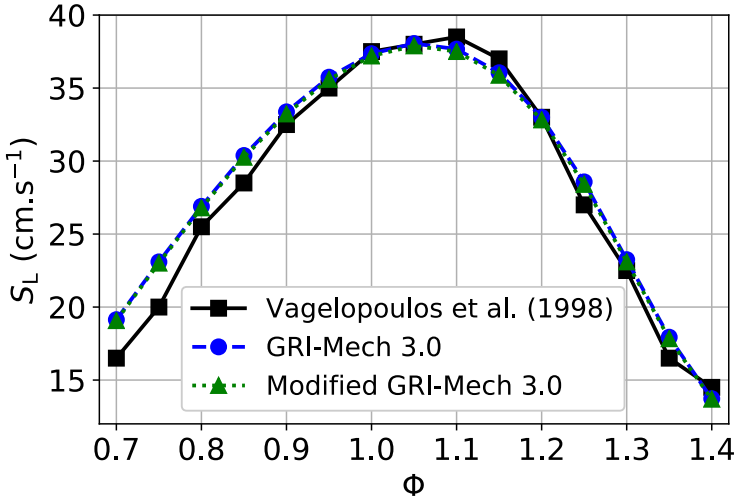

Figure E.1: *Comparison of the computed laminar flame speed of a methane-air premixed flame for the original GRI-Mech 3.0 mechanism (dashed blue line) and the updated mechanism (dotted green line) with the reactions from Tables E.1 and E.2. The third set of data (solid black line) corresponds to experimental measurements from Vagelopoulos and Egolpoulos (1998). The pressure is 1 atm and the unburnt gas is at a temperature of 300 K.*

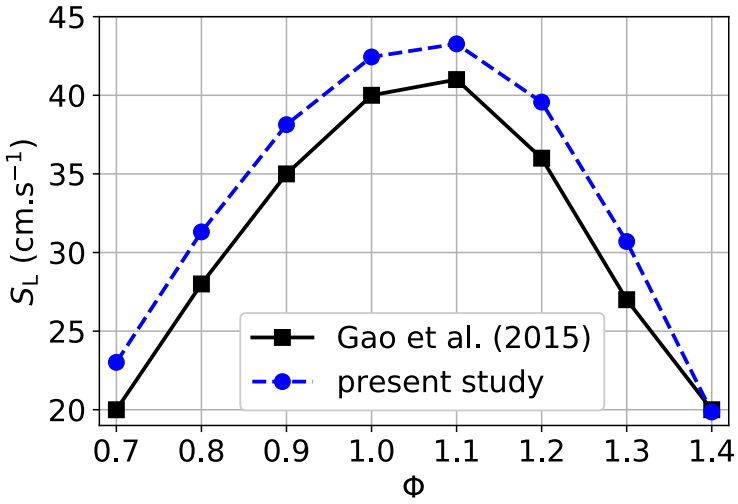

Figure E.2: *Comparison of the laminar flame speed as a function of equivalence ratio in the present study (dashed blue line) to the data from Gao et al. (2015). The premixed methane-air flame is at atmospheric pressure and temperature and the ozone addition is 6,334 ppm.*

The present model tends to overestimate a little the flame speed enhancement with ozone addition, with a maximum deviation of 10 % from the experimental

results from Gao et al. (2015).

The evolution of the laminar flame speed enhancement with ozone addition has been compared as a function of the ozone concentration in the unburnt gas. Figure E.3 compares the enhancement obtained with the model (dashed blue line) to the enhancement measured by Wang et al. (2012) (solid black line) and by Gao et al. (2015) (dotted green line). Both experiments have been realised at atmospheric pressure and temperature, for equivalence ratios of respectively 0.7 and 0.65 while the numerical results of the present study have been realised for $\Phi = 0.65$.

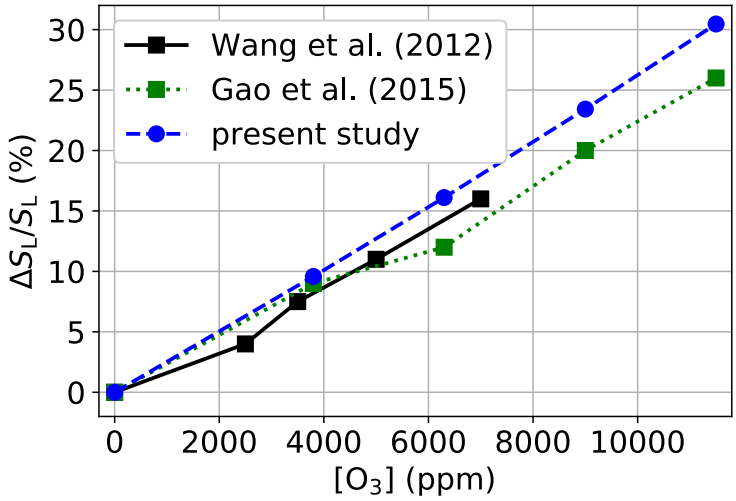

Figure E.3: *Laminar flame speed enhancement as a function of ozone addition (dashed blue line) where $\Phi = 0.65$, compared to data from Wang et al. (2012) (solid black line) where $\Phi = 0.7$ and Gao et al. (2015) (dotted green line) where $\Phi = 0.65$.*

The present model overestimates the evolution of flame speed with the ozone concentration compared to the experimental results from Wang et al. (2012) and Gao et al. (2015). At 11,000 ppm of ozone, the laminar flame speed enhancement measured by Gao et al. (2015) is 26 % while the one of the present study is 31 %. Since the maximum ozone concentration considered in Chapter 3 is 15,000 ppm, the overall uncertainty on the laminar flame speed enhancement by ozone addition is considered to be 5 %.

References

Adamovich, I. V., I. Choi, N. Jiang, J.-H. Kim, S. Keshav, W. R. Lempert, E. Mintusov, M. Nishihara, M. Samimy, and M. Uddi (2009). Plasma assisted ignition and high-speed flow control: non-thermal and thermal effects. *Plasma Sources Science and Technology 18*, 034018. *(p. xxvii, 14, 24)*

Alquaity, A. B. S., J. Han, M. Chahine, H. Selim, M. Belhi, S. M. Sarathy, F. Bisetti, and A. Farooq (2017). Measurements of positively charged ions in premixed methane-oxygen atmospheric flames. *Combustion Science and Technology 189*(4), 575–594. *(p. 54)*

Alves, L. L. (2014). The IST-Lisbon database on LXCat. *Journal of Physics: Conference Series 565*(1). *(p. 102, 132)*

Atkinson, R., D. L. Baulch, R. a. Cox, J. N. Crowley, R. F. Hampson, R. G. Hynes, M. E. Jenkin, M. J. Rossi, and J. Troe (2003). Evaluated kinetic and photochemical data for atmospheric chemistry: Part 1 - gas phase reactions of Ox, HOx, NOx and SOx species. *Atmospheric Chemistry and Physics Discussions 3*(6), 6179–6699. *(p. 103, 145)*

Bak, M. S. and M. A. Cappelli (2015). Numerical studies of nitric oxide formation in discharge-stabilized flames of premixed methane / air. *(p. xvi, 10, 12)*

Bálek, R., M. Červenka, and S. Pekárek (2014). Acoustic field effects on a negative corona discharge. *Plasma Sources Science and Technology 23*(3), 035005. *(p. 24)*

Barbosa, S., G. Pilla, D. A. Lacoste, P. Scouflaire, S. Ducruix, C. O. Laux, and D. Veynante (2015). Influence of nanosecond repetitively pulsed discharges on the stability of a swirled propane/air burner representative of an aeronautical combustor. *Philosophical Transactions of the Royal Society A: Mathematical, Physical and Engineering Sciences 373*(2048), 20140335. *(p. xvi, 15, 16, 78)*

Bergthorson, J. M., D. G. Goodwin, and P. E. Dimotakis (2005). Particle streak velocimetry and CH laser-induced fluorescence diagnostics in strained, premixed, methane-air flames. *Proceedings of the Combustion Institute 30*(1), 1637–1644. *(p. 90)*

Biagi, S. F. (2010). Fortran program, MAGBOLTZ, S.F. Biagi, versions 8.9

and after. *(p. 132)*

Bogaerts, A., A. Okhrimovskyy, and R. Gijbels (2002). Calculation of the gas flow and its effect on the plasma characteristics for a modified Grimm-type glow discharge cell. *Journal of Analytical Atomic Spectrometry 17*, 1076–1082. *(p. 24)*

Bouvet, N., D. Davidenko, C. Chauveau, L. Pillier, and Y. Yoon (2014). On the simulation of laminar strained flames in stagnation flows: 1D and 2D approaches versus experiments. *Combustion and Flame 161*(2), 438–452. *(p. 90)*

Bowman, S. S., I. V. Adamovich, and W. R. Lempert (2014). Experimental and modeling analysis of singlet delta oxygen kinetics in a repetitively pulsed nanosecond discharge. *Plasma Sources Science and Technology 23*(3), 035009. *(p. 8)*

Cahill, O. J., T. Claro, N. O'Connor, A. A. Cafolla, N. T. Stevens, S. Daniels, and H. Humphreys (2014). Cold air plasma to decontaminate inanimate surfaces of the hospital environment. *Applied and Environmental Microbiology 80*(6), 2004–2010. *(p. 3)*

Canny, J. (1986). A Computational Approach to Edge Detection. *IEEE Transactions on Pattern Analysis and Machine Intelligence PAMI-8*(6), 679–698. *(p. 71, 80)*

Chabert, P., A. Rousseau, G. Gousset, and P. Leprince (1998). On the influence of the gas velocity on dissociation degree and gas temperature in a flowing microwave hydrogen discharge. *J. App. Phys. 84*(1), 161–167. *(p. 24)*

Chen, J. and J. H. Davidson (2002). Ozone Production in the Positive DC Corona Discharge: Model and Comparison to Experiments. *Plasma Chemistry and Plasma Processing 22*(4), 495–522. *(p. 8, 100, 101)*

Clanet, C. and G. Searby (1998). First Experimental Study of the Darrieus-Landau Instability. *Physical Review Letters 80*(17), 3867–3870. *(p. 59)*

Colas, D. F., A. Ferret, D. Z. Pai, D. A. Lacoste, and C. O. Laux (2010). Ionic wind generation by a wire-cylinder-plate corona discharge in air at atmospheric pressure. *Journal of Applied Physics 108*(10). *(p. 24)*

Cosby, P. C. (1993). Election-impact dissociation of oxygen. *The Journal of Chemical Physics 98*(12), 9560–9569. *(p. 7)*

Debien, A., N. Benard, and E. Moreau (2012). Streamer inhibition for improving force and electric wind produced by DBD actuators. *Journal of Physics D: Applied Physics 45*(May), 215201. *(p. 24)*

Evans, N. A. (1967). Effect of flow velocity on a single, controlled glow discharge in cesium-seeded argon. *AIAA Journal 5*(10), 1908–1910. *(p. 24)*

Fialkov, A. B. (1997). Investigations on ions in flames. *Progress in Energy and Combustion Science 23*, 399–528. *(p. 54, 61)*

Fridman, A. (2008). *Plasma Chemistry*. *(p. 1)*

Gao, X., Y. Zhang, S. Adusumilli, J. Seitzman, W. Sun, T. Ombrello, and C. Carter (2015). The effect of ozone addition on laminar flame speed.

Combustion and Flame 162(10), 3914–3924. *(p. xxiv, 104, 147, 148, 149)*

Gillan, C. J., J. Tennyson, B. M. McLaughlin, and P. G. Burke (1996). Low-energy electron impact excitation of the nitrogen molecule: optically forbidden transitions. *Journal of Physics B: Atomic, Molecular and Optical Physics 29*(8), 1531–1547. *(p. 10)*

Goodings, J. M., D. K. Bohme, and C.-W. Ng (1979a). Detailed ion chemistry in methane oxygen flames. I. Positive ions. *Combustion and Flame 36*, 27–43. *(p. 54)*

Goodings, J. M., D. K. Bohme, and C.-W. Ng (1979b). Detailed ion chemistry in methane oxygen flames. II. Negative ions. *Combustion and Flame 36*, 45–62. *(p. 54)*

Goodings, J. M., D. K. Bohme, and F. T. M. Sudken (1977). Positive ion probe of methane-oxygen combustion. *Kinetics of Elementary Reactions 16*(1), 891–902. *(p. 61)*

Goodwin, D. G., H. K. Moffat, and R. L. Speth (2017). Cantera: An Object-oriented Software Toolkit for Chemical Kinetics, Thermodynamics, and Transport Processes. *(p. 103, 135, 145)*

Hagelaar, G. J. M. and L. C. Pitchford (2005). Solving the Boltzmann equation to obtain electron transport coefficients and rate coefficients for fluid models. *Plasma Sources Sci. Technol. 14*(14), 722–733. *(p. 102, 131)*

Haley, R. F., P. R. Smy, H. Search, C. Journals, A. Contact, M. Iopscience, and I. P. Address (1989). Electrically induced turbulence-the short duration spark. *Journal of Physics D: Applied Physics 22*(2), 258. *(p. 24)*

Heinlin, J., G. Morfill, M. Landthaler, W. Stolz, G. Isbary, J. L. Zimmermann, T. Shimizu, and S. Karrer (2010). Plasma-Medizin: Anwendungsmöglichkeiten in der Dermatologie. *JDDG - Journal of the German Society of Dermatology 8*(12), 968–977. *(p. xxvii, 2)*

Heitz, S., D. A. Lacoste, and J. P. Moeck (2017a). Effect of nanosecond plasma discharges on methane-air premixed stagnation flames. *Proceedings of the European Combustion Meeting 2017*, 1378–1383. *(p. 77)*

Heitz, S., J. P. Moeck, A. Bourdon, and D. A. Lacoste (2017b). Numerical investigation of thermal and chemical effects of nanosecond repetitively pulsed discharges on a laminar premixed counterflow flame. *Proceedings of the Asian-Pacific Combustion Meeting 2017*, 4. *(p. 77)*

Heitz, S., J. P. Moeck, T. Schuller, D. Veynante, and D. A. Lacoste (2016). Influence of air flow parameters on nanosecond repetitively pulsed discharges in a pin-annular electrode configuration. *Journal of Physics D: Applied Physics 49*(15), 155205. *(p. 23)*

Hicks, A., S. Norberg, P. Shawcross, W. R. Lempert, J. W. Rich, and I. V. Adamovich (2005). Singlet oxygen generation in a high pressure non-self-sustained electric discharge. *Journal of Physics D: Applied Physics 38*(20), 3812–3824. *(p. 8)*

Hirst, A. M., F. M. Frame, N. J. Maitland, and D. O'Connell (2014). Low temperature plasma: A novel focal therapy for localized prostate cancer?

BioMed Research International 2014. *(p. 3, 24)*

Ibraguimova, L. B., G. D. Smekhov, and O. P. Shatalov (2003). Recommended Rate Constants of Chemical Reactions in an H 2 -O 2 Gas Mixture With Electronically Excited Reactions in an H 2 -O 2 Gas Mixture With. *2*, 1–31. *(p. 102, 103, 131, 145)*

Ionin, A. A., I. V. Kochetov, A. P. Napartovich, and N. N. Yuryshev (2007). Physics and engineering of singlet delta oxygen production in low-temperature plasma. *Journal of Physics D: Applied Physics 40*(2), R25–R61. *(p. 8)*

Itikawa, Y. (2017). Itikawa database. *(p. 132)*

Jaworek, A. and A. Krupa (1996). Corona discharge from a multipoint electrode in flowing air. *Journal of Electrostatics 38*(3), 187–197. *(p. 24, 34)*

Jiang, N., N. Lu, K. Shang, J. Li, and Y. Wu (2013). Effects of electrode geometry on the performance of dielectric barrier/packed-bed discharge plasmas in benzene degradation. *Journal of Hazardous Materials 262*, 387–393. *(p. 3)*

Johnson, R. F., A. C. Vandine, G. L. Esposito, and H. K. Chelliah (2015). On the axisymmetric counterflow flame simulations: Is there an optimal nozzle diameter and separation distance to apply quasi one-dimensional theory? *Combustion Science and Technology 187*(1-2), 37–59. *(p. 62)*

Ju, Y. and W. Sun (2015a). Plasma assisted combustion: Dynamics and chemistry. *Progress in Energy and Combustion Science 48*(C), 21–83. *(p. xv, xxvii, 2, 14)*

Ju, Y. and W. Sun (2015b). Plasma assisted combustion: Progress, challenges, and opportunities. *Combustion and Flame 162*(3), 529–532. *(p. xxvii)*

Kee, R. J., G. Dixon-lewis, and J. A. Miller (1986). 1ss Gas-Phase Multicomponent Transport Properties. (December). *(p. 145)*

Kim, W., H. Do, M. Mungal, and M. Cappelli (2006). Flame stabilization enhancement and NOx production using ultra short repetitively pulsed plasma discharges. *44th Aerospace Sciences ...* (January), 1–13. *(p. xv, 10, 11, 16)*

Kim, W., H. Do, M. G. Mungal, and M. A. Cappelli (2007). Investigation of NO production and flame structure in plasma enhanced premixed combustion. *Proceedings of the Combustion Institute 31 II*, 3319–3326. *(p. 16, 78)*

Kogelschatz, U., B. Eliasson, and M. Hirth (1988). Ozone Generation from Oxygen and Air: Discharge Physics and Reaction Mechanisms. *Ozone Science and Engineering 10*, 367–378. *(p. 8)*

Kong, M. G., G. Kroesen, G. Morfill, T. Nosenko, T. Shimizu, J. Van Dijk, and J. L. Zimmermann (2009). Plasma medicine: An introductory review. *New Journal of Physics 11*. *(p. 3, 24)*

Kopiev, V. F., Y. S. Akishev, I. V. Belyaev, N. K. Berezhetskaya, V. a.

Bityurin, G. a. Faranosov, M. E. Grushin, a. I. Klimov, V. a. Kopiev, I. a. Kossyi, I. a. Moralev, N. N. Ostrikov, M. I. Taktakishvili, N. I. Trushkin, and M. Y. Zaytsev (2014). Instability wave control in turbulent jet by plasma actuators. *Journal of Physics D: Applied Physics 47*(50), 505201. *(p. 24)*

Kozlov, V. E., A. M. Starik, and N. S. Titova (2008). Enhancement of Combustion of a Hydrogen-Air Mixture by Excitation of O2 Molecules to the a1Δg State. *Combustion, Explosion, and Shock Waves 44*(4), 371–379. *(p. 8)*

Kumar, S. and P. K. Ghosh (1993). Dissociation of nitrogen in flowing DC glow plasmas. *Journal of Physics D: Applied Physics 26*(9), 1419–1426. *(p. 10)*

Lacoste, D. A., B. J. Lee, A. Satija, S. Krishna, S. A. Steinmetz, I. Alkhesho, O. Hazzaa, R. P. Lucht, M. S. Cha, and W. L. Roberts (2017c). Investigation of Gas Heating by Nanosecond Repetitively Pulsed Glow Discharges Used for Actuation of a Laminar Methane-Air Flame. *Combustion Science and Technology 2202*(July), 1–11. *(p. xv, xxvii, 6, 7, 20, 78, 90)*

Lacoste, D. A., J. P. Moeck, D. Durox, C. O. Laux, and T. Schuller (2013b). Effect of Nanosecond Repetitively Pulsed Discharges on the Dynamics of a Swirl-Stabilized Lean Premixed Flame. *Journal of Engineering for Gas Turbines and Power 135*(10), 101501. *(p. xvi, 19, 20)*

Lacoste, D. A., J. P. Moeck, C. O. Paschereit, and C. O. Laux (2013a). Effect of Plasma Discharges on Nitric Oxide Emissions in a Premixed Flame. *Journal of Propulsion and Power 29*(3), 748–751. *(p. xvi, 16, 17, 18, 78, 101)*

Lacoste, D. A., J. P. Moeck, W. L. Roberts, S. H. Chung, and M. S. Cha (2017a). Analysis of the step responses of laminar premixed flames to forcing by non-thermal plasma. *Proceedings of the Combustion Institute 36*(3), 4145–4153. *(p. xxvii, 6, 78)*

Lacoste, D. A., Y. Xiong, J. P. Moeck, S. H. Chung, W. L. Roberts, and M. S. Cha (2017b). Transfer functions of laminar premixed flames subjected to forcing by acoustic waves, AC electric fields, and non-thermal plasma discharges. *Proceedings of the Combustion Institute 36*(3), 4183–4192. *(p. xvi, xxvii, 19, 21)*

Lagmich, Y., T. Callegari, L. C. Pitchford, and J. P. Boeuf (2008). Model description of surface dielectric barrier discharges for flow control. *Journal of Physics D: Applied Physics 41*(9), 095205. *(p. 24)*

Lamoureux, N., H. El Merhubi, L. Gasnot, C. Schoemaecker, and P. Desgroux (2015). Measurements and modelling of HCN and CN species profiles in laminar CH4/O2/N2 low pressure flames using LIF/CRDS techniques. *Proceedings of the Combustion Institute 35*(1), 745–752. *(p. 145)*

Lamoureux, N., H. E. Merhubi, L. Pillier, S. de Persis, and P. Desgroux (2016). Modeling of NO formation in low pressure premixed flames. *Combustion and Flame 163*, 557–575. *(p. 145)*

Laporta, V., R. Celiberto, and J. Tennyson (2014). Dissociative electron attachment and electron-impact resonant dissociation of vibrationally excited O2 molecules. *Physical Review A - Atomic, Molecular, and Optical Physics 91*(1). *(p. 7)*

Laporta, V., R. Celiberto, and J. Tennyson (2015). Dissociative electron attachment and electron-impact resonant dissociation of vibrationally excited O2 molecules. *Physical Review A - Atomic, Molecular, and Optical Physics 91*(1), 1–5. *(p. 7)*

Law, C. K. (2006). *Combustion physics* (Cambridge ed.). *(p. 7)*

Lebouvier, A., S. A. Iwarere, P. D'Argenlieu, D. Ramjugernath, and L. Fulcheri (2013). Assessment of carbon dioxide dissociation as a new route for syngas production: A comparative review and potential of plasma-based technologies. *Energy and Fuels 27*(5), 2712–2722. *(p. xxvii)*

Li, S. Z., W. T. Huang, and D. Wang (2009). The effect of gas flow on argon plasma discharge generated with a single-electrode configuration at atmospheric pressure. *Physics of Plasmas 16*(9). *(p. 24)*

Likhanskii, A. V., M. N. Shneider, S. O. MacHeret, and R. B. Miles (2008). Modeling of dielectric barrier discharge plasma actuator in air. *Journal of Applied Physics 103*(5). *(p. 24)*

Lu, X., G. V. Naidis, M. Laroussi, S. Reuter, D. B. Graves, and K. Ostrikov (2016). Reactive species in non-equilibrium atmospheric-pressure plasmas: Generation, transport, and biological effects. *Physics Reports 630*(April), 1–84. *(p. xxvii)*

Massines, F., C. Sarra-Bournet, F. Fanelli, N. Naudé, and N. Gherardi (2012). Atmospheric pressure low temperature direct plasma technology: Status and challenges for thin film deposition. *Plasma Processes and Polymers 9*(11-12), 1041–1073. *(p. 3, 24)*

Mcbride, B., S. Gordon, and M. Reno (1993). Coefficients for Calculating Thermodynamic and Transport Properties of Individual Species. *Nasa Technical Memorandum 4513*(NASA-TM-4513), 98. *(p. 145)*

Mcmanus, K. R., T. Poinsoti, and S. M. Candeli (1993). A review of active control of combustion instabilities. *Progress in Energy and Combustion Science 19*(1), 1–29. *(p. 19)*

Mericam-Bourdet, N., M. J. Kirkpatrick, F. Tuvache, D. Frochot, and E. Odic (2012). Effect of voltage waveform on dielectric barrier discharge ozone production efficiency. *The European Physical Journal Applied Physics 57*, 30801. *(p. 8, 24)*

Moeck, J. P., D. A. Lacoste, C. O. Laux, and C. O. Paschereit (2013). Control of combustion dynamics in a swirl-stabilized combustor with nanosecond repetitively pulsed discharges. *51st AIAA Aerospace Sciences Meeting including the New Horizons Forum and Aerospace Exposition* (January), AIAA–2013–565. *(p. 19, 78)*

Moreau, M., N. Orange, and M. G. J. Feuilloley (2008). Non-thermal plasma technologies: New tools for bio-decontamination. *Biotechnology*

Advances 26(6), 610–617. *(p. xxvii, 3)*

Morgan, W. L. (2017). Morgan database. *(p. 132)*

Nagaraja, S., T. Li, J. A. Sutton, I. V. Adamovich, and V. Yang (2015). Nanosecond plasma enhanced H2/O2/N2 premixed flat flames. *Proceedings of the Combustion Institute 35*(3), 3471–3478. *(p. 101)*

Napartovich, A. P., N. A. Dyatko, I. V. Kochetov, and A. G. Sukharev (2017). Triniti database. *(p. 132)*

Nighan, W. L. (1970). Electron Rates Excited. *2*(5). *(p. 54)*

Nijdam, S., E. Takahashi, J. Teunissen, and U. Ebert (2014). Streamer discharges can move perpendicularly to the electric field. *New Journal of Physics 16*(103038), 1–9. *(p. 74)*

Nozaki, T., A. Hattori, and K. Okazaki (2004). Partial oxidation of methane using a microscale non-equilibrium plasma reactor. *Catalysis Today 98*(4), 607–616. *(p. 3, 24)*

Ombrello, T., S. H. Won, Y. Ju, and S. Williams (2010a). Flame propagation enhancement by plasma excitation of oxygen. Part I: Effects of O3. *Combustion and Flame 157*(10), 1906–1915. *(p. 8)*

Ombrello, T., S. H. Won, Y. Ju, and S. Williams (2010b). Flame propagation enhancement by plasma excitation of oxygen. Part I: Effects of O3. *Combustion and Flame 157*(10), 1906–1915. *(p. 8, 100, 101, 131)*

Pai, D. Z. (2008). *Nanosecond Repetitively Pulsed Plasmas in Preheated Air at Atmospheric Pressure*. Ph. D. thesis, École Centrale Paris. *(p. xv, 3, 4, 5, 122)*

Pai, D. Z., D. A. Lacoste, and C. O. Laux (2010a). Nanosecond repetitively pulsed discharges in air at atmospheric pressure - the spark regime. *Plasma Sources Science and Technology 19*(065015), 10. *(p. xxvii, 3, 4, 33)*

Pai, D. Z., D. A. Lacoste, and C. O. Laux (2010b). Transitions between corona, glow, and spark regimes of nanosecond repetitively pulsed discharges in air at atmospheric pressure. *Journal of Applied Physics 107*(9). *(p. xxvii, 3, 25, 33, 54, 60, 84)*

Pai, D. Z., G. D. Stancu, D. A. Lacoste, and C. O. Laux (2009). Nanosecond repetitively pulsed discharges in air at atmospheric pressure - the glow regime. *Plasma Sources Science and Technology 18*(045030), 7. *(p. xxvii, 3, 4, 34, 56, 67, 102)*

Pancheshnyi, S. V., D. A. Lacoste, A. Bourdon, and C. O. Laux (2006). Ignition of propane-air mixtures by a repetitively pulsed nanosecond discharge. *IEEE Transactions on Plasma Science 34*(6), 2478–2487. *(p. xvi, 12, 13)*

Parker, J. R. (2011). *Algorithms for image prcessing and computer vision*. *(p. 71)*

Pereira, R., D. Ragni, and M. Kotsonis (2014). Effect of external flow velocity on momentum transfer of dielectric barrier discharge plasma actuators. *Journal of Applied Physics 116*(10). *(p. 24)*

Phelps, A. W. (2017). Phelps databse. *(p. 132)*

Pitchford, L. C., L. L. Alves, K. Bartschat, S. F. Biagi, M. C. Bordage, I. Bray, C. E. Brion, M. J. Brunger, L. Campbell, A. Chachereau, B. Chaudhury, L. G. Christophorou, E. Carbone, N. A. Dyatko, C. M. Franck, D. V. Fursa, R. K. Gangwar, V. Guerra, P. Haefliger, G. J. Hagelaar, A. Hoesl, Y. Itikawa, I. V. Kochetov, R. P. McEachran, W. L. Morgan, A. P. Napartovich, V. Puech, M. Rabie, L. Sharma, R. Srivastava, A. D. Stauffer, J. Tennyson, J. de Urquijo, J. van Dijk, L. A. Viehland, M. C. Zammit, O. Zatsarinny, and S. Pancheshnyi (2017). LXCat: an Open-Access, Web-Based Platform for Data Needed for Modeling Low Temperature Plasmas. *Plasma Processes and Polymers 14*(1-2), 1–17. *(p. 132)*

Popov, N. A. (2001). Investigation of the mechanism for rapid heating of nitrogen and air in gas discharges. *Plasma Physics Reports 27*(10), 886–896. *(p. 131)*

Popov, N. A. (2011). Effect of singlet oxygen O2(a1âˆ†g) molecules produced in a gas discharge plasma on the ignition of hydrogen-oxygen mixtures. *Plasma Sources Science and Technology 20*(045002), 11. *(p. 8)*

Raizer, Y. P. (1987). *Gas Discharge Physics*. *(p. 1)*

Rickard, M., D. Dunn-Rankin, F. Weinberg, and F. Carleton (2005). Characterization of ionic wind velocity. *Journal of Electrostatics 63*(6-10), 711–716. *(p. 24)*

Rupf, S., A. Lehmann, M. Hannig, B. Schäfer, A. Schubert, U. Feldmann, and A. Schindler (2010). Killing of adherent oral microbes by a non-thermal atmospheric plasma jet. *Journal of Medical Microbiology 59*(2), 206–212. *(p. 3)*

Rusterholtz, D. L., D. A. Lacoste, G. D. Stancu, D. Z. Pai, and C. O. Laux (2013). Ultrafast heating and oxygen dissociation in atmospheric pressure air by nanosecond repetitively pulsed discharges. *Journal of Physics D: Applied Physics 46*(46), 464010. *(p. 6, 42, 101, 102, 131)*

Scapinello, M., L. Martini, G. Dilecce, and P. Tosi (2015). Reforming of CH4 and CO2 by a nanosecond-pulsed discharge at atmospheric pressure. *Ispc*, 5–7. *(p. 3)*

Singleton, D., C. Carter, S. J. Pendleton, C. Brophy, J. Sinibaldi, J. W. Luginsland, M. Brown, E. Stockman, and M. A. Gundersen (2016). The effect of humidity on hydroxyl and ozone production by nanosecond discharges. *Combustion and Flame 167*, 164–171. *(p. xv, 8, 9)*

Smith, G. P., D. M. Golden, M. Frenklach, N. W. Moriarty, B. Eiteneer, M. Goldenberg, C. T. Bowman, R. K. Hanson, S. Song, J. William C. Gardiner, V. V. Lissianski, and Z. Qin. GRI-Mech 3.0. *(p. 103, 135, 145)*

Snoeckx, R. and A. Bogaerts (2016). Plasma technology - a novel solution for CO2 conversion? *Chem. Soc. Rev.*. *(p. xxvii)*

Stancu, G. D., F. Kaddouri, D. A. Lacoste, and C. O. Laux (2010). Atmospheric pressure plasma diagnostics by OES, CRDS and TALIF. *Journal*

of Physics D: Applied Physics 43(12), 124002. *(p. 101)*

Starik, a. M., B. I. Lukhovitskii, and N. S. Titova (2007). Mechanism of the initiation of combustion in CH4(C2H2)/Air/O3 mixtures by laser excitation of the O3 molecules. *Kinetics and Catalysis 48*(3), 348–366. *(p. 103, 145)*

Starikovskaia, S. M. (2014). Plasma-assisted ignition and combustion: nanosecond discharges and development of kinetic mechanisms. *Journal of Physics D: Applied Physics 47*(35), 353001. *(p. xxvii, 54, 74)*

Starikovskiy, A. and N. Aleksandrov (2013). Plasma-assisted ignition and combustion. *Progress in Energy and Combustion Science 39*(1), 61–110. *(p. xxvii, 14, 24)*

Stauss, S., Y. Imanishi, H. Miyazoe, and K. Terashima (2010). High rate deposition of ZnO thin films by a small-scale inductively coupled argon plasma generated in open air. *Journal of Physics D: Applied Physics 43*(15), 155203. *(p. 3, 24)*

Stuckert, E. P. and E. R. Fisher (2015). Ar/O2 and H2O plasma surface modification of SnO2 nanomaterials to increase surface oxidation. *Sensors and Actuators, B: Chemical 208*, 379–388. *(p. 3)*

Sun, W., S. H. Won, T. Ombrello, C. Carter, and Y. Ju (2013). Direct ignition and S-curve transition by in situ nano-second pulsed discharge in methane/oxygen/helium counterflow flame. *Proceedings of the Combustion Institute 34*(1), 847–855. *(p. xvi, 13, 14)*

Tholin, F. and A. Bourdon (2011). Simulation of the stable quasi-periodic glow regime of a nanosecond repetitively pulsed discharge in air at atmospheric pressure. *Journal of Physics D: Applied Physics 44*(385303), 17. *(p. 75, 102)*

Vagelopoulos, C. M. and F. N. Egolpoulos (1998). Direct experimental determination of laminar flame speeds. *Proc. combust. Inst. 27*, 513–519. *(p. xxiv, 146, 148)*

Vojnovic, M., M. Popovic, M. M. Ristic, M. D. Vicic, and G. B. Poparic (2015). Rate coefficients for electron impact excitation of N2. *Chemical Physics 463*, 38–46. *(p. 10)*

Wang, Z. H., L. Yang, B. Li, Z. S. Li, Z. W. Sun, M. Aldén, K. F. Cen, and A. A. Konnov (2012). Investigation of combustion enhancement by ozone additive in CH4/air flames using direct laminar burning velocity measurements and kinetic simulations. *Combustion and Flame 159*(1), 120–129. *(p. xxiv, 104, 149)*

Wangher, A., G. Searby, and J. Quinard (2008). Experimental investigation of the unsteady response of premixed flame fronts to acoustic pressure waves. *Combustion and Flame 154*(1-2), 310–318. *(p. 59)*

Wortberg, G. (1965). Ion-concentration measurements in a flat flame at atmospheric pressure. *Symposium (International) on Combustion 10*(1), 651–655. *(p. 54, 61)*

Xu, D., M. N. Shneider, D. A. Lacoste, and C. O. Laux (2014). Thermal and

hydrodynamic effects of nanosecond discharges in atmospheric pressure air. *Journal of Physics D: Applied Physics 47*, 235202. *(p. 6, 10)*

Xu, D. A., D. A. Lacoste, D. L. Rusterholtz, P. Q. Elias, G. D. Stancu, and C. O. Laux (2011). Experimental study of the hydrodynamic expansion following a nanosecond repetitively pulsed discharge in air. *Applied Physics Letters 99*(12), 97–100. *(p. 6, 24)*

Zhang, X. and M. S. Cha (2015). Partial oxidation of methane in a temperature-controlled dielectric barrier discharge reactor. *Proceedings of the Combustion Institute 35*(3), 3447–3454. *(p. 3, 24)*

université PARIS-SACLAY
ÉCOLE DOCTORALE
Sciences mécaniques et énergétiques, matériaux et géosciences (SMEMAG)

Titre : mécanismes d'interaction entre décharges nanosecondes répétitives pulsées et écoulements laminaires réactifs

Mots clés : combustion, décharges plasma, écoulements laminaires

Résumé : Les interactions entre décharges Nanosecondes Répétitives Pulsées et des écoulements de gaz laminaires sont étudiées.
L'influence d'écoulements d'air stationnaires et instationnaires sur les régimes de décharges NRP est étudiée et les résultats interprétés au moyen de nombres adimensionnels afin de mettre en évidence l'effet synergétique du nombre d'impulsions appliquées, ainsi que de la puissance des pulses, sur le régime de décharge NRP observé. Une étude de l'effet de flammes méthane-air laminaires prémélangées sur des décharges NRP est ensuite présentée. Dans les deux configurations expérimentales utilisées, un effet de la flamme sur les décharges NRP en régime couronne est démontré. De plus, l'influence du mélange de gaz entre les électrodes sur la forme des décharges plasma est démontrée. Enfin, l'effet de décharges NRP en régime couronne sur des flammes plates laminaires prémélangées est étudié. Les décharges NRP entraînent un déplacement de la flamme vers l'amont. Des simulations numériques de flammes axisymétriques sont ensuite réalisées.
Cette étude met en évidence l'effet des décharges NRP sur une flamme et donne des indications sur le phénomène à l'origine de cet effet, à savoir l'augmentation de la vitesse de flamme laminaire par le biais de la génération de chaleur et d'ozone par les décharges plasma. De plus, l'étude démontre l'effet opposé de mélanges réactifs sur les décharges NRP. Les décharges NRP sont modifiées par le phénomène de convection du gaz entre les électrodes ainsi que par la constitution de ce gaz.

Title: Interaction mechanisms between nanosecond repetitively pulsed plasma discharges and laminar reactive flows

Keywords: combustion, plasma discharges, laminar flows

Abstract: The interactions between Nanosecond Repetitively Pulsed plasma discharges and laminar reactive flows are investigated.
The influence of steady and unsteady air flows on the regimes of NRP discharges is investigated. The results are interpreted with the use of characteristic dimensionless numbers; this analysis allows to highlight a synergetic effect between the high-voltage pulses as well as the power of the pulses on the NRP discharge regime observed. Then, an investigation of the effect of laminar premixed methane-air flames on NRP discharges is presented. An effect of the flame on the NRP corona discharges is displayed; this effect is a function of the proximity of the flame to the discharges. the influence of the inter-electrode gas mixture on the shape of the plasma discharges is also visually assessed. Finally, the effect of NRP corona discharges on laminar premixed flat flames is investigated. The NRP discharges induce a displacement of the flame in the upstream direction which is verified with numerical simulations.
This study displays the effect of NRP discharges on a flame and gives insights as to the phenomenon underlying this effect. Moreover, the study highlights the opposite effect of reactive mixtures on the NRP discharges. The visual modification of the NRP discharges is a function of the transport of the inter-electrode flow and of the nature of the gas itself.

Université Paris-Saclay
Espace Technologique / Immeuble Discovery
Route de l'Orme aux Merisiers RD 128 / 91190 Saint-Aubin, France